Multiscale Modeling of Calcium-Induced Arrhythmias

by
Mark A. Walker

A dissertation submitted to the Johns Hopkins University in conformity with the requirements for the degree of Doctor of Philosophy

Baltimore, Maryland
April 2016

© Copyright by Mark A. Walker 2016
All Rights Reserved

Abstract

Sudden cardiac death occurs when an unexpected ventricular arrhythmia degenerates into fibrillation, which prevents the heart from pumping blood through the body. Heart diseases such as heart failure are significant risk factors for arrhythmias and are characterized by severely altered calcium (Ca^{2+}) handling in cardiac myocytes. However, the Ca^{2+}-dependent mechanisms underlying cardiac arrhythmia initiation are not well understood.

In this work, mathematical models were developed to investigate the molecular mechanisms of pathological Ca^{2+} dynamics in ventricular cardiac myocytes. A biophysically-detailed three-dimensional model of a subcellular Ca^{2+} release site was used to study mechanisms of spontaneous spatially-confined Ca^{2+} release events, known as Ca^{2+} "sparks," which underlie cell-wide Ca^{2+} release and arrhythmogenic Ca^{2+} waves. It revealed a correlation between Ca^{2+} spark frequency and the maximum eigenvalue of the adjacency matrix describing the Ca^{2+} release channel lattice. This relationship was further investigated using a mathematical contact network model describing the Ca^{2+} spark initiation process.

A multiscale model of a 1D fiber of myocytes was also developed to investigate the mechanisms of ectopic excitation of cardiac tissue. The model was used to study the stochastic variability of delayed afterdepolarizations caused by spontaneous propagating waves of Ca^{2+} sparks. Large delayed afterdepolarizations triggered ectopic beats probabilistically due to the stochasticity of Ca^{2+} release channel gating. A novel method was developed to estimate the probability of rare arrhythmic events.

Academic Advisor and Mentor:

Raimond L. Winslow, Raj and Neera Singh Professor, Department of Biomedical Engineering, The Johns Hopkins University

Thesis Committee and Co-Advisor:

Joseph L. Greenstein, Associate Research Scientist, Institute for Computational Medicine, The Johns Hopkins University

Thesis Committee Chair:

Natalia Trayanova, Murray B. Sachs Professor, Department of Biomedical Engineering, The Johns Hopkins University

Acknowledgements

Thank you to my friends and family for their unwavering encouragement and support, especially my parents Martha and Bill for all the opportunities you have made possible and my big brother Jeff for always inspiring me. Also thank you to my labmates, former and current, for being there with me every step of the way.

To my advisor and mentor Dr. Rai Winslow: I could not have asked for a better experience as a graduate student. Thank you for granting me the freedom to explore intellectually and professionally. Your support has given me the skills and confidence I need to achieve success.

To my co-advisor Dr. Joe Greenstein: Thank you for the conversations, both scientific and non. Your laid-back attitude and words of encouragement always kept me at ease even in stressful times.

Thank you to Dr. Natalia Trayanova for serving as chair of the thesis committee and for your insightful feedback on this work. Also thank you to all of my collaborators, especially Drs. Jeremy Rice, Slava Gurev, Blair Williams, Tobias Kohl, and Ravi Madduri. This work would not have been possible without you.

Finally, thank you to Melissa for always believing in me and making life awesome.

Table of Contents

Chapter 1 Introduction 1

- 1.1 Cardiomyocyte Calcium Dynamics 1
- 1.2 Cellular Arrhythmias 4
- 1.3 Reproducible Research in Computational Modeling..5

Chapter 2 Superresolution Calcium Spark Model 8

- 2.1 Model Description 8
  - 2.1.1 Geometry..8
  - 2.1.2 Transport Equations 11
  - 2.1.3 Ion Channels 12
  - 2.1.4 Numerical Methods and Implementation..13
  - 2.1.5 Spark Analysis 14
  - 2.1.6 Spectral Analysis of RyR Clusters...14
- 2.2 Results...15
  - 2.2.1 Model Validation 15
  - 2.2.2 The Life and Death of Ca^{2+} Sparks 18
  - 2.2.3 Direct $[Ca^{2+}]_{jsr}$-dependent Regulation of RyRs 19
  - 2.2.4 Subspace Geometry 23
  - 2.2.5 RyR Cluster Structure 27
  - 2.2.6 Spectral Analysis of RyR Cluster Structure......................................30
- 2.3 Discussion 33
  - 2.3.1 RyR Cluster Spectral Properties 33
  - 2.3.2 $[Ca^{2+}]_{jsr}$-dependent Regulation...34

2.3.3 Physiological and Pathophysiological Significance 35
2.4 Conclusion 39
Chapter 3 RyR Contact Network Model...40
3.1 Model Description 40
3.2 Results...46
3.2.1 Ca^{2+} Diffusion in the CN Model 46
3.2.2 Linear Mean-Field CN Model 49
3.2.3 Characterization of Subdomains by the Eigenmodes 53
3.2.4 Perturbation Analysis...57
3.3 Discussion...60
3.4 Conclusion 68
Chapter 4 Stochastic Tissue Model..69
4.1 Superresolution Modeling of Release Site Coupling......................................69
4.2 Model Description 72
4.2.1 Ventricular Myocyte Model...72
4.2.2 Fiber model 76
4.2.3 Beta-adrenergic stimulation...76
4.3 Results...78
4.3.1 Cell Model Properties 78
4.3.2 Delayed afterdepolarizations during pacing 80
4.3.3 Effect of SR Ca^{2+} load on DADs 83
4.3.4 Dependence of DAD distribution on total cell Ca^{2+} and I_{K1} density 88

4.3.5 Probabilistic triggered activity in a paced fiber of myocytes 91

4.3.6 Roles of Ca^{2+} loading, I_{K1} density, and g_{gap} in fiber DADs 94

4.3.7 Overview of method for estimating rare event probabilities 96

4.3.8 Filtering method for estimating V_{max} from J_{RyR} 96

4.3.9 Resampling method for estimating rare event probabilities 101

4.3.10 Prediction of rare events 104

4.4 Discussion 107

4.5 Conclusion 109

Chapter 5 Models and Simulations as a Service 111

5.1 Tool Description 111

5.1.1 Globus Galaxies 111

5.1.2 Tool Development 111

5.2 Results 113

5.2.1 SRS Model Tools 113

5.2.2 XML-encoded Model Tools 117

5.2.3 Hodgkin-Huxley Model Composition 120

5.3 Discussion 122

5.4 Conclusion 124

Chapter 6 Conclusion and Future Directions 125

List of Tables

Table 4.1 Parameters used for filtering method in Figure 4.10. 100

Table A.1 Diffusion Coefficients.. 128

Table A.2 Initial Conditions 128

Table A.3 Buffering Parameters 128

Table A.4 RyR Gating Parameters... 129

Table A.5 SERCA and JSR Transport Parameters 129

Table C.1 Release Site Ca^{2+} Transport Parameters 140

List of Figures

Figure 2.1 Model geometry diagrams. 10

Figure 2.2 Representative Ca^{2+} sparks and RyR gating properties. 17

Figure 2.3 Effects of SR load on SR Ca^{2+} leak and ECC gain. 22

Figure 2.4 Effects of increasing the distance between TT and JSR membranes. 25

Figure 2.5 Effects of JSR diameter on SR Ca^{2+} leak. 26

Figure 2.6 Spark fidelity of RyR cluster geometries inferred from STED nanoscopy images. 29

Figure 2.7 Correlation between maximum eigenvalue λ_{max} of the RyR cluster adjacency matrix and spark fidelity. 32

Figure 3.1 The contact network model reproduces RyR channel gating during Ca^{2+} spark initiation. 44

Figure 3.2 Dependence of δ/β on biophysical properties of the Ca^{2+} release site. 48

Figure 3.3 The expected number of open channels in the linearized mean-field CN (LCN) model predicts spark probability. 52

Figure 3.4 Intra-cluster spatial gradients in spark probability are characterized by one or two eigenmodes. 56

Figure 3.5 Perturbation analysis of lattice structure. 59

Figure 3.6 Dependence of λ_1 and Ca^{2+} spark probability on RyR cluster image interpretation. 67

Figure 4.1 Superresolution model of two Ca^{2+} release sites. 71

Figure 4.2 Multiscale cell and tissue model schematics. 75

Figure 4.3 Cell model properties. 79

Figure 4.4 DADs induced by Ca^{2+} overload during 1 Hz pacing in the myocyte model. 82

Figure 4.5 Elevating SR Ca^{2+} load accelerated Ca^{2+} wave formation and increased DAD amplitude. 84

Figure 4.6 Variability of DAD timing and amplitude in five independent model realizations with identical initial conditions. 87

Figure 4.7 Roles of total cell Ca^{2+} and I_{K1} density in DAD distribution. 90

Figure 4.8 Probabilistic triggered activity caused by DADs in the fiber model....... 93

Figure 4.9 Roles of initial $[Ca^{2+}]_i$, I_{K1} density, and g_{gap} in DAD variability in the fiber model. 95

Figure 4.10 Filtering method for estimating V_{max} from the spatiotemporal J_{RyR} profile in a fiber. 99

Figure 4.11 Method for estimation of rare extreme DAD probabilities. 103

Figure 4.12 Realizations of rare extreme DADs.. 106

Figure 5.1 Spark simulation from the SRS model. 116

Figure 5.2 Use of XML-encoded models in Galaxy. 119

Figure 5.3 Model composition of the Hodgkin-Huxley squid giant axon model using Galaxy workflows. 121

Chapter 1 Introduction

Sudden cardiac death (SCD) occurs following the unexpected onset of a cardiac arrhythmia and accounts for an estimated 180-400,000 deaths per year in the US (1). Heart failure (HF) affects 8.4M individuals in the US (2) and increases the likelihood of SCD 6- to 9-fold (3). Other forms of heart disease including hypertrophic cardiomyopathy (4), long QT syndrome (5), and catecholaminergic polymorphic ventricular tachycardia (CPVT) (6) are also significant risk factors for SCD. These diseases are characterized by alterations to calcium (Ca^{2+}) handling in cardiac myocytes that predispose the heart to arrhythmogenesis. However, the mechanisms contributing to the initiation of cardiac arrhythmias remain incompletely understood.

1.1 Cardiomyocyte Calcium Dynamics

Contraction of the cardiac myocyte is driven by a process known as excitation-contraction coupling (ECC), which is initiated at Ca^{2+} release units (CRUs) when individual L-type Ca^{2+} channels (LCCs) open in response to membrane depolarization. These events produce Ca^{2+} flux into a narrow subspace formed by the t-tubule (TT) and junctional sarcoplasmic reticulum (JSR) membranes. The resulting increase in subspace Ca^{2+} concentration ($[Ca^{2+}]_{ss}$) leads to opening of Ca^{2+}-sensitive Ca^{2+} release channels, known as ryanodine receptors (RyRs), located in the JSR membrane, producing additional flux of Ca^{2+} into the subspace. These two sources of Ca^{2+} flux generate an intracellular Ca^{2+} transient that triggers cardiac muscle contraction. Studying the mechanisms of this Ca^{2+}-induced Ca^{2+} release (CICR) process is therefore critical to understanding healthy and diseased cardiac muscle function.

Individual release events, referred to as "Ca^{2+} sparks," can be visualized using fluorescent Ca^{2+} indicators and confocal microscopy (7, 8). Spontaneous Ca^{2+} sparks are observed in resting myocytes and during diastole. A Ca^{2+} spark occurs when a RyR opens spontaneously and causes a local rise in $[Ca^{2+}]_{ss}$ that triggers the rest of the RyR cluster. Recently, it has been shown that diastolic Ca^{2+} sparks contribute to sarcoplasmic reticulum (SR) Ca^{2+} leak (9), which balances Ca^{2+} uptake into the SR by the SR Ca^{2+}-ATPase (SERCA) pump. In addition, RyRs can mediate Ca^{2+} leak in the absence of Ca^{2+} sparks (9, 10). The spontaneous opening of a single RyR may fail to trigger the rest of the RyR cluster, thus releasing only a small amount of Ca^{2+} (11, 12). This type of event is known as a "Ca^{2+} quark," and it results in a phenomenon referred to as "invisible" Ca^{2+} leak because its fluorescence signal is too small to detect with $[Ca^{2+}]_i$ indicator dyes (13). Invisible leak may originate from RyRs located in clusters or from non-junctional "rogue" RyRs (14).

Spark fidelity, or the probability that a single RyR opening triggers a Ca^{2+} spark, is a property of the RyR cluster, and it is strongly influenced by RyR gating properties. In particular, the sensitivity of the RyR to $[Ca^{2+}]_{ss}$ critically influences spark fidelity. When a RyR opens, neighboring RyRs sense the steep $[Ca^{2+}]_{ss}$ gradient from the open channel. If $[Ca^{2+}]_{ss}$ sensitivity is very high, openings are very likely to recruit nearby RyRs, whereas low sensitivity to $[Ca^{2+}]_{ss}$ results in fewer Ca^{2+} sparks. Previously, single-channel studies in artificial lipid bilayers found that the EC_{50} for RyR open probability was in the range of 1-25 μM (15). However, more recent experiments have shown that this range is likely much higher (45-85 μM) in the presence of physiological $[Mg^{2+}]$, [ATP], and JSR Ca^{2+} concentration ($[Ca^{2+}]_{jsr}$) (16-18). There are a multitude of mechanisms that modulate RyR gating. A large body of work suggests that $[Ca^{2+}]_{jsr}$ controls sensitivity to $[Ca^{2+}]_{ss}$ (15, 17, 19-21). The physiological role of $[Ca^{2+}]_{jsr}$-dependent regulation is controversial, but recent single-channel studies have concluded that $[Ca^{2+}]_{jsr}$-dependent regulation is weak in rat and mouse in the physiological range of $[Ca^{2+}]_{jsr}$ (0.1-1 mM) (16, 17). There is also evidence that the JSR load affects RyR activity during Ca^{2+} sparks by controlling the unitary RyR current amplitude, which would influence the $[Ca^{2+}]_{ss}$ gradient during channel opening (11, 16, 22). Other regulatory mechanisms include the effects of protein kinase A (23, 24), Ca^{2+} /calmodulin-dependent kinase II (CaMKII) (25, 26), allosteric coupling (27, 28), redox modifications (29), and genetic mutations associated with CPVT (17, 30, 31). The role of CRU geometry in Ca^{2+} spark fidelity has been studied using compartmental models (32, 33), but has yet to be addressed with a detailed 3D model.

The cardiac CRU is formed by the JSR, a flattened cisternal extension of the SR ~30 nm thick that wraps around the TT, forming a narrow subspace ~12- 20 nm in width. In recent years, viewpoints on the packing of RyRs within the subspace have evolved. Franzini-Armstrong et al. observed densely packed RyR “foot” structures in the subspace using electron microscopy and estimated large cluster sizes in excess of 100 RyRs (34). However, recent super-resolution fluorescence microscopy techniques showed heterogeneous peripheral RyR cluster shapes with unprecedented detail, and quantitative analysis confirmed that RyR cluster sizes are exponentially distributed. Of note, the majority of RyR channels were organized in clusters of ~25 RyRs in rat myocytes (35). Breakthroughs in electron microscope tomography have led to detailed 3D reconstructions of the TT and SR ultrastructure, revealing that the geometry of the subspace is also heterogeneous due to the irregular shape of the SR membrane (36, 37). Remodeling of the JSR (38, 39) and TT (40, 41) have also been observed in models of chronic HF. Despite these new data, the functional roles of subspace and RyR cluster geometry remain unclear and cannot be directly investigated through current experimental methods and technologies.

1.2 Cellular Arrhythmias

Under conditions promoting cellular Ca^{2+} overload, Ca^{2+} sparks can trigger the RyRs at nearby release sites and form a propagating Ca^{2+} wave(42). During this spontaneous Ca^{2+} release event, Ca^{2+} is removed from the cell through the Na+/Ca^{2+} exchanger (NCX), which transports 3 Na+ ions into the cell for every Ca^{2+} ion extruded out. This produces a net inward current, resulting in an inflection in the cell membrane potential known as a delayed afterdepolarization (DAD)(43). DADs of sufficient amplitude can lead to the activation of the fast Na+ current (I_{Na}) to trigger an AP. Gap junctions joining adjacent cells then conduct the AP across the myocardial syncytium. Such ectopic events in the heart can induce reentrant ventricular arrhythmias that lead to sudden cardiac death(44). Furthermore, propensity for exhibiting spontaneous Ca^{2+} release is increased in heart diseases such as HF and some forms of long-QT syndrome, which are associated with increased risk for sudden cardiac death. Therefore understanding of Ca^{2+} dynamics in ventricular myocytes and the Ca^{2+} handling instability that arises under pathological conditions are fundamental to our understanding of cardiac arrhythmogenesis.

Experimental studies have observed triggered activity under conditions evoking spontaneous Ca^{2+} release in myocardial wedge preparations(45) and whole heart(46, 47). These studies showed that the likelihood of observing of ectopic foci is correlated with the amount of Ca^{2+} loading. In isolated myocytes, Ca^{2+} waves are observed when the SR Ca^{2+} load achieves a critical level(48). However, electrotonic coupling in tissue attenuates DAD amplitude by draining inward current to adjacent myocytes through the gap junctions. Wasserstrom et al. reported that by increasing SR Ca^{2+} load, spontaneous Ca^{2+} waves exhibited greater synchrony following cessation of rapid pacing in intact heart(47). Synchronous DADs would result in smaller spatial gradients in membrane potential, less inward current flowing into neighboring cells, and therefore larger DAD amplitude. The mechanism of synchronization and factors affecting the likelihood of triggered activity are not well understood.

1.3 Reproducible Research in Computational Modeling

Computational modeling is now an essential tool for studying a wide range of biological systems. As knowledge of these systems deepens, models have become increasingly multi-scale, complex, and computationally demanding. Publication of such models is challenging because transcribing equations and parameter values from model software into publications is error prone. XML-based model description languages such as SBML (49) and CellML (50) have been developed to address some of these challenges. These languages separate the description of models from the details underlying their implementation and execution. Once models are correctly encoded, they may be distributed in an error-free manner for machine interpretation. To enable reproduction of published results, authors must also disseminate the simulation details of each *in silico* experiment.

The scope of existing model description languages and their associated computational tools limits them for use with certain classes of models. SBML Level 3 describes biochemical reaction networks and their kinetic laws (49). It has been widely adopted by the systems biology community, and other infrastructure such as the BioModels Database (51) have been built around this standard. CellML describes models formulated as differential-algebraic equations (52), and the CellML Model Repository contains descriptions of over 500 models. Tools such as Copasi (53) and OpenCOR (54) can import SBML and CellML model descriptions and solve the underlying model equations.

Many different types of mathematical representations may encompass a given model as they become increasingly multi-scale. For example, our super-resolution spark (SRS) model presented in Chapter 2 can be used to study mechanisms underlying the generation of Ca^{2+} sparks. While some model components can be described using existing markup languages (e.g., ion channels and membrane transporters), the integrated model cannot. Simulations require definition of a model geometry and channel placement in that geometry, and solution of a reaction-diffusion equation in which some components of the reaction term require Monte Carlo simulations of stochastic channel gating, while others require solution of ordinary differential equations. Given the nature of this and many other highly complex multi-scale biological models, we believe it is important to consider complementary methods and technologies that make computational models accessible to users, and that enable modelers to systematically document their work so that it can be reproduced by others.

Galaxy (55) is a web-based platform for conducting data-intensive biomedical research that has been widely adopted by genomics researchers. Galaxy provides users access to data, analysis algorithms, and computational resources on which analyses are performed. All capabilities are accessed solely through the user’s web-browser. Galaxy instances are highly customizable, and extensible new tools can be created or imported from the Galaxy Tool Shed - an open repository of applications contributed by the community (56). Galaxy is a reproducible research system (RRS) that automatically tracks and records details of analyses, allows the construction of complex workflows, and permits results to be documented, shared, and published with complete provenance, helping to assure transparency and reproducibility of research. Galaxy is also a workflow composition system (WCS) that allows sequential steps of data reads/writes and data analyses to be assembled in a modular fashion using its graphical interface.

Chapter 2 Superresolution Calcium Spark Model

2.1 Model Description

Here we present a detailed three-dimensional model of a cardiac Ca^{2+} release unit that incorporates diffusion, intracellular buffering systems, and stochastically gated ion channels. The model exhibits realistic Ca^{2+} sparks and robust Ca^{2+} spark termination across a wide range of geometries and conditions. Furthermore, the model captures the details of Ca^{2+} spark and non-spark based SR Ca^{2+} leak and produces normal excitation-contraction coupling gain.

The model simulates local Ca^{2+} dynamics with a spatial resolution of ~10 nm over the course of individual release events (~100 ms). It is based on the previous work of Williams et al. (12) and incorporates major biophysical components, including stochastically gated RyRs and LCCs, spatially organized TT and JSR membranes, and other important elements such as mobile buffers (calmodulin, ATP, fluo-4), immobile buffers (troponin, sarcolemmal membrane binding sites, calsequestrin), and the SERCA pump. The three-dimensional geometry was discretized on an unstructured tetrahedral mesh and solved using a cell-centered finite volume scheme. Parameter values and additional equations are given in 0.

2.1.1 Geometry

The simulation domain is a 64 μm^3 cube (64 fL) with no-flux conditions imposed at the boundaries. The CRU geometry consists of the TT and JSR membranes (Figure 2.1*A*). The TT is modeled as a cylinder 200 nm in diameter (41) that extends along the z-axis of the domain. Unless otherwise noted, we used a nominal geometry where the JSR is a square “pancake” 465 nm in diameter that wraps around the TT (57), forming a dyadic space 15 nm in width. The thickness of the JSR is 40 nm and has a total volume of 10^{-17} L. RyRs are treated as point sources arranged in the subspace on a lattice with 31 nm spacing, and the LCCs are located on the surface of the TT. The nominal CRU model contains a square 7×7 array of RyRs and 7 LCCs distributed evenly over the RyR cluster (Figure 2.1*B*). The SERCA pump and troponin buffering sites are homogeneously distributed in the cytosol beyond a radius of 200 nm from the TT axis.

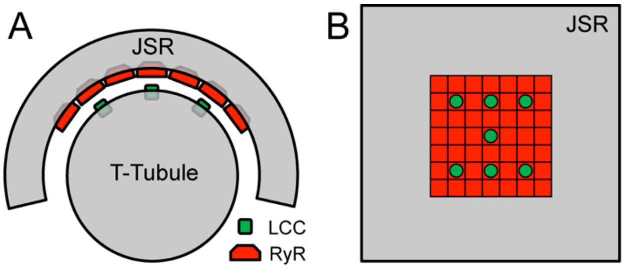

Figure 2.1 Model geometry diagrams.

(A) Cross-sectional diagram of the model geometry and arrangement of ion channels and membrane structures. The TT is modeled as a cylinder 200 nm in diameter and is partially encircled by the JSR, forming a subspace 15 nm in width. The ion channels are treated as point sources and do not occupy any volume in the subspace. (B) Schematic of flattened JSR (*gray*) with the arrangement of a 7×7 lattice of RyRs with 31 nm spacing (*red*) and LCCs distributed over the cluster (*green*). The depicted JSR membrane is 465 nm in diameter

2.1.2 Transport Equations

The Ca^{2+} diffusion and buffering system is based on a previous spark model by Hake et al. (58). The reaction-diffusion equation for Ca^{2+} is given by

$$\beta \frac{\partial [Ca^{2+}]}{\partial t} = D_{Ca} \nabla^2 [Ca^{2+}] + \sum_i J_i \,, \tag{2.1}$$

where β is the dynamic buffering fraction due to sarcolemmal binding sites and D_{Ca} is the diffusion coefficient. The J_i terms represent sources of Ca^{2+}, including additional buffers, RyR and LCC fluxes, and SERCA uptake. Diffusion of mobile buffers (ATP, calmodulin, fluo-4) is modeled using similar transport equations. Each buffer B (excluding sarcolemmal binding sites) is assumed to bind to Ca^{2+} according to elementary rate laws given by

$$J_B = k_{off}[CaB] - k_{on}[B][Ca^{2+}], \tag{2.2}$$

where and k_{on} and k_{off} are reaction rate constants, and $[CaB]$ is the concentration of Ca^{2+}-bound buffer. Concentration balance equations and the values of the diffusion coefficients, reaction rate constants, and buffer concentrations are provided in 0. The LCC (59) and SERCA (60) flux formulations are adapted from previous work. $[Ca^{2+}]_{jsr}$ is modeled spatially in the JSR with the same diffusion coefficient as in the cytosol. The network SR (NSR) Ca^{2+} concentration ($[Ca^{2+}]_{nsr}$) is assumed to be constant. JSR Ca^{2+} is refilled by the NSR at each element in the JSR volume with a flux term given by

$$J_{refill} = v_{refill}\left([Ca^{2+}]_{nsr} - [Ca^{2+}]_{jsr}\right), \tag{2.3}$$

where v_{refill} is a constant that was adjusted to achieve a refill time constant of ~130 ms (61). Refilling of the JSR throughout its volume is unlikely to have significant impacts on $[Ca^{2+}]_{jsr}$ dynamics, as JSRs typically have ~4 connections to the NSR (57).

Negatively charged phospholipid head groups on the inner sarcolemmal membrane surface are known to exert significant electrostatic effects on $[Ca^{2+}]_{ss}$ dynamics (62). However, the Debye length for the electric field at the membrane is ~1 nm, which would have required much higher spatial resolution. This was computationally prohibitive to include in this model due to the small time steps required. Instead, a rapid buffering approximation was used for Ca^{2+} binding to high affinity sarcolemmal binding sites described in Peskoff et al. (63) (see 0).

2.1.3 Ion Channels

RyRs and LCCs are simulated stochastically using Markov chains. The LCC model used here was described previously in (59). The RyR is a minimal, two-state Markov chain that incorporates activation by $[Ca^{2+}]_{ss}$ and $[Ca^{2+}]_{jsr}$-dependent regulation of the opening rate (12). State transitions are determined according to a fixed closing rate (*k*-) and an opening rate given by

$$r_{open} = k^{+}\phi[Ca^{2+}]_{ss}^{\eta}, \tag{2.4}$$

where k^{+} is the opening rate constant, ϕ represents a $[Ca^{2+}]_{jsr}$-dependent regulation term, and η is a constant. The unitary RyR Ca^{2+} flux is given by

$$J_{ryr} = v_{ryr}\left([Ca^{2+}]_{jsr} - [Ca^{2+}]_{ss}\right), \tag{2.5}$$

where v_{ryr} is a constant. The values of k^{+}, η, and v_{ryr} were adjusted to yield physiological resting Ca^{2+} spark frequency and leak rate at 1 mM $[Ca^{2+}]_{jsr}$. A narrow range of these parameters yielded a realistic spark rate for rat of ~100 $cell^{-1}$ s^{-1}. The value of v_{ryr} was adjusted to a unitary current of 0.15 pA at 1 mM $[Ca^{2+}]_{jsr}$. The ϕ term is an empirical power function given by

$$\phi = \phi_b + \left([Ca^{2+}]_{jsr}/\phi_k\right)^4, \tag{2.6}$$

where ϕ_b and ϕ_k are constants. At 1 mM $[\mathrm{Ca}^{2+}]_{\mathrm{jsr}}$, P_O at diastolic $[\mathrm{Ca}^{2+}]_{\mathrm{ss}}$ (100 nM) is extremely low (1.76×10^{-6}), and the EC_{50} for activation is 55 μM. We assumed that $[\mathrm{Ca}^{2+}]_{\mathrm{jsr}}$ strongly regulates P_O (64) such that at 2 mM $[\mathrm{Ca}^{2+}]_{\mathrm{jsr}}$, the EC_{50} decreases to 29 μM. In accordance with recent data (16, 17), however, we assumed that the $[\mathrm{Ca}^{2+}]_{\mathrm{jsr}}$ weakly regulates the RyR when $[\mathrm{Ca}^{2+}]_{\mathrm{jsr}}$ is below 1 mM such that the EC_{50} does not change significantly. In cases where $[\mathrm{Ca}^{2+}]_{\mathrm{jsr}}$-dependent regulation was assumed to be absent, $\phi=1$, which corresponds to the effect of a resting level of 1 mM $[\mathrm{Ca}^{2+}]_{\mathrm{jsr}}$ on RyR opening rate when this regulation is intact.

2.1.4 Numerical Methods and Implementation

The simulation domain was discretized with an unstructured mesh consisting of ~12,000 tetrahedral elements and was generated using Tetgen (65). The transport PDEs were solved in space using a cell-centered finite volume scheme for unstructured grids and explicitly in time using the first-order Euler method. For the nominal model geometry, numerical stability and solution convergence was achieved for time steps < 47 ns. We utilized a 12 ns time step, which ensured both stability and accuracy across all tested CRU geometries. RyR and LCC gating models were simulated using the method described by Alfonsi et al. (66) (see SI text). A Galaxy (55) toolset was developed for the model, allowing users to explore sample datasets and run simulations with customized CRU geometries and model parameters on a cloud-based service. Example workflows are available for performing linescan simulations, Ca^{2+} spark fidelity and leak estimation, and ECC gain estimation. The tools can be found under the "Calcium Spark" model and the example histories and workflows under "Shared Data" at: http://cvrg.galaxycloud.org.

2.1.5 Spark Analysis

Linescans were generated by convolving a Gaussian point spread function with the Ca^{2+}-bound indicator dye concentration, as described in Smith et al. (67), and the raw fluorescence signal was normalized to the baseline signal (F_0). Gaussian noise was superimposed to resemble intrinsic photon noise. Spark kinetics and morphology were computed using Sparkmaster (68). Methods used to estimate Ca^{2+} spark fidelity, rate, leak, and ECC gain are given in the SI text. Unless otherwise noted, each plotted data point is derived from an ensemble of at least 1,000 independent simulations.

2.1.6 Spectral Analysis of RyR Clusters

RyR clusters were defined by the channel positions on a 2D lattice. For a given cluster with N channels, we define the $N \times N$ adjacency matrix $\mathbf{A}$ with elements $a_{ij} = 1$ if RyRs i and j are adjacent, and 0 otherwise. This represents a graph where vertices represent RyRs and edges represent adjacency. It is well-known that the spectrum of the adjacency matrix of a graph contains valuable information about its structural properties (69). We computed $\mathbf{A}$ for a collection of RyR cluster geometries to show that its maximum eigenvalue λ_{max} is a reliable predictor of spark fidelity.

2.2 Results

2.2.1 Model Validation

To validate the model, a nominal parameter set and geometry were selected to produce a representative Ca^{2+} spark with realistic appearance, frequency, and integrated flux. The Ca^{2+} spark was initiated by holding a RyR open for 10 ms. The linescan simulation exhibited a time-to-peak of 10 ms, full-duration at half maximum of 24 ms, and full-width at half maximum (FWHM) of 1.65 μm (Figure 2.2*A*). The width is slightly lower than what is observed experimentally (1.8- 2.2 μm), but this discrepancy could not be remedied by increasing release flux or altering the CRU geometry. This "Ca^{2+} spark width paradox" is difficult explain using mathematical models (16, 67, 70), but it may be due to non-Fickian diffusion in the cytosol (71). $[Ca^{2+}]_{ss}$ at the center of the subspace peaked at 280 μM, and optical blurring decreased peak F/F_0 6-fold due to the small volume of the subspace (data not shown). The local $[Ca^{2+}]_{ss}$ transients in the vicinity of an open RyR were similar to that shown for a 0.2 pA source in previous work that incorporated electrodiffusion and the buffering effects of negatively charged phospholipid heads of the sarcolemma (62) (data not shown).

The model was also constrained to reproduce whole-cell Ca^{2+} spark rate and overall SR Ca^{2+} leak. The Ca^{2+} spark frequency at 1 mM $[Ca^{2+}]_{jsr}$ was estimated to be 133 $cell^{-1}$ s^{-1} (see 0), which is in agreement with the observed Ca^{2+} spark rate of ~100 $cell^{-1}$ s^{-1} in rat (72). The leak rate of 1.01 μM s^{-1} is also close to that of a previous model of the rat myocyte used to study SERCA pump-leak balance (12) and is consistent with an experimental study in rabbit (9).

ECC gain was estimated for a 200 ms membrane depolarization at test potentials from -20 to 60 mV in 20 mV steps. The gain was then computed as ratio of peak total RyR flux to peak total LCC flux. ECC gain decreased from 20.7 at -20 mV to 1.5 at 60 mV, in reasonable agreement with experimental studies (73). This validation was achieved without further fitting of the model parameters.

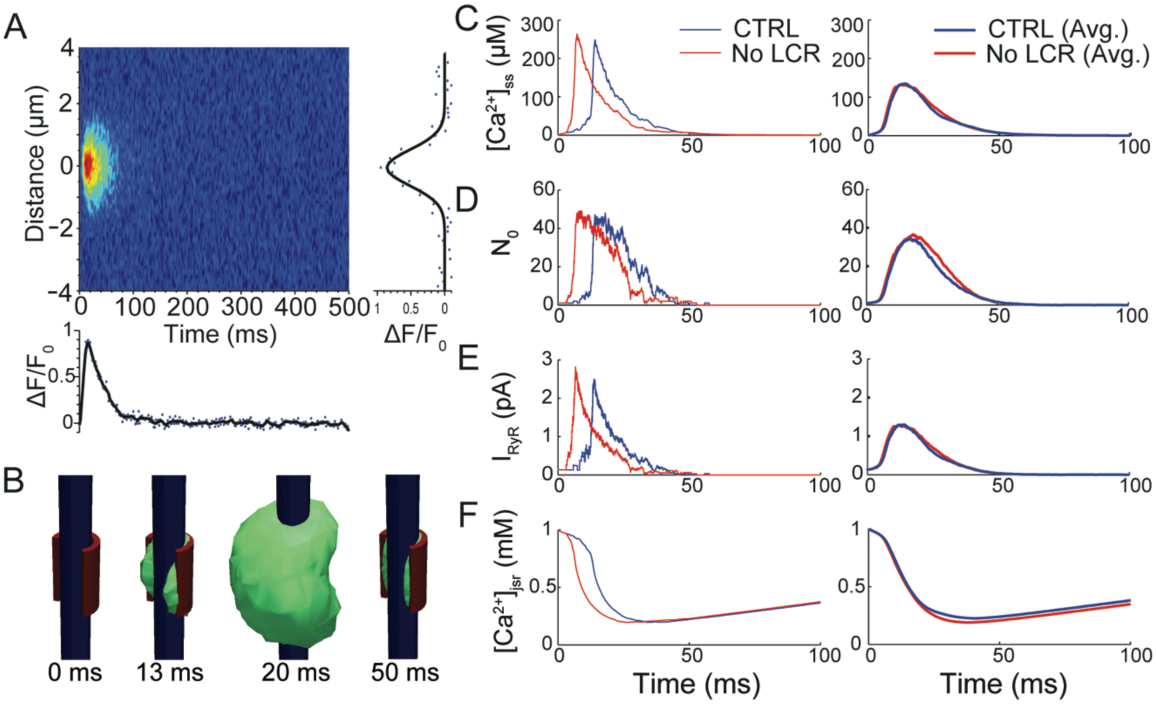

Figure 2.2 Representative Ca^{2+} sparks and RyR gating properties.

(A) Simulated linescan of Ca^{2+} spark (with $[Ca^{2+}]_{jsr}$-dependent regulation) shown with the temporal fluorescence profile through the center of the spark (*bottom*), and the spatial fluorescence profile at the peak of the spark (*right*). (B) Three-dimensional renderings of the Ca^{2+} spark showing TT (*blue*), JSR (*red*), and 1 μM $[Ca^{2+}]_i$ isosurface (*green*). The presence of the JSR membrane causes noticeable asymmetry in the $[Ca^{2+}]_i$ gradient throughout the spark. (C) Average $[Ca^{2+}]_{ss}$, (D) number of open RyRs, and (E) total RyR current, and (F) average $[Ca^{2+}]_{jsr}$ with (*blue*) and without (*red*) $[Ca^{2+}]_{jsr}$-dependent regulation during a spark initiated at t = 0 ms. Left panels show traces for single representative sparks, and right panels show averages of at least 100 sparks. Note that the peaks of the averages were lower due to variability in spark activation timing. An example Ca^{2+} spark dataset can be viewed at: http://cvrg.galaxycloud.org/u/mwalker/h/spark-linescan.

2.2.2 The Life and Death of Ca^{2+} Sparks

The model provides new insights into local Ca^{2+} signaling during release. Figure 2.2*B* shows the asymmetrical profile of the 1 μM cytosolic Ca^{2+} concentration ($[Ca^{2+}]_i$) isosurface during a spark. Linescan simulations with scans parallel to the TT (z-direction), orthogonally through the center of the subspace (x-direction), and in the y-direction exhibited FWHMs of 1.65, 1.50, and 1.35 μm, respectively, but showed no significant asymmetry in their respective spatial profiles (data not shown). The presence of the JSR caused noticeable rotational asymmetry in $[Ca^{2+}]_i$, however, particularly on the back face of the JSR, where $[Ca^{2+}]_i$ reaches ~1 – 4 μM. Shrinking the JSR lessened this effect on the $[Ca^{2+}]_i$ isosurface, but still resulted in an uneven distribution during release. $[Ca^{2+}]_i$ outside the CRU reached ~10 μM on the side opposite the JSR due to lower resistance to diffusion. These results highlight the importance of accounting for the nanoscopic structure of the CRU in studying localized Ca^{2+} signaling in microdomains.

During Ca^{2+} spark initiation, a rise in local $[Ca^{2+}]_{ss}$ around an open channel triggers the opening of nearby RyRs, resulting in a rapid increase in average $[Ca^{2+}]_{ss}$ (Figure 2.2*C*) and the sustained opening of the entire cluster of RyRs (Figure 2.2*D*). Note that release continues for over 50 ms, despite much shorter spark duration in the linescan. This is explained by the decline in release flux (Figure 2.2*E*) due to emptying of JSR Ca^{2+} over the course of the Ca^{2+} spark (Figure 2.2*F*). When $[Ca^{2+}]_{jsr}$ reaches ~0.2 mM, the declining $[Ca^{2+}]_{ss}$ can no longer sustain RyR re-openings, and the Ca^{2+} spark terminates. This indirect $[Ca^{2+}]_{jsr}$-dependent regulation of the RyR is critical to the process by which CICR can terminate. Figure 2.2 *C* - *F* also shows sparks where $[Ca^{2+}]_{jsr}$-dependent regulation was removed, in which case spark dynamics were very similar and termination still occurred. This is not surprising given that $[Ca^{2+}]_{jsr}$ dependent regulation below 1 mM was weak in this model. The release extinction time, defined as the time from the first RyR opening to the last RyR closing, was marginally higher on average without $[Ca^{2+}]_{jsr}$-dependent regulation (56.4 vs. 51.5 ms). Our data clearly show that Ca^{2+} sparks terminate via stochastic attrition facilitated by the collapse of $[Ca^{2+}]_{ss}$ due to localized luminal depletion events (i.e., Ca^{2+} blinks). Importantly, this conclusion is consistent with our earlier models (12, 70, 74, 75) and in agreement with recent models by Cannell et al. (16) and Gillespie & Fill (76). However, it is not clear that naming this existing termination mechanism to something such as "induction decay" or "pernicious attrition" provides additional insight beyond a simple acronym such as STOP (Stochastic Termination On Ca^{2+} dePletion). Regardless, the critical role played by $[Ca^{2+}]_{jsr}$ depletion in Ca^{2+} spark termination is clear, and this depletion must be robust enough for $[Ca^{2+}]_{ss}$ to decrease sufficiently so that spontaneous closings of active RyRs outpaces Ca^{2+}-dependent re-openings.

2.2.3 Direct $[Ca^{2+}]_{jsr}$-dependent Regulation of RyRs

The role of direct $[Ca^{2+}]_{jsr}$-dependent regulation on RyR gating remains controversial. As shown in the previous section, we found that such regulation is not essential for Ca^{2+} spark termination. To see how this mechanism influences cell function, we investigated its effects on spark fidelity, Ca^{2+} spark rate, leak, and ECC gain over varying SR loads.

Experimental studies have demonstrated that Ca^{2+} spark frequency and SR Ca^{2+} leak rate increase exponentially at elevated $[Ca^{2+}]_{jsr}$ (9, 77, 78). There are two intrinsic factors contributing to the exponential rise. First, higher $[Ca^{2+}]_{jsr}$ results in larger concentration gradients across the JSR membrane, thereby increasing the unitary current of the RyR. This accelerates the $[Ca^{2+}]_{ss}$ rising rate and thus perpetuates release from other RyRs. Second, higher SR loads also increase the amount of Ca^{2+} released per Ca^{2+} spark, contributing to increased Ca^{2+} spark-based leak. $[Ca^{2+}]_{jsr}$-dependent regulation introduces two additional mechanisms that contribute to increased Ca^{2+} spark frequency. First, $[Ca^{2+}]_{jsr}$-dependent regulation of the RyR enhances its sensitivity to $[Ca^{2+}]_{ss}$ at higher $[Ca^{2+}]_{jsr}$, increasing the likelihood that the cluster will be triggered. Second, the enhanced Ca^{2+} sensitivity also increases the frequency of spontaneous Ca^{2+} quarks (12).

To elucidate the importance of $[Ca^{2+}]_{jsr}$-dependent regulation in the SR leak-load relationship, we tested two versions of the model with and without it. In the case without it, $\phi = 1$, so that Ca^{2+} spark frequency and leak are still properly constrained at 1 mM $[Ca^{2+}]_{jsr}$. Spark fidelity and the total Ca^{2+} released per Ca^{2+} spark were estimated from an ensemble of simulations of independent CRUs, from which Ca^{2+} spark frequency and SR Ca^{2+} leak rate could be estimated for $[Ca^{2+}]_{jsr}$ values ranging from 0.2 to 1.8 mM (see 0). The presence of $[Ca^{2+}]_{jsr}$-dependent regulation increased fidelity at high $[Ca^{2+}]_{jsr}$ due to enhanced $[Ca^{2+}]_{ss}$ sensitivity, which increased the likelihood that a single open RyR triggered nearby channels (Figure 2.3*A*). The frequency of Ca^{2+} sparks, which is proportional to spark fidelity, was therefore also elevated for the same reason but additionally because of a higher spontaneous opening rate at resting $[Ca^{2+}]_{ss}$ (Figure 2.3*B*). Average Ca^{2+} released per Ca^{2+} spark was slightly lower in the presence of $[Ca^{2+}]_{jsr}$-dependent regulation (Figure 2.3*C*). This is because the RyR gating model exhibits a small decrease in $[Ca^{2+}]_{ss}$ sensitivity upon JSR depletion, thus accelerating spark termination and decreasing total Ca^{2+} release. However, the combination of enhanced spark fidelity and the increased rate of individual RyR openings resulted in an exponential increase in Ca^{2+} spark frequency under Ca^{2+} overload, despite the purely linear relationship observed in the absence of $[Ca^{2+}]_{jsr}$-dependent regulation (Figure 2.3*D*). Therefore, the exponential rise in spark rate and leak rate at elevated $[Ca^{2+}]_{jsr}$ cannot be accounted for solely by the greater driving force for Ca^{2+} release flux and higher SR load, but it can be explained by RyR sensitization by $[Ca^{2+}]_{jsr}$-dependent regulation.

Figure 2.3*E* shows that there was a small effect on the fraction of leak attributed to non-spark events, with greater invisible leak at lower $[Ca^{2+}]_{jsr}$ in the presence of $[Ca^{2+}]_{jsr}$-dependent regulation. This is due to the fact that $[Ca^{2+}]_{jsr}$-dependent regulation decreases $[Ca^{2+}]_{ss}$ sensitivity at low values of $[Ca^{2+}]_{jsr}$ and therefore also lowers spark fidelity. Interestingly, we find that invisible leak is maximal at 1 mM $[Ca^{2+}]_{jsr}$ (data not shown). The decrease in invisible leak under SR overload is explained by a decline in the mean open time for non-spark RyR openings (1.90 ms at 1 mM vs. 0.64 ms at 1.8 mM). This occurs because a larger flux through the RyR occurs at higher $[Ca^{2+}]_{jsr}$, causing other RyRs to be triggered earlier. It is then more likely that even short openings would initiate Ca^{2+} sparks, decreasing the average Ca^{2+} release of non-spark events. Finally, Figure 2.3*F* shows small differences in ECC gain at a 0 mV test potential between models with and without $[Ca^{2+}]_{jsr}$-dependent regulation at varying $[Ca^{2+}]_{jsr}$, reflecting differences in RyR sensitivity to trigger Ca^{2+}.

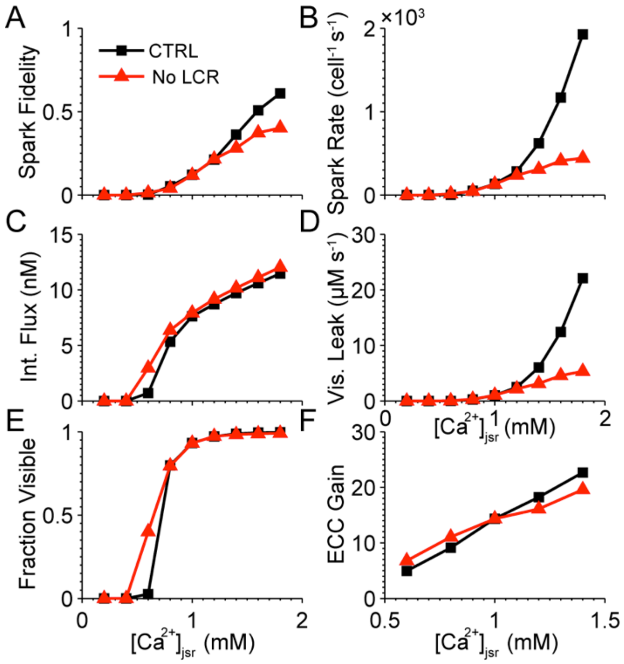

Figure 2.3 Effects of SR load on SR Ca^{2+} leak and ECC gain.

Results are plotted for two versions of the model with (*black*) and without luminal [Ca^{2+}]$_{jsr}$-dependent regulation (*red*). (A) Dependence of spark fidelity, the probability of a spark occurring given that one RyR has opened. (B) Whole-cell spark rate, estimated assuming 1.25×10^{6} RyRs per cell. (C) Mean total Ca^{2+} release per spark. (D) Visible leak released through sparks only. (E) The fraction of total RyR mediated leak attributed to invisible (non-spark) leak. (F) Peak-to-peak ECC gain for the 200 ms voltage clamp protocol to 0 mV. An example dataset for Ca^{2+} spark fidelity and leak estimates is available at: http://cvrg.galaxycloud.org/u/mwalker/h/fidelity-leak, and for ECC gain at: http://cvrg.galaxycloud.org/u/mwalker/h/ecc-gain.

2.2.4 Subspace Geometry

Ultrastructural remodeling of the subspace has been implicated in diseases such as HF (38, 39, 79) and CPVT (80, 81). We investigated how changes in subspace geometry influence CRU function. We first altered the distance between the TT and JSR membranes. Ca^{2+} spark fidelity (Figure 2.4*A*), rate (Figure 2.4*B*), and leak (Figure 2.4*C*) decreased steeply as the TT-JSR separation increased beyond the nominal width of 15 nm. This separation reduced the initial rise of $[Ca^{2+}]_{ss}$ during CICR due to the increase in subspace volume. The resulting drop in spark fidelity led to fewer sparks and less leak. The ECC gain at 0 mV also declined in a similar manner, dropping sharply from 16.8 at 12 nm to 2.4 at 30 nm (Figure 2.4*D*). This is not surprising given the effects of subspace width on fidelity, since LCCs also initiate release through CICR. Ca^{2+} sparks, Ca^{2+} spark-based leak, and ECC function were nearly abolished at subspace widths greater than 60 nm, with the exception of invisible leak, which was nearly constant over all distances.

We also investigated the effects of resizing the JSR membrane diameter (as depicted in Figure 2.1*B*) over a range of 217×217 nm^2 to 465×465 nm^2. We observed higher spark fidelity for JSRs of larger diameter (Figure 2.5*A*), which introduced resistance to diffusion of Ca^{2+} out of the subspace. Larger JSRs also exhibited greater spark-based leak and decreased invisible leak (Figure 2.5*B*). The enhanced spark-based leak was due to the higher spark rate and larger JSR volume, which provides more releasable Ca^{2+} per spark. The effect on invisible leak was smaller in absolute terms, dropping from 0.090 $\mu M\ s^{-1}$ at 217×217 nm^2 to 0.082 $\mu M\ s^{-1}$ at 403×403 nm^2 but then to 0.051 $\mu M\ s^{-1}$ at 465×465 nm^2. Smaller JSRs are more likely to leak invisible Ca^{2+} because of their lower fidelity. These results suggest that remodeling of the JSR, as observed in diseased hearts, may alter SR Ca^{2+} leak and the effectiveness of CICR and extends previous observations (41).

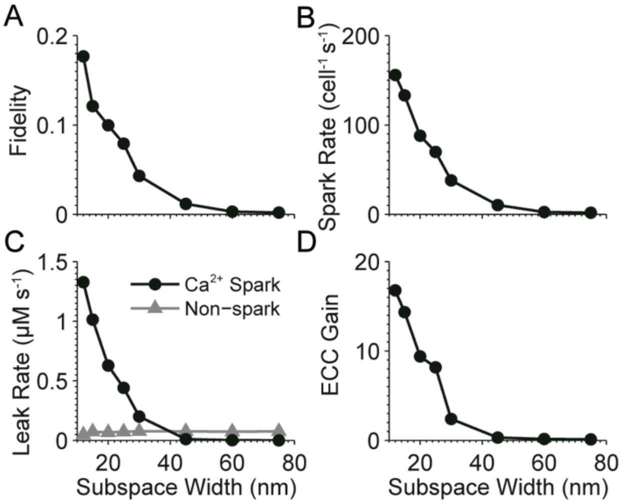

Figure 2.4 Effects of increasing the distance between TT and JSR membranes. Effects on (A) Ca^{2+} spark fidelity (B) spark rate, (C) spark (*circles*) and non-spark (*triangles*) based SR Ca^{2+} leak, and (D) ECC gain at 0 mV clamp potential. Spark-based leak and ECC gain were abolished for widths over 40 nm due to the increase in subspace volume, while invisible leak remained nearly constant.

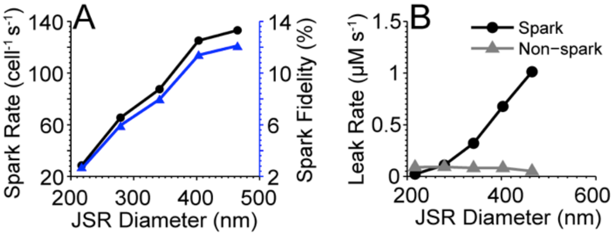

Figure 2.5 Effects of JSR diameter on SR Ca^{2+} leak.

(A) Spark fidelity (*triangles*) and rate (*circles*). (B) Spark and non-spark based SR Ca^{2+} leak. Data points collected for JSR membrane areas of 217×217, 279×279, 341×341, 403×403, and 465×465 nm^2.

2.2.5 RyR Cluster Structure

Superresolution imaging techniques have revealed the diversity and complexity of channel arrangements of peripheral RyR clusters (35). We explored how the geometry of the RyR cluster may be related to spark fidelity. Images of peripheral RyR clusters were acquired using superresolution STED microscopy of RyR immunolabelings in isolated adult mouse myocytes (C57Bl6) (41, 82). Imaging protocols were adjusted to sample RyR immunofluorescent signals at a lateral imaging resolution less than 70 nm and produced variable and complex cluster shapes. These images were then used to extract RyR cluster geometries and infer the arrangement of RyRs in each cluster. For this purpose, high signal levels equal to and above the 95th percentile brightness were interpreted to represent a closed lattice of RyR channels (83). We incorporated a collection of 15 RyR cluster arrangements that represented the diversity of cluster geometries into the model and estimated the fidelity of each RyR using the protocol from Figure 2.3*A*. Figure 2.6 illustrates the RyR cluster arrangements, where each RyR is colored according to its spark fidelity. Larger and denser clusters exhibited higher spark fidelity. For example, cluster (*i*) with 4 RyRs had a 1.2% average fidelity, while cluster (*xv*) with 91 RyRs had an 11.1% average fidelity. Evidently, there were also spatial gradients in fidelity, particularly across the larger clusters. RyRs located on the boundary of a cluster were less likely to initiate sparks, while those near the epicenter had a high chance of triggering sparks because they had more neighboring RyRs.

We also explored the spark fidelity of two artificial cluster types: square arrays and randomly generated clusters in which cluster lattice spaces contained a RyR with 50% probability. The number of RyRs in a cluster was a robust predictor of spark fidelity for the STED-based clusters and square arrays (data not shown). For these two cluster types, larger clusters exhibited higher spark fidelity. In a cell-wide population of release sites, clusters with more than 30 RyRs contributed to 92% of spark-based leak. However, the number of RyRs was not a robust predictor of spark fidelity for the randomly generated clusters. RyRs with zero, one, or two adjacent RyRs were common in the random clusters, but they contributed little to spark fidelity. Therefore, clusters with the same number of RyRs exhibited different spark fidelity because of heterogeneity in cluster structure.

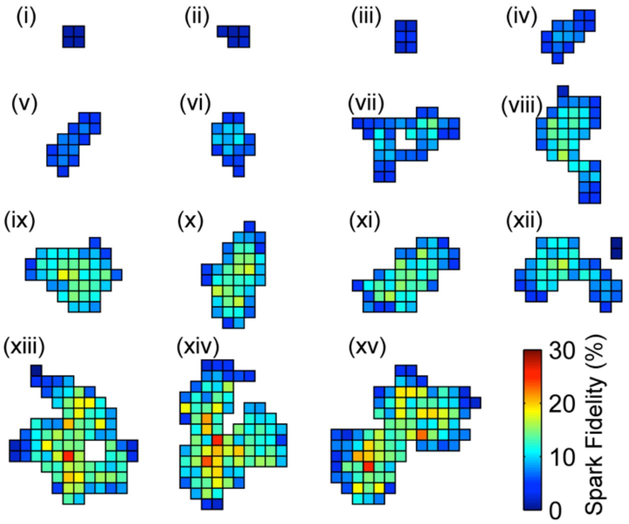

Figure 2.6 Spark fidelity of RyR cluster geometries inferred from STED nanoscopy images.

Superresolution imaging of adult rat cardiomyocyte RyR clusters at < 70 nm lateral resolution resolved highly variable cluster shapes and sizes that were translated into a lattice of pore positions. Heat maps depict the RyR cluster geometries, with the TT axis in the vertical direction. Each grid square represents a single RyR and is colored by the probability that it will trigger a spark. At least 10,000 simulations were performed for each cluster.

2.2.6 Spectral Analysis of RyR Cluster Structure

To understand why clusters with the same number of RyRs exhibit different fidelity requires consideration of the channel arrangement. A natural approach is to use a graph-based analysis in which adjacent RyRs, represented by nodes, are connected by edges.

We computed the maximum eigenvalue λ_{max} of each cluster's adjacency matrix for square arrays, STED-based clusters, and the randomly generated clusters and found a remarkably strong correlation with spark fidelity (Spearman's rank correlation ρ = 0.9055). Figure 2.7*A* shows each cluster's λ_{max} value plotted against its spark fidelity for the nominal set of model parameters. The range of λ_{max} values was 1.8 - 3.92, near the theoretical bounds of 1 - 4. STED-based clusters had a wide range of λ_{max} values (2.0 - 3.69) due to their varying sizes and degrees of compactness. Densely packed square arrays had mostly higher values (2.83 - 3.92). The randomly generated clusters fell in a lower range (1.80 - 3.23) due to their fragmented structure. It can be shown that $\langle d \rangle < \lambda_{\max} < d_{\max}$, where $\langle d \rangle$ and d_{max} are the average and maximum degrees of the graph, respectively (69). The fidelity of the clusters from Figure 2.7*A* was also significantly correlated with $\langle d \rangle$ (r = 0.8730) (data not shown). The slightly lower correlation coefficient may be attributed to the fact that λ_{max} takes into account the full structure of the RyR network.

We then tested how an increase in RyR Ca^{2+} sensitivity would alter the relationship between spark fidelity and λ_{max} because of its relevance to RyR hypersensitivity in CPVT (17, 84). Figure 2.7*B* shows the fidelity of the STED-based and square clusters when the RyR EC_{50} was decreased to from 55 to 25 μM by increasing the mean open time (τ_O) to 10 ms or increasing the opening rate constant. The strong correlation between λ_{max} and fidelity still held for this set of parameters, with $r = 0.9266$ and 0.8169 for increasing τ_O and the opening rate, respectively. Increasing τ_O elevated fidelity to a range of 0.45 – 0.72, which was greater than the range 0.31 – 0.50 resulting from increased opening rate. Note that the changes in model parameters were approximately five-fold in both cases, suggesting that Ca^{2+} spark fidelity is more sensitive to changes in τ_O. These results show how an increase in RyR sensitivity resulting from CPVT-linked mutations causes dramatically increased Ca^{2+} spark fidelity.

In all cases, λ_{max} was a consistent predictor of spark fidelity for a given set of physical parameters. We therefore conclude that the precise arrangement of RyRs in the subspace has a significant impact on the spark initiation process and that the fidelity of the RyR cluster can be reliably predicted from λ_{max}, which only requires knowledge of the RyR cluster structure.

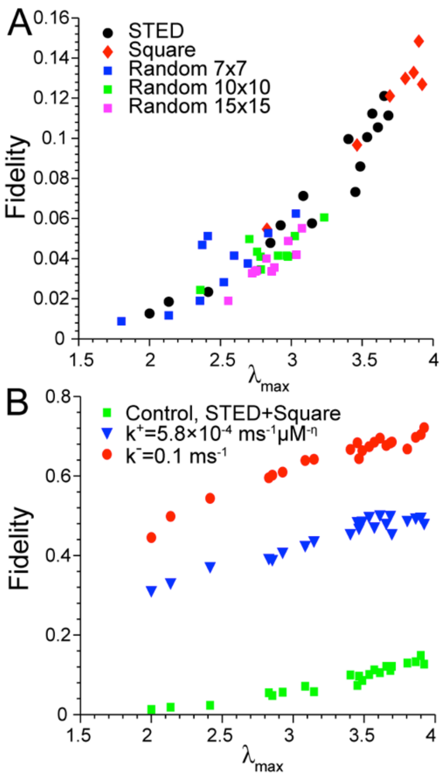

Figure 2.7 Correlation between maximum eigenvalue λ_{max} of the RyR cluster adjacency matrix and spark fidelity.

(A) Results for clusters inferred from STED images (*circles*), square arrays of RyRs (*diamonds*) and random clusters (*squares*, 7×7 in *blue*; 10×10 *green*; 15×15 *magenta*). Random clusters were generated by randomly filling each RyR lattice space with 50% probability. (B) Results for STED-based and square clusters where RyR EC_{50} was lowered from 55 to 25 μM by increasing the RyR opening rate constant k^+ from 1.10×10^{-3} to 5.80×10^{-3} $ms^{-1}\mu m^{-\eta}$ (*triangles*) or increasing τ_O to 10 ms (*circles*). The data from panel (A) for STED and square clusters are replotted for comparison (*squares*).

2.3 Discussion

Here we have presented a novel three-dimensional model of the cardiac CRU to investigate mechanisms of Ca^{2+} release. The model is based on previous work, which demonstrated that RyR-mediated leak through Ca^{2+} sparks and non-spark "Ca^{2+} quarks" is sufficient to achieve SERCA pump-leak balance in resting cells (12). The present work is the first to quantitatively capture these dynamics and exhibit a realistic ECC gain in a superresolution spatial framework that is not limited by the assumptions of a compartmental model, such as the uniformity of $[Ca^{2+}]_{ss}$ within the subspace or simplified cytosolic transport fluxes. The model has enabled us to explore how perturbations of subspace geometry and RyR cluster arrangements, like those that may occur under normal physiological conditions and in various diseased states, affect Ca^{2+} release. It also provides a framework for exploring nanoscopic Ca^{2+} signaling and can be used to investigate a plethora of topics such as the roles of Ca^{2+} load, RyR gating properties, $[Ca^{2+}]_{ss}$ and $[Ca^{2+}]_{jsr}$ sensitivity, and CRU geometry in Ca^{2+} release.

2.3.1 RyR Cluster Spectral Properties

A significant finding of this work is that the maximum eigenvalue of the RyR cluster adjacency matrix is a reliable predictor of Ca^{2+} spark fidelity. Spectral graph theory is a mature field that has been used in a variety of applications, such as the study of Internet networks (85), spread of social contagion (86), protein side chain cluster detection (87), biological networks (88), phylogeny inference (89), EEG analysis (90), and infectious disease models (91). These studies leverage the information contained in graph spectra to characterize network structure and develop novel metrics for predicting functional system properties.

Similarly, we have discovered an important role for λ_{max} in predicting an important functional property of a complex system. The correlation with spark fidelity is remarkable given the complexity and non-linearity of the model. Note that this enables one to compare fidelity across clusters for a given physiological state, and it only requires knowledge of the RyR cluster structure. We believe that this is an elegant theoretical tool that can be used for functional comparison of different cluster structures in experimental studies.

2.3.2 $[Ca^{2+}]_{jsr}$-dependent Regulation

Termination of Ca^{2+} release is essential to stable cell function. However, it remains unclear exactly how a Ca^{2+} spark terminates given the regenerative nature of CICR. Several potential mechanisms have been proposed, including $[Ca^{2+}]_{ss}$- or use-dependent RyR inactivation (92) and $[Ca^{2+}]_{jsr}$-dependent regulation of RyRs (19). Our model predicts that deactivation of the RyR caused by $[Ca^{2+}]_{jsr}$-dependent regulation is not necessary for Ca^{2+} spark termination. Note that this result may be dependent on the refill rate of the JSR, as faster rates can prevent sufficient JSR depletion and thus Ca^{2+} spark termination as well by this mechanism (data not shown) (93, 94). A more detailed model that incorporates diffusion of Ca^{2+} in the network SR may be able to address this issue more carefully. Similarly, we did not include RyR-RyR interactions (27, 28), since Ca^{2+} spark termination did not require it. Nevertheless, there is reasonable biological evidence that support such interactions. When features that require such interactions in the generation and/or termination of Ca^{2+} sparks are shown experimentally, they can be used to constrain and inform Ca^{2+} spark features.

We have also shown that $[Ca^{2+}]_{jsr}$-dependent regulation can explain the exponential shape of the SR leak-load relationship (9, 77) by 1) enhancing RyR sensitivity to the local rise in $[Ca^{2+}]_{ss}$ during a Ca^{2+} quark and 2) increasing the spontaneous RyR opening rate. It is also possible that Ca^{2+}-activated regulators, such as CaMKII (25, 26), RyR mutations (84), or mutations in RyR-linked proteins (95) may affect the relationship between SR load and spark frequency in a similar manner or that propagation of release between adjacent sites could enhance leak under overload (96). Nevertheless, the model predicts that the leak-load relationship cannot be adequately captured in the absence of these mechanisms.

2.3.3 Physiological and Pathophysiological Significance

We have shown how an increase in spark fidelity leads to higher Ca^{2+} spark frequency and Ca^{2+} spark-based leak. Ca^{2+} spark frequency is an important property that controls cellular and SR Ca^{2+} load by providing a pathway for Ca^{2+} to leak from the SR during diastole. Diastolic spark-based leak leads to extrusion of Ca^{2+} from the cell through the sarcolemmal Na^{+}/Ca^{2+} exchanger and also delicately balances SR refilling via the SERCA pump (12, 97). Under conditions with enhanced SR Ca^{2+} leak, these pathways contribute to reduced SR Ca^{2+} load and impaired systolic function.

CPVT is an inherited genetic disorder that often leads to syncope and sudden cardiac death. The disease has been linked to mutations in the RyR (*RYR*) and calsequestrin (*CASQ2*) genes (98). Chen et al. (17) recently showed that a *R33Q-CASQ2* knock-in mice exhibit CPVT-like symptoms and then showed through single-channel studies that this mutation causes an increase in RyR τ_O to ~10 ms. They attributed this increase to a loss of calsequestrin-dependent regulation of the RyR. Jiang et al. (84)

studied a CPVT-linked RYR mutation that resulted in decreased mean closed time of the channel.

We have shown that these mutations result in dramatically higher spark fidelity (compare Figure 2.7 *A* and *B*). The increased sensitivity to $[Ca^{2+}]_{ss}$ directly elevated leak, as did the higher Ca^{2+} spark rate that it caused, and both would contribute to the reduction in SR load and spontaneous cell-wide release (i.e. Ca^{2+} sparks and Ca^{2+} waves) observed in experimental models of CPVT (99-101). This model and these data suggest that CICR underlies these changes in Ca^{2+} sparks and waves and not store overload-induced Ca^{2+} release (SOICR) (102).

Using the *R33Q-CASQ2* knock-in model, Liu et al. (80) and Denegri et al. (81) observed extensive ultrastructural remodeling of the CRU, resulting in JSR fragmentation, reduced subspace areas, and smaller RyR clusters. Our results are in agreement with a recent compartmental model by Lee et al. (33), who showed that subspace volume and efflux rate critically influence spark fidelity. Interestingly, our data suggest that this could be a compensatory mechanism that helps reduce the enhanced fidelity, spark frequency, and SR Ca^{2+} leak caused by the increase in τ_O.

Chronic HF in cardiac myocytes is characterized by diminished excitation-contraction coupling and slowed contraction (9, 103), which are in part due to a reduction in SR Ca^{2+} load (41, 104). It has been shown that RyR-mediated leak alone is sufficient to cause the decrease in SR Ca^{2+} load (9). This can be attributed to a variety of posttranslational modifications to the RyR, including PKA-dependent phosphorylation (24), CaMKII-dependent phosphorylation (105), and redox modifications (106). The model shows how the spark rate rises quickly for sensitive channels, suggesting that minor increases in RyR $[Ca^{2+}]_{ss}$ sensitivity could significantly enhance SR Ca^{2+} leak in HF.

Structural changes to the CRU may be caused by a down-regulation of the protein junctophilin-2 (JP2) in HF (38, 39, 79). Wu et al. (39) observed a reduction in the length of the JSR and subspace in both failing rat myocytes and a JP2 knockdown model. This, in part, led to reduced $[Ca^{2+}]_i$ transients and desynchronized release. The present work has confirmed that the CICR process is sensitive to the diameter of the JSR, which acts as a barrier to Ca^{2+} efflux from the subspace. Shortening the JSR reduces spark fidelity (see Figure 2.5*A*) and thus the ability of trigger Ca^{2+} from the LCCs to efficiently activate the RyRs. In addition, van Oort et al. (79) demonstrated experimentally that JP2 knockdown resulted in an increase in the variability of subspace width. This is consistent with the model prediction that ECC gain is sensitive to the distance between the JSR and TT (see Figure 2.4*D*), implying that subspace width variability would also contribute to nonsynchronous release during ECC.

JSRs become separated from the TT during chronic HF, resulting in “orphaned” RyR clusters that are uncoupled from the LCCs (107). Again, the model predicts that the separation of the JSR and TT membranes strongly decreases spark frequency and ECC gain due to the increase in subspace volume. This corroborates the findings of Gaur and Rudy (32), who demonstrated that increasing subspace volume causes reduced ECC gain. We conclude here that orphaned RyR clusters contribute less to spark-based leak and Ca^{2+} release during ECC, but they may mediate invisible leak.

The heterogeneity of spark fidelity among release sites may have implications for the formation of Ca^{2+} waves. Modeling studies have suggested that conditions that enable one Ca^{2+} spark to trigger another are needed to initiate a Ca^{2+} wave (108). While it is unclear exactly how this occurs in every instance, conditions that favor regenerative Ca^{2+} sparks among local CRUs leads to both the generation of "macrosparks" and Ca^{2+} waves (42, 109). Therefore, RyR clusters with greater spark fidelity may be more arrhythmogenic because they have a higher propensity for exhibiting spontaneous release and are more likely to be influenced by the local elevation of $[Ca^{2+}]_{ss}$ produced by a nearby Ca^{2+} spark.

The model also provides insights into nanoscopic Ca^{2+} signaling during release. A small JSR results in a spherical 1 μM $[Ca^{2+}]_i$ isosurface, while a larger JSR causes lower $[Ca^{2+}]_i$ on its back face. Furthermore, peak $[Ca^{2+}]_i$ just outside the subspace ranged from ~1 – 12 μM depending on the relative position of the JSR. Additional barriers to diffusion not incorporated here, such as a mitochondrion abutting the back face of the JSR, could result in even higher local $[Ca^{2+}]_i$. These results may have implications for local Ca^{2+} sensing by mitochondria (110), CaMKII signaling (111), and Na^+/Ca^{2+} exchanger activity (112, 113). Future work incorporating these components could advance our understanding of their individual contributions to cell function under normal and pathological conditions.

2.4 Conclusion

To study the roles of RyR gating properties, spark fidelity, and CRU anatomy on CICR, we developed a three-dimensional, biophysically detailed model of the CRU. The model quantitatively reproduced important physiological parameters, such as Ca^{2+} spark kinetics and morphology, Ca^{2+} spark frequency, and SR Ca^{2+} leak rate across a wide range of conditions and CRU geometries. The model also produced realistic ECC gain, a measure of efficiency of the ECC process and healthy cellular function. We compared versions of the model with and without $[Ca^{2+}]_{jsr}$-dependent activation of the RyR and showed how it could explain the experimentally observed SR leak-load relationship. Perturbations to subspace geometry influenced local $[Ca^{2+}]_{ss}$ signaling in the CRU nanodomain as well as the CICR process during a Ca^{2+} spark. We also incorporated RyR cluster geometries informed by stimulated emission depletion (STED) (35) imaging and demonstrated how the precise arrangement of RyRs can impact CRU function. We found that Ca^{2+} spark fidelity was influenced by the size and compactness of the cluster structure. Based on these results, we showed that by representing the RyR cluster as a network, the maximum eigenvalue of its adjacency matrix is strongly correlated with fidelity. This model provides a robust, unifying framework for studying the complex Ca^{2+} dynamics of CRUs under a wide range of conditions.

Chapter 3 RyR Contact Network Model

3.1 Model Description

We developed a theoretical framework for understanding the relationship between Ca^{2+} spark fidelity and the dominant eigenvalue of the RyR cluster's adjacency matrix observed in the 3D Superresolution Ca^{2+} Spark (SRS) model. We employ the theory of contact networks (CNs), which are widely used to study the spread of disease due to contact between infected and susceptible individuals (91).

In this section, we present a stochastic CN model of the Ca^{2+} spark initiation process, in which interactions arise instead from Ca^{2+}-dependent coupling due to local influx and diffusion of Ca^{2+}. For simplicity, we assume that the local Ca^{2+} concentration gradient near an open RyR declines rapidly enough in space such that only adjacent RyRs interact (62, 76, 114). Each channel transitions stochastically between open and closed states (Figure 3.1*A*). If an RyR channel i has $Y_i(t)$ neighboring RyR channels that are open, its opening rate is $\beta Y_i(t)$, where β is a constant parameter. Therefore β is the RyR opening rate when one nearest neighbor RyR is open. Note that in the SRS model, the RyR opening rate when all neighbors are closed is very small ($\sim 9\times10^{-7}$ ms^{-1}). Therefore we have taken this rate to be zero in this formulation. The value of β is varied in our analyses. The RyR closing rate, δ, is assumed to be a constant 0.5 ms^{-1}. Derivation of the model and parameters are given in Chapter 6 Appendix B.

The CN model is able to capture RyR gating dynamics during the initiation phase of Ca^{2+} sparks. We used the Stochastic Simulation Algorithm of Gillespie (115) to simulate the stochastic CN model. Figure 3.1*B* shows traces of the number of open channels (N_O) during representative simulations of spark initiation in the SRS and CN models for a 7×7 lattice cluster. A single RyR is opened at $t = 0$, which then triggers openings of other channels. The CN model qualitatively reproduces channel gating behavior during the initiation of the spark. In the SRS model, Ca^{2+} sparks occur with greater than 95% probability if a minimum of four channels open. Therefore, we define this as the minimum number for successful spark initiation in both models. We also assume that each RyR in the cluster is equally likely to open spontaneously, and so the first open channel is chosen at random.

The advantage of developing the CN model is that we can derive analytical relationships between the dominant eigenvalue of the RyR lattice's adjacency matrix, referred to in this chapter as λ_1, and spark fidelity. In this chapter, we will refer to spark fidelity as spark probability, p_S. We show (see Chapter 6 Appendix B) that for a deterministic mean-field approximation of the model, RyR open probability decays to zero when

$$\lambda_1 < \frac{\delta}{\beta}. \tag{3.1}$$

This implies that, in the mean-field approximation, δ/β is a stability threshold for λ_1 at which RyR activity switches from decay to growth. While it was not immediately clear how this threshold related to the behavior of the full stochastic CN model, we expected that the model would exhibit constant spark probability when $\lambda_1 = \delta/\beta$. That is, for a set of cluster structures each with a different value of λ_1, the spark probability would be consistent across clusters when each cluster's opening rate was set to $\beta = \delta/\lambda_1$. Figure 2*C* shows the spark probability for a collection of 107 RyR clusters obtained using STED microscopy (see Chapter 2 for imaging methods). For each simulation, λ_1 was computed for the cluster and β was set to the threshold value δ/λ_1. The range of spark probabilities across all clusters was narrow (0.14 - 0.0078). This was also observed when using sub-threshold values $\beta = 0.5\delta/\lambda_1$ (0.029 - 0.0024) and a supra-threshold values $\beta = 2\delta/\lambda_1$ (0.28 - 0.012). Therefore spark probability is constant when β is scaled inversely with λ_1. For comparison, we also plotted spark probability when β is set to a single value across all clusters (Figure 3.1*D*). In this case, spark probability increased with λ_1 in agreement with the SRS model.

The CN model was able to accurately predict Ca^{2+} spark probability for a range of cluster geometries. We estimated the spark probabilities for a collection of 15 RyR clusters obtained using STED microscopy. The value of β was adjusted until the spark probabilities in the CN model correlated with those of the SRS model (Figure 3.1*E*). Maximal correlation was achieved for $\beta = 0.115$ ($R^2 = 0.939$), which gives the value of $\delta/\beta = 4.35$. Note that the theoretical value of λ_1 for any cluster is bounded above by the maximum number of channel neighbors (four) (116). Consequently, $\delta/\beta = 4.35 > \lambda_1$ implies that the system is always sub-threshold for any cluster structure under normal physiological conditions.

The CN model also predicts spark probability for different opening rates. To show this, we first estimated p_S in the SRS model for a 7×7 cluster with the opening rate scaled by a constant factor. We then scaled $\beta = 0.115$ by the same factor and determined p_S in the CN model. This was repeated for a range of scaling factors. Noting that the closing rates δ are the same in both models, we could directly compare p_S in the two models by plotting it as a function of δ/β, where β is the scaled value. For the SRS model, β is the value used in the corresponding CN simulation. In both models, spark probability fell rapidly as δ/β approached λ_1 from the left before decreasing gradually to the right of λ_1.

This suggests that spark probability is more sensitive to RyR gating kinetics when the opening rate is elevated. From the data in this section, we concluded that the CN model is able to accurately predict p_S over a range of opening rates and cluster geometries.

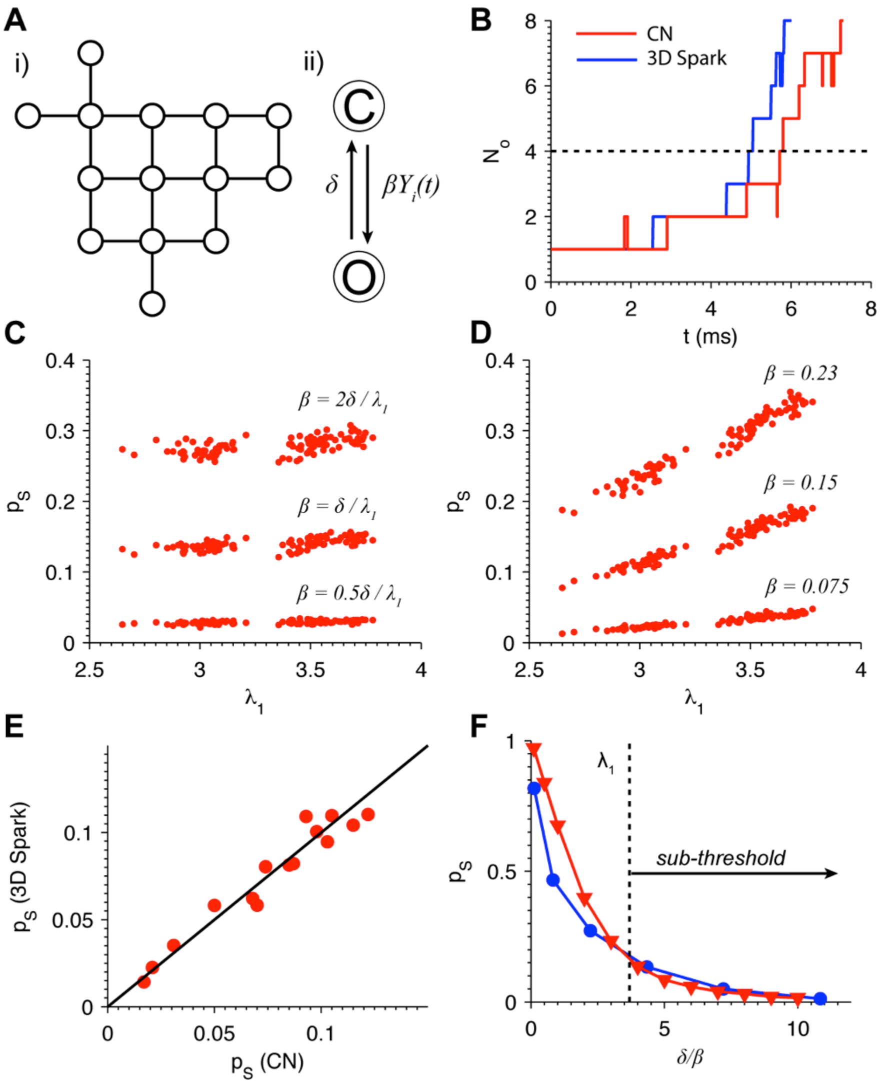

Figure 3.1 The contact network model reproduces RyR channel gating during Ca^{2+} spark initiation.

(A) Contact network model schematic showing (i) a diagram of the structure of an example RyR lattice with lines connecting adjacent channels and (ii) the Markov model representing each channel with closed (C) and open (O) states. The opening rate of each channel *i* scales with the number of open adjacent channels $Y_i(t)$. (B) Example simulations showing CN model (*red*) and SRS model (*blue*) RyR gating behavior during the spark initiation phase. Spark generation is considered successful if $N_O \geq 4$ (dashed line). (C) Spark probabilities for a collection of 107 STED-informed RyR clusters for threshold (*middle*), sub-threshold (lower), and supra-threshold (upper) values of β. (D) Spark probabilities when the value of β was set to constant values across all clusters. (E) β was adjusted to the nominal value of 0.115 ms^{-1} to maximize the correlation with spark probabilities from the SRS model for a collection of 15 representative clusters ($R^2 = 0.939$). (F) Spark probability p_S of a 7×7 lattice of RyRs as a function of δ/β in the CN (*red*) and SRS (*blue*) models (see text for details). The CN model is in the sub-threshold regime when δ/β is to the right of λ_1 (*black dotted line*).

3.2 Results

3.2.1 Ca^{2+} Diffusion in the CN Model

Cardiac Ca^{2+} release is actively regulated under normal conditions and modulated in various diseases. To study this regulation, we expanded the CN model by deriving a simple model of Ca^{2+} diffusion between RyR Ca^{2+} sources. The parameter β was estimated using this diffusion model and a model of RyR gating. All parameters were taken from the SRS model, except for the effective Ca^{2+} diffusion coefficient (d_C), which was adjusted to give $\beta = 0.115$ as determined in the previous section.

A number of signaling molecules regulate RyR channels, affecting their opening rate. This includes RyR phosphorylation by Ca^{2+} /calmodulin-dependent protein kinase II (CaMKII) and protein kinase A (PKA) (24, 117) and JSR Ca^{2+} concentration (19). Channel gating can also be altered under oxidative stress (106), and by genetic mutations (84, 95). As shown in Figure 3.2*A*, δ/β is inversely proportional to the channel opening rate constant (k^+), reflecting the increased Ca^{2+} spark frequency observed under such conditions (9, 105, 118). Note that the closing rate is δ and therefore scales δ/β linearly. Increasing the unitary channel current (i_{RyR}) resulted in a decrease in δ/β (Figure 3.2*B*). This behavior is consistent with experimental evidence (22), in which decreased i_{RyR} resulted in lowered spark frequency.

The CN model was also sensitive to parameters affecting the diffusion of Ca^{2+} ions in the release site subspace. Figure 3.2*C* shows the dependence of δ/β on d_C. As d_C increases, Ca^{2+} ions are more likely to escape the nanodomain around the open channel, thus decreasing spark probability. Uniformly increasing the distance between the open channel pore and neighboring Ca^{2+} binding site increased δ/β so as to decrease spark probability (Figure 3.2*D*).

In this section, we have used a simple diffusion model to probe the effects of perturbations to biophysical properties of the release site including the opening rate, unitary channel current, Ca^{2+} diffusion coefficient, and inter-channel spacing. The CN model suggests that minor modifications to these parameters can alter the stability of the system, thus leading to significant changes in spark probability.

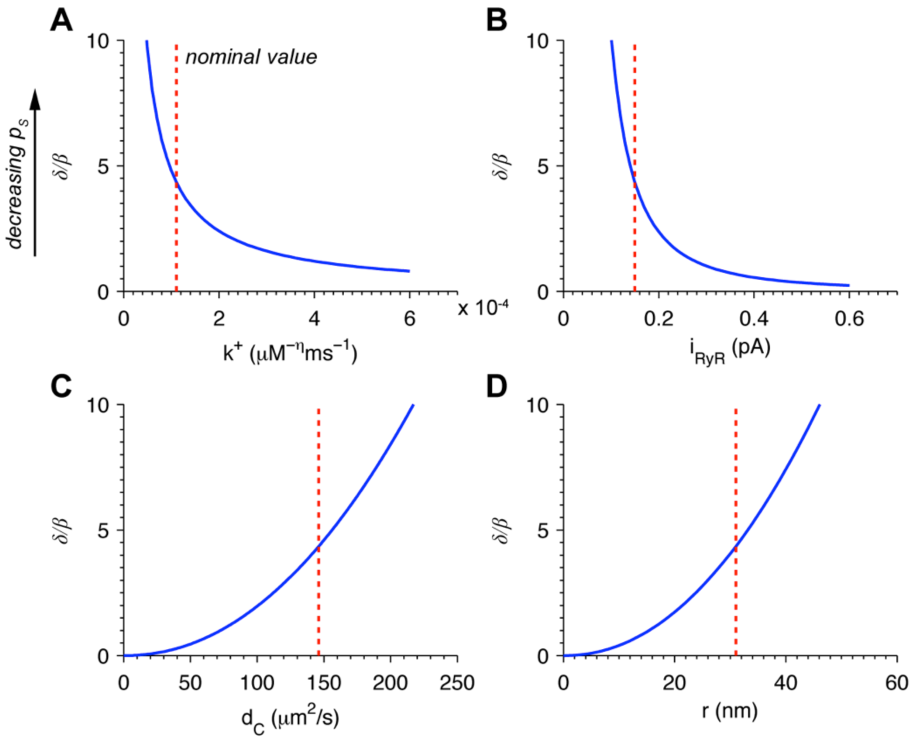

Figure 3.2 Dependence of *δ/β* on biophysical properties of the Ca^{2+} release site. Dependence on (A) the RyR opening rate constant, (B) unitary RyR current, (C) effective Ca^{2+} diffusion coefficient, and (D) distance between channel pore and neighboring Ca^{2+} binding site. Red dotted lines indicate nominal parameter values from the SRS model, except for d_C, which was adjusted to give $\beta = 0.115$ as determined in Figure 3.1*E*.

3.2.2 Linear Mean-Field CN Model

Up to this point, we have considered spark probability when each RyR is equally likely to open first. An emergent property of the SRS model was that the probability of a spark occurring varied with the choice of initiating RyR. Channels closer to the epicenter of the cluster were more likely to trigger sparks because they have more possible combinations of first, second, third, etc. neighbors along which channel openings could propagate. Likewise, channels on the periphery of the cluster were less likely to trigger sparks.

We derive a linear mean-field representation of the CN (LCN) model (see Appendix B) to quantitatively study how spark probability depends on the position of the initiating RyR. The LCN model can be used to compute the expected number of open channels as a function of time. We reasoned that a greater expected number of open channels during the spark initiation phase would imply that sparks are more likely to occur and therefore would correlate with p_S. Using the LCN model, we derived an expression for the expected number of open channels, $E[N_O]$ (see Chapter 6 Appendix B), and computed its value for a collection of 15 RyR clusters. We find that $E[N_O]$ derived in the LCN model correlated with p_S in the SRS model ($R^2 = 0.934$, Figure 3.3*A*). Note that the equation for $E[N_O]$ is time-dependent, but the results were not sensitive to our choice of the time point t ($R^2 = 0.933$ and 0.923 at $t = 4$ and 12 ms, respectively).

To further establish the relationship between $\mathrm{E}[N_O]$ and p_S, we compared $\mathrm{E}[N_O]$ to λ_1 for a broader collection of 107 clusters obtained from STED microscopy (Figure 3.3*B*). A strong correlation between these variables was present, in contrast to the number of channels in the cluster, which was not consistently correlated with $\mathrm{E}[N_O]$. Recall that these conclusions were also drawn from the data of Figure 2.7 for a smaller collection of clusters. Taken together, these data suggest that λ_1 and $\mathrm{E}[N_O]$ are both accurate predictors of p_S, while by itself the number of channels without regard to relative channel locations is not.

The LCN model was used to compute the vector whose elements are the expected number of open channels given each possible initiating RyR. We denote this vector $\mathrm{E}[\underline{n}_O]$ (see Chapter 6 Appendix B), where each element $(\mathrm{E}[\underline{n}_O])_j$ is the expected number of open channels given that channel j is opened initially. Note that our nominal value of δ/β is in the sub-threshold regime, which implies that $\mathrm{E}[N_O]$ and $\mathrm{E}[\underline{n}_O]$ both decay in the LCN model (see Chapter 6 Appendix B). Figure 3.3*C* shows how $(\mathrm{E}[\underline{n}_O])_j$ was initially 1, reflecting the first open channel, and decayed in time. This occurred at varying rates within an individual cluster, depending on the choice of initiating RyR. $(\mathrm{E}[\underline{n}_O])_j$ decayed more rapidly for channels j near the edge compared to those near the center, consistent with the lower peripheral spark probabilities estimated using the SRS model (Figure 3.3*D*). This is because channels near the edge have fewer adjacent channels to trigger, and therefore it is less likely that a second channel will open before the first closes. Furthermore, the peripheral channels tend to have fewer second, third, etc. neighbors that can potentially be activated compared to central channels.

We conclude that both the expected number of open channels in the LCN model is strongly correlated with spark probability. This fact will be used to further analyze spatial gradients in spark probability that depend on which RyR is opened initially.

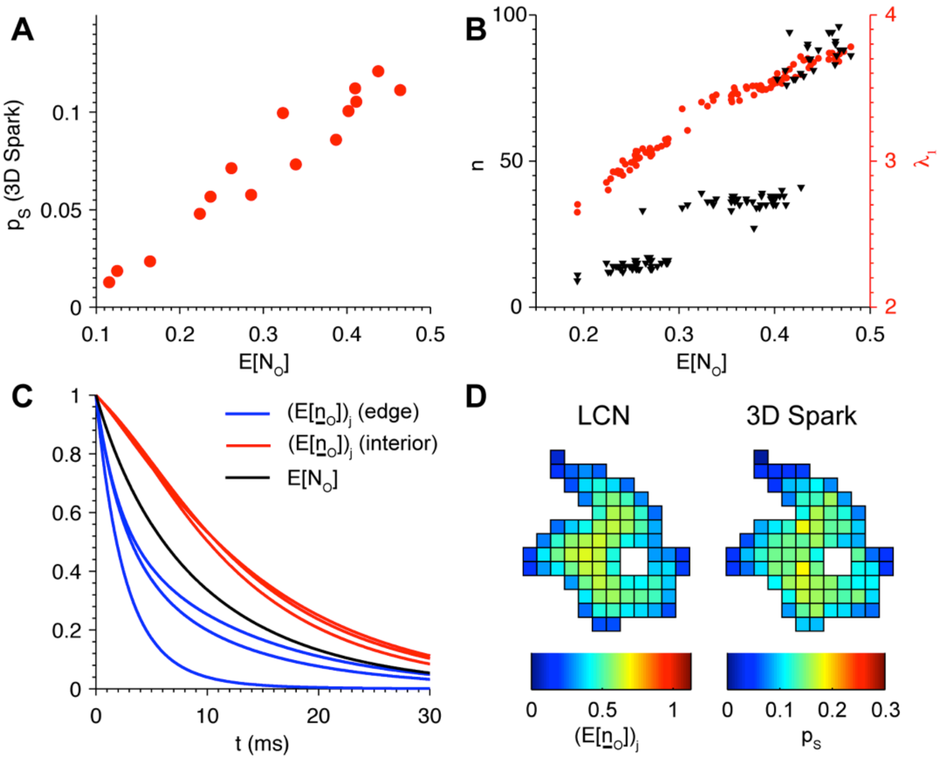

Figure 3.3 The expected number of open channels in the linearized mean-field CN (LCN) model predicts spark probability.

(A) Expected number of open channels (E[N_O]) of the LCN model at t = 8 ms strongly correlated with p_S of the SRS model ($R^2 = 0.934$). Data are shown for a collection of 15 clusters. (B) E[N_O] also correlated with λ_1 (*red*), but not with the number of channels in the cluster (*n*, black). Data points are from collection of 107 clusters. (C) Time dependence of the expected number of open channels for different initiating RyRs (E[$\underline{n}_O$]) on edge of the cluster (*blue*), in the interior (*red*), and the average (E[N_O]) for the cluster shown in the following panel. (D) Heatmaps of E[$\underline{n}_O$] (*left*) and p_S estimated using the SRS model (*right*) illustrates intra-cluster gradients in spark probability.

3.2.3 Characterization of Subdomains by the Eigenmodes

The LCN model can be decomposed into a set of independent eigenmodes by taking the similarity transform of the adjacency matrix: **A**= **VDV**^{T}, where **V** is the modal matrix whose columns are formed by a set of orthonormal eigenvectors $\{\underline{v}_1, \underline{v}_2,..., \underline{v}_n\}$ and **D** is a diagonal matrix of eigenvalues $\{\lambda_1, \lambda_2,..., \lambda_n\}$ in descending order. Note that **A** is symmetric such that $\mathbf{V}^{-1} = \mathbf{V}^T$. The i^{th} eigenmode is defined by the pair λ_i-$\underline{v}_i$, in which λ_i determines the rate of decay of the eigenmode in time and the values $(\underline{v}_i)_j$ determine the membership of channel j in the eigenmode. We derived an expression for E[$\underline{n}_O$] as a weighted sum of the eigenvectors

$$E\left[\underline{n}_O(t)\right] = \sum_{i=1}^{n} b_i(t)\underline{v}_i \,, \tag{3.2}$$

where the weights $b_i(t) = e^{(\beta\lambda_i-\delta)t}\underline{u}^T\underline{v}_i$, with $\underline{u}$ being the all-one-vector. A similar expression for E[N_O] is given by

$$E\left[N_O(t)\right] = \sum_{i=1}^{n} c_i(t)\,, \tag{3.3}$$

where $c_i(t) = (1/n)e^{(\beta\lambda_i-\delta)t}(\underline{u}^T\underline{v}_i)^2 = (1/n)b_i(t)\underline{u}^T\underline{v}_i$. Therefore E[$\underline{n}_O$] and E[$N_O$] are essentially equal to weighted sums of the eigenmodes. The derivation of these equations can be found in Chapter 6 Appendix B.

In the previous section, we presented further evidence of the relationship between λ_1 and spark probability as well as intra-cluster spatial gradients in spark probability. A natural question to then ask is: does the dominant eigenvector ($\underline{v}_1$) corresponding to λ_1 give us information about these gradients? Furthermore, how significant are other eigenmodes?

The spatial distribution of $E[\underline{n}_O]$ is shown for collection of 10 RyR clusters in Figure 3.4*A*. We further defined $c_i = c_i(\hat{t}) \Big/ \sum_{j=1}^{n} c_j(\hat{t})$ at $\hat{t}$ =8 ms, which gives the fractional contribution of the i^{th} eigenmode to $N_O(\hat{t})$. We decomposed these clusters into their eigenmodes and plotted the values of c_i corresponding to the 8 greatest eigenvalues in Figure 3.4*B*. In most cases (clusters (1)-(4), (6), (7), (9)), c_1 was the only large value, implying that the dominant eigenmode characterized the behavior of the LCN model. Clusters (5), (8), and (10), however, exhibited another significant c_i corresponding to a subdominant eigenmode.

Examining the dominant eigenmode of each cluster, we found that for clusters characterized by only the dominant eigenmode, there was a single locus of elevated membership in the dominant eigenvector corresponding to the channels j with greatest values $(E[\underline{n}_O])_j$ (Figure 3.4*C*). Furthermore, the eigenmode's spatial gradients resembled the full solution in Figure 3.4*A*. For clusters with a subdominant eigenmode (5, 8, 10), however, the dominant eigenvector did not fully characterize the spatial gradients in $E[\underline{n}_O]$. For these clusters, the subdominant eigenmode accounted for areas of high $E[\underline{n}_O]$ that were not included in the dominant eigenmode (Figure 3.4*D*). In addition, the subdominant eigenmodes were insignificant in the other clusters.

To quantitatively assess how well the dominant and subdominant eigenmodes characterize spark probability, we computed the correlation coefficients between the $E[\underline{n}_O]$ and the dominant ($k = 1$), the sum of dominant and subdominant ($k = 2$), and sum of the dominant, subdominant, and a tertiary eigenmode corresponding to the third largest c_i ($k = 3$) (Figure 3.4*E*). Clusters well described by the dominant eigenmode generally yielded high $\rho_1 > 0.84$, indicating that $\underline{v}_1$ was sufficient to characterize the spatial gradients in spark probability. For the clusters with significant subdominant eigenmodes, ρ_1 was lower (< 0.68), and the second eigenmode was required to establish a correlation. Note that inclusion of the tertiary eigenmode did not greatly improve the correlation, suggesting that the first two eigenmodes were most significant.

In this section, we characterized the intra-cluster spatial gradients in spark probability in terms of the eigenvalues and eigenvectors of the adjacency matrix. In the majority of cases, the dominant eigenmode λ_1-$\underline{v}_1$ was sufficient to approximate the gradients. Clusters (5), (8), and (10) of Figure 3.4, however, possessed secondary subdomains of channels separated from the dominant subdomain by a bottleneck (i.e. dumbbell-like morphology). These functional subdomains generally contained channels with lower spark probability than the dominant subdomain. This is consistent with Equation (3.3), which indicates that these secondary subdomains are also characterized by a decay rate $1/\lambda_s > 1/\lambda_1$ and therefore would be expected to have lower spark probability.

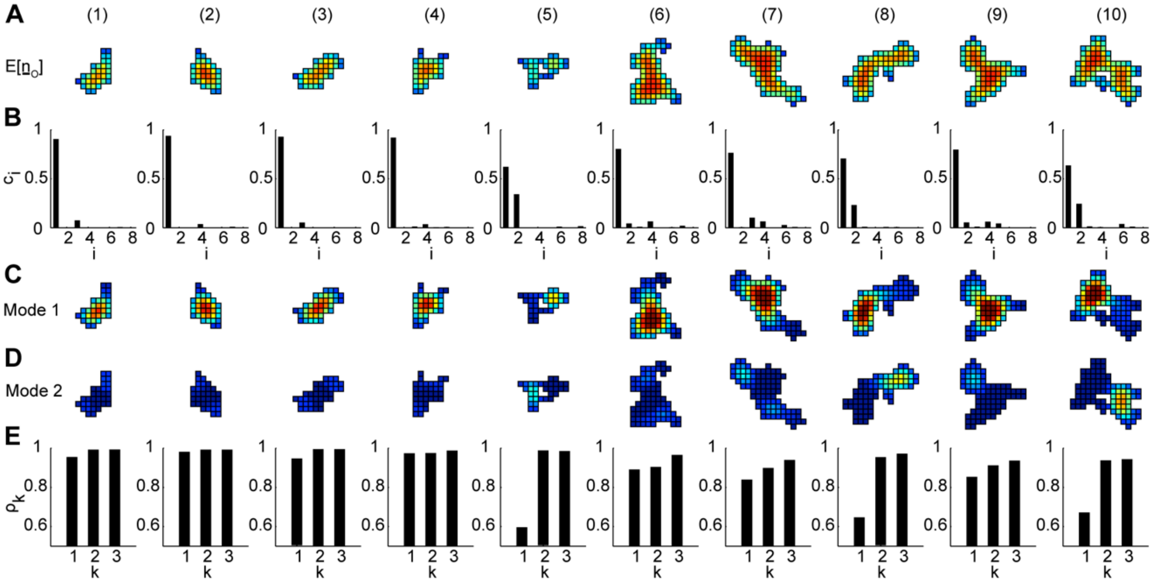

Figure 3.4 Intra-cluster spatial gradients in spark probability are characterized by one or two eigenmodes.

Data are shown for 10 clusters obtained from STED microscopy. (A) Spatial gradients in E[$\underline{n}_O$]. (B) Fractional eigenmode contributions to E[N_O] corresponding to the 10 greatest eigenvalues of the adjacency matrix. (C) Dominant eigenmode ($b_1\underline{v}_1$) corresponding to λ_1. (D) Subdominant eigenmode corresponding to the second greatest b_i. Negative values are shown as 0 for clarity. (E) Correlation coefficients between the values of E[$\underline{n}_O$] from panel (A) and the (1) dominant eigenmode, (2) sum of dominant and subdominant eigenmodes, and (3) sum of dominant, subdominant, and tertiary eigenmodes. Color scales in all panels are the same as in Figure 3.3*D*.

3.2.4 Perturbation Analysis

It is not clear how one can determine whether a cluster is characterized by a single eigenmodes or dominant-subdominant pair of eigenmodes without performing the eigendecomposition computations. For example, comparing clusters (6) and (8) in Figure 3.4, it is not immediately obvious why (8) requires both modes and (6) does not. To better understand this relationship, we progressively severed the connection between two functional subdomains at the top and bottom of cluster (6). In Figure 3.5*A*, we removed channels from this cluster proceeding left to right along the row of channels indicated by the dashed line in the baseline cluster. A subdominant eigenmode emerged as the channels were removed. The dominant eigenmode remained in the lower subdomain, while the subdominant eigenmode formed in the upper region. Note the formation of two disjoint subclusters in cluster (A4), which have eigenmodes similar to when connected by a single channel in (A3). The formation of a secondary subdomain is further demonstrated by an increase in the value of c_i for the subdominant eigenmode (Figure 3.5*B*). In this example, the subdominant eigenmode appeared after removing only one channel and gradually became more prominent with the removal of additional channels. Therefore, the formation of a subdominant eigenmode can be quite responsive to reductions in the region dividing two possible subdomains, each distinguished by different propensities for sparks.

We next investigated how sensitive spark probability is to small changes in lattice shape. Figure 3.5*C* shows a series of clusters in which only a single channel was removed from the original cluster. As expected, removing a channel along the upper edge as in cluster (C1) where spark probability is low resulted in a small change in $\lambda_1 (\delta \lambda_1)$.

Discarding a central channel as in cluster (C4) resulted in the greatest change. One may expect that removing channels with the higher spark probability would cause a greater decrease in λ_1. However, the channel removed in cluster (C2) corresponded to a greater element in E[$\underline{n}_O$] than the channel in (C3), yet the change in λ_1 was less. This is because the channel in cluster (C3) had greater membership in the dominant eigenmode. To illustrate this, we systematically removed each channel one at a time from the baseline cluster and calculated $\delta\,\lambda_1$. Figure 3.5*D* shows that there was a consistent relationship between $\delta\,\lambda_1$ and the discarded channel *j*'s corresponding element of the dominant eigenvector $(\underline{v}_1)_j$ in the original cluster but not $(\mathrm{E}[\underline{n}_O])_j$. Therefore element j of the dominant eigenvector determines the extent by which spark probability decreases when a single channel j is removed.

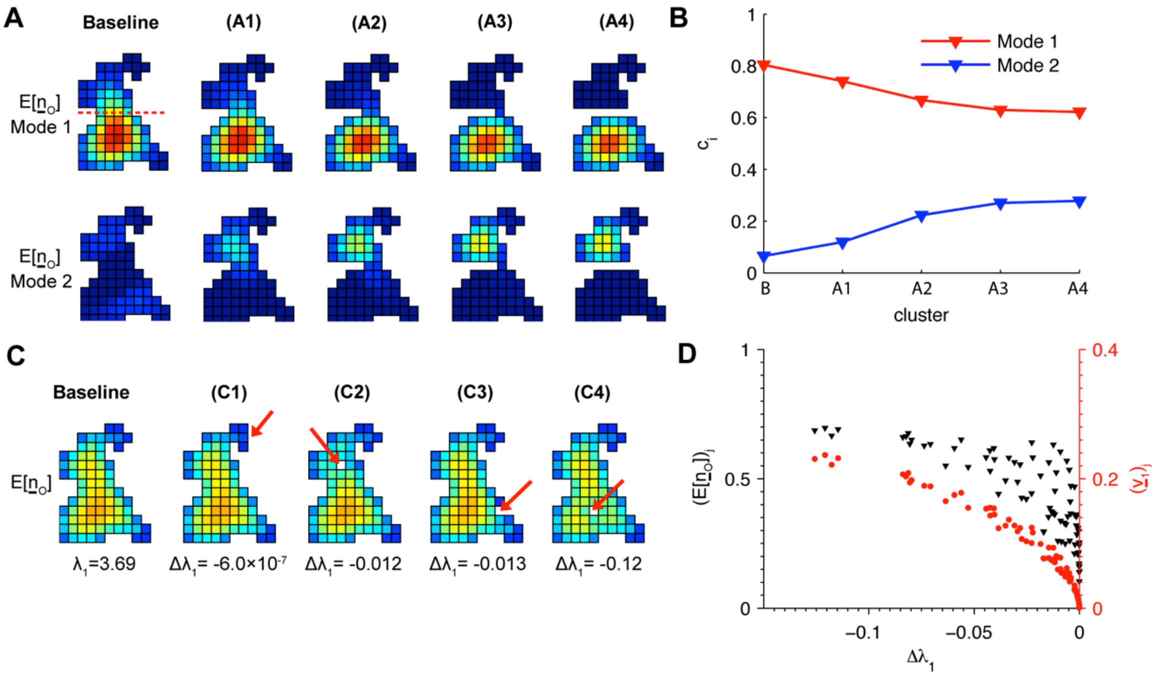

Figure 3.5 Perturbation analysis of lattice structure.

(A) Dominant (top) and subdominant (*bottom*) eigenmodes for six variations of cluster (6) in Figure 3.4. In clusters (A1)-(A4), channels are progressively removed from left to right along the row indicated by the dashed line on the baseline cluster. (B) Values of eigenmode weights c_i as the channels are removed. (C) Removal of a single channel indicated by the arrows caused varying reductions in λ_1 depending on its position. The change in λ_1 compared to the baseline cluster ($\delta\lambda_1$) is shown for each cluster (C1)-(C4). Heatmaps show E[$\underline{n}_O$] in each case. (D) Change in λ_1 when removing a single channel *j* from the baseline cluster. $(\underline{v}_1)_\mathrm{j}$ is the channel's corresponding element in the dominant eigenvector (*red*) and (E[$\underline{n}_O$])$_\mathrm{j}$ is its element in E[$\underline{n}_O$] (*blue*) in the baseline cluster. $\delta\, \lambda_1$ is again the change in λ_1 upon removing channel *j*. Heatmap color scales are the same as in Figure 3.3*D*.

3.3 Discussion

We showed in Chapter 2 that the precise structure of RyR channel clusters influences properties of Ca^{2+} release. In particular, the probability of a Ca^{2+} spark occurring when an RyR opens spontaneously depends strongly on the arrangement of the RyRs in the subspace. This has implications for Ca^{2+} cycling in the cell, as Ca^{2+} spark probability controls the frequency of Ca^{2+} sparks and the excitability of the cluster (12). An emergent property of this biophysically detailed model was that λ_1 is a strong predictor of Ca^{2+} spark probability.

Here we presented a model similar to those used to study the spread of contagion, such as in disease epidemics (119). In this model, a single RyR is opened initially, which increases the open probability of its neighbors via a local rise in Ca^{2+} concentration. After deriving a linearized mean-field formulation of the system, we showed that the open probability of the RyRs is extinguished when $\lambda_1 < \delta/\beta$. Therefore λ_1 governs a stability threshold for spark generation. In the stochastic model, spark probability was constant across all clusters when $\lambda_1 = \delta/\beta$. Therefore, if one compares any two different RyR clusters, the cluster with lower λ_1 value would need a lower δ/β ratio (i.e. greater RyR mean open time or opening rate) to achieve the same spark probability as the other cluster. This explains why λ_1 is correlated with Ca^{2+} spark probability. Cator and Van Mieghem derived a second-order CN model, with which they showed that the true threshold for the system to exhibit exponentially long transients is in fact bounded from above by λ_1 (120). Nevertheless, the first-order model presented here was sufficient to account for the relationship between λ_1 and spark probability.

It is known that the maximum eigenvalue of a graph's adjacency matrix is related to the number of walks on the graph (116). Specifically, if W_k is the number of possible walks of length k on a graph with n vertices, then $W_k \approx n \lambda_1$ ^k when k is large. Furthermore, W_k is proportional to $(\underline{u}^T\underline{v}_1)^2$ when k is large. Recall that this term also appears in the expression for c_1. It is no coincidence that W_k and $E[N_O]$ are related. Intuitively, a greater number of walks implies that there are more possible contiguous sets of RyRs along which channel openings can propagate. This is essentially the underlying relationship between λ_1 and Ca^{2+} spark probability.

An eigendecomposition of the CN model further identified RyR subdomains characterized by different spark probabilities, as observed in the SRS model. Secondary subdomains with lower spark probability were found in clusters containing two groups of channels separated by central narrow regions ~2-3 channels in width. This lends meaning to the eigenvectors of the model, which define the membership of the RyRs to each functional subdomain. Interestingly, $\underline{v}_1$ is a known measure of vertex centrality (121), which means that the proportion of all possible walks of length k beginning at vertex j is $(\underline{v}_1)_j/(\underline{u}^T\underline{v})$ when k is sufficiently large. This implies that the elements of $\underline{v}_1$ indicate the relative number of lattice walks beginning at each channel. Our results suggest that this is approximately true for clusters characterized by the dominant eigenmode, as channels with greater values of $(\underline{v}_1)_j$ had higher spark probability. Because we consider the transient behavior of channel gating during a fixed time window, the assumption that k is large (i.e. t is large) may not hold, thus explaining why a subdominant eigenmode was observed for some clusters.

Our results indicate that the system is near the threshold under normal conditions, as the ratio δ/β is close to the threshold λ_1. Therefore, small changes to β can greatly change the qualitative behavior of the system. Using a simple Ca^{2+} diffusion model, we determined that spark probability is sensitive to changes in biophysical parameters.

RyR open probability is modulated by a variety of factors including phosphorylation (24, 117), JSR Ca^{2+} concentration (19), oxidative stress (106), and genetic mutations (84, 95). Most of these increase the opening rate of the channel and cause elevated Ca^{2+} spark frequency. Our work in Chapter 2 and others (16, 76) have shown that RyR regulation by JSR Ca^{2+} concentration is not necessary for spark termination. Rather, depletion of the JSR Ca^{2+} stores causes a sufficient decrease in unitary RyR current such that the channel openings are not sustained. This mechanism is supported in the present model as well, as shown by the sharp increase in δ/β as i_{RyR} is decreased (see Figure 3.2*B*), as it would be due to reduction of the Ca^{2+} concentration gradient from inside the JSR to the subspace when RyRs open.

A recent imaging study by Asghari et al. (122) observed regulation of RyR cluster structure. The authors reported RyRs clusters in dense side-by-side lattices, as assumed in the present study, as well as checkerboard-like arrangements with greater spacing of ~37 nm compared to the baseline of 31 nm. Increasing channel spacing uniformly caused an increase in δ/β to 6.3 at 37 nm (see Figure 3.2*D*). Note that for any graph whose vertices have a maximum of m neighbors, $\lambda_1 < m$ (69). Therefore $\lambda_1 < 4$ for cluster lattices. This suggests that any cluster in the checkerboard arrangement would be unlikely to exhibit Ca^{2+} sparks in the absence of other changes. Interestingly, checkerboard spacing was observed upon channel phosphorylation or after decreasing the cytosolic Mg^{2+}

concentration, both of which increase RyR open probability (19, 24). Therefore the increase in inter-channel spacing may counteract the effects of these conditions.

We maintained focus on the relevance of cluster morphology to Ca^{2+} spark probability when a single RyR opens spontaneously. Ca^{2+} release can also be triggered following electrical excitation of the cell due to Ca^{2+} influx through apposing LCCs located on the transverse tubule. Note modeling studies suggest that coupling fidelity between LCCs and RyRs is still strong despite low spark probability (11, 12, 114). This is because although LCC mean open time is shorter (~0.5 ms), unitary LCC current is approximately the same as the RyR, there are usually several LCCs per RyR cluster (the ratio of RyRs to LCCs is 4-10 (123)), and LCC openings are synchronized upon membrane depolarization to drive local buildup of Ca^{2+}.

The study of sub-cellular structure using super-resolution techniques requires careful interpretation of the raw image data. In this study, we generated RyR cluster lattices based on fluorescence intensity using a uniform thresholding algorithm. Intensities at or above the 95th percentile were interpreted to represent the RyR positions over the entire image. To assess uncertainty in the results with respect to our choice of threshold, we analyzed a single set of STED images using both the 95th and 98th percentile thresholds. At the higher threshold, more of the fluorescence signal is filtered out and thus the clusters contain fewer RyRs. This resulted in lower values of λ_1 and decreased p_S (Figure 3.1*A*). The large differences in spark probability after using the higher threshold highlight the sensitivity of the model to the image processing methods. Nevertheless, there was still a strong correlation between p_S and λ_1 when using the higher threshold (Figure 3.1*B*). Consequently quantitative prediction of spark probability applying λ_1 requires consistent interpretation of superresolution imaging data and in addition benefits from an incremental alteration of image analysis parameters if possible.

We did not consider weaker interactions between RyRs such as those between diagonally adjacent neighbors. This results in an underestimation of the open probabilities. We also did not consider clusters with heterogeneous inter-channel spacing as observed in Asghari et al. (122). We also only considered single connected clusters containing no gaps that divide the cluster into separate subclusters. We assumed that the Ca^{2+} concentration gradient surrounding an open RyR declines sufficiently rapidly such that a negligible Ca^{2+} concentration is sensed in nearby subclusters, and therefore spark initiation occurs independently. These limitations could be overcome by using a distance matrix or diffusion model as in (28) to compute inter-RyR Ca^{2+} coupling. In addition, the LCN model is known to deviate most from the exact model near the stability threshold $\delta/\beta = \lambda_1$ (124). Note it has been shown that the solution of the mean-field CN model is an upper-bound on the true probabilities (125), and although higher-order approximations do exist (120) we chose the first-order mean-field approximation for its simplicity and analytical tractability.

The CN model may also be applied to similar biological systems. It may be adapted to study Ca^{2+} release triggered by an LCC. The spark probability would be related to the coupling fidelity between LCCs and RyRs. This model could be used to analyze the arrangement of LCCs as such experimental data become available. It may also be applied to future imaging studies to compare RyR cluster morphology to, for example, identify interspecies variability or remodeling in heart disease. For example, reduced RyR cluster sizes and fragmented JSR morphology have been observed in mouse models of CPVT (80). Inositol trisphosphate receptors (IP3Rs) located in the sarcoplasmic reticulum are known to aggregate into small clusters that exhibit similar release events known as Ca^{2+} "puffs," and recent work has implicated cluster size in release extent (126) and trigger probability (127). The present models could be used to compare IP3R cluster geometries like those reported in a recent study (128). In skeletal muscle, Ca^{2+} release is coordinated mainly by physical LCC-RyR1 and RyR1-RyR1 interactions (129). Imaging studies have observed that RyR1 clusters in slow-twitch muscle fibers were typically smaller and more fragmented than in fast-twitch muscle (34, 130). The model presented here could be used to relate these observations to known differences in the Ca^{2+} release properties of these cell types.

More generally, the model could be adapted to complement super-resolution imaging studies of a wide range of receptors that form similar supramolecular clusters in other cell types (131, 132). A general theoretical model has suggested that clusters of ligand-activated receptors behave cooperatively (133). Examples from neurons include synaptic microclusters of syntaxin 1 (134), acetylcholine receptor complexes at the neuromuscular postynapse (135), and rings of AMPA receptors found in spiral ganglion neurons (136). Another example are immunoreceptors (137), which form clusters to amplify signal initiation and transduction, perhaps by decreasing the effective dissociation constants of ligands and downstream effectors (138). Furthermore, Greenfield et al. employed super-resolution techniques to investigate the spatial organization of receptors involved in bacterial chemotaxis (139). These receptors form clusters in the cell membrane and, similar to RyRs, exhibit cooperative interactions that enhance sensitivity to low chemical signals.

This work presents a new perspective on cardiac calcium release and, more generally, highlights the relevance of subcellular variability in microdomains for the study of multi-scale biological systems.

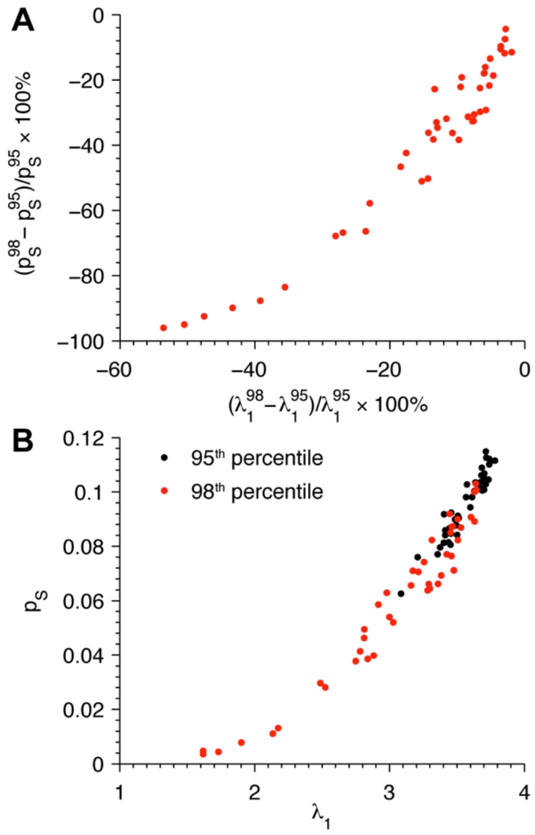

Figure 3.6 Dependence of λ_1 and Ca^{2+} spark probability on RyR cluster image interpretation.

(A) Percent changes in spark probability and λ_1 for a collection of clusters reconstructed from STED images after raising the fluorescence intensity threshold from the 95th percentile (p_S^{95}, λ_1^{95}) to the 98th percentile (p_S^{98}, λ_1^{98}). (B) Relationship between λ_1 and p_S when cluster structures are determined at the 95th (*black*) and 98th (*red*) percentiles.

3.4 Conclusion

Here we presented an analytical model of the Ca^{2+} release process and derive the relationship between λ_1 and spark probability. The model was applied to realistic RyR clusters obtained using stimulated emission depletion (STED) microscopy and recapitulated the spatial gradients in spark probability observed in the SRS model. We found through an eigendecomposition that some RyR clusters possess functional subdomains with distinct sensitivity to Ca^{2+}. This work outlines a unique approach to understanding CICR and provides a theoretical framework for comparing the physiological function of protein clusters based solely on structural information.

Chapter 4 Stochastic Tissue Model

4.1 Superresolution Modeling of Release Site Coupling

Recent super-resolution imaging experiments of RyR clusters revealed that RyR clusters can be closely spaced (<100 nm edge-to-edge) (36, 140). However, the question has been raised as to whether these clusters are contained within multiple subspaces and whether they are functionally coupled (141). Three-dimensional reconstructions of JSR and TT morphology in mouse showed that subspaces can extend along the length of the TT with varying JSR diameter (36, 37).

In light of these data, we next sought to investigate the properties of calcium release at a pair of release sites where the JSRs are tethered together by a narrow sarcoplasmic connection. We extended the SRS model to incorporate an additional release site on the same TT (Figure 4.1*A*). Figure 4.1*B* shows four configurations used in the model. Configuration (i) consists of a single elongated JSR containing two RyR clusters, and configurations (ii)-(iv) consist of two identical release sites with RyR cluster edge-to-edge spacing of 93-155 nm. At the start of each simulation, a calcium spark was initiated by holding one RyR open in the "initiating" release site for 10 ms.

For each configuration, the probability that a Ca^{2+} spark was triggered at the neighboring site is plotted in Figure 4.1*B*. For configuration (i), the probability was approximately 100% due to the high resistance to Ca^{2+} efflux out of the subspace and larger Ca^{2+} stores contained in the elongated JSR. Increasing the edge-to-edge distance to 93 nm and splitting the JSR into two separate compartments resulted in a 50% drop in spark probability, as in configuration (ii). Thus, regardless of whether the JSR formed a single compartment, RyR clusters with <100 nm edge-to-edge spacing were functionally coupled. However, increasing the separation distance by 31 nm greatly reduced the triggering probability, as in configuration (iii). These results strongly suggest that the RyR superclusters observed in recent studies are likely to be functionally coupled because subclusters sense high local elevations of [Ca^{2+}] caused by Ca^{2+} sparks at neighboring sites.

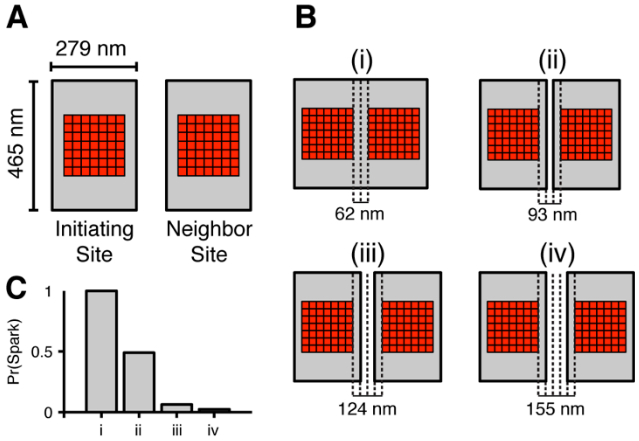

Figure 4.1 Superresolution model of two Ca^{2+} release sites.

(A) Model geometry incorporating two Ca^{2+} release sites on a single TT (not shown for clarity). (B) Release site configurations with varying edge-to-edge RyR cluster spacing. (C) Probability that a Ca^{2+} spark at the initiating site triggered a Ca^{2+} spark at the neighboring site.

4.2 Model Description

4.2.1 Ventricular Myocyte Model

We developed a 3D model of a single heart cell based on the Greenstein-Winslow canine ventricular myocyte model (59). To enable reproduction of realistic Ca^{2+} waves and DADs, the original non-spatial model was adapted to include spatial Ca^{2+} diffusion on a rectangular lattice of 25,000 Ca^{2+} release sites. The cell was divided into 25 and 20 lattice points in the two transverse directions and 50 lattice points in the longitudinal direction. Release sites were spaced 1 and 2 μm in the transverse and longitudinal directions, respectively (142). The time constant for longitudinal Ca^{2+} diffusion was twice that for the transverse direction (i.e. 2x slower) such that the model exhibited symmetric Ca^{2+} wave propagation (143).

A submembrane (SM) release site compartment was added to describe the volume under the membrane where $[Ca^{2+}]_i$ is elevated during Ca^{2+} sparks and cell-wide Ca^{2+} release (144). Detailed imaging studies of Ca^{2+} release sites have revealed that RyR clusters exhibit edge-to-edge spacing of less than 100 nm (36, 140). We showed in the previous section that neighboring sites are likely to be functionally coupled through local Ca^{2+} diffusion. Therefore Ca^{2+} diffusion between SM compartments was implemented to reflect Ca^{2+} transport across steep $[Ca^{2+}]$ gradients on the periphery of the release site during release. The SM compartment was modeled as a layer above the TT membrane (TT radius 100 nm) with thickness 80 nm that extends 1 μm along the axis of the TT. It was assumed that 50% of NCX are located in the SM compartment and the rest are in the cytosol (112, 145). Ca^{2+} in the SM is buffered by calmodulin and sarcolemmal binding sites. Ca^{2+} transport rates from the SM to the cytosol and between SM compartments were constrained to yield a realistic Ca^{2+} wave threshold (~100 - 150 μmol/L cytosol) (146) and velocity (50-100 μm/s) (42) in the baseline model.

Each site at coordinate (*i*,*j*,*k*) contains its own set of ordinary differential equations to describe local Ca^{2+} transport (Figure 4.2*A*). The Ca^{2+} concentration ($[Ca^{2+}]$) is assumed to be uniform within the local JSR ($[Ca^{2+}]_{jsr\ ,i,j,k}$), dyadic subspace ($[Ca^{2+}]_{ss\ ,i,j,k}$), and SM space ($[Ca^{2+}]_{sm,i,j,k}$) compartments. Spatial Ca^{2+} diffusion is modeled as transport between SM compartments of adjacent release sites in the 3D lattice (Figure 4.2*B*). Model equations and parameters are given in Appendix C.

It was assumed that the lattice of local JSR, SS, and SM Ca^{2+} compartments could adequately describe spatial Ca^{2+} dynamics in the cell. Therefore, bulk compartments were used to represent average cytosolic $[Ca^{2+}]$ ($[Ca^{2+}]_i$) and network SR $[Ca^{2+}]$ ($[Ca^{2+}]_{nsr}$). This assumption eliminated two Ca^{2+} diffusion parameters and provided a three-fold reduction in the number of Ca^{2+} diffusion terms.

Each release site also contains a set of 48 RyRs and 8 LCCs that gate stochastically according to Markov chain models. The LCC model is essentially as described in the Greenstein-Winslow model (59), with adjustments made to the rate of Ca^{2+}-dependent inactivation in order to reproduce the inactivation kinetics of the original model (see Appendix C). RyR gating is described by the minimal two-state Markov model used in the SRS model. Briefly, mean open time of each channel is 2 ms, and the opening rate is given by

$$r_O = \phi k^+ \left([Ca^{2+}]_{SS,i,j,k}\right)^{\eta} \tag{4.1}$$

where $k^+ = 1.107 \times 10^{-4}\ \mathrm{ms}^{-1}\ \mu\mathrm{M}^{-\eta}$ is the opening rate constant, $\eta = 2.1$ is the Ca^{2+} Hill coefficient, and ϕ is a $[Ca]_{JSR,i,j,k}$-dependent regulation term given by

$$\phi_O = 0.8025 + \left(\frac{[Ca^{2+}]_{JSR,i,j,k}}{1.5\text{mM}} \right)^4 . \tag{4.2}$$

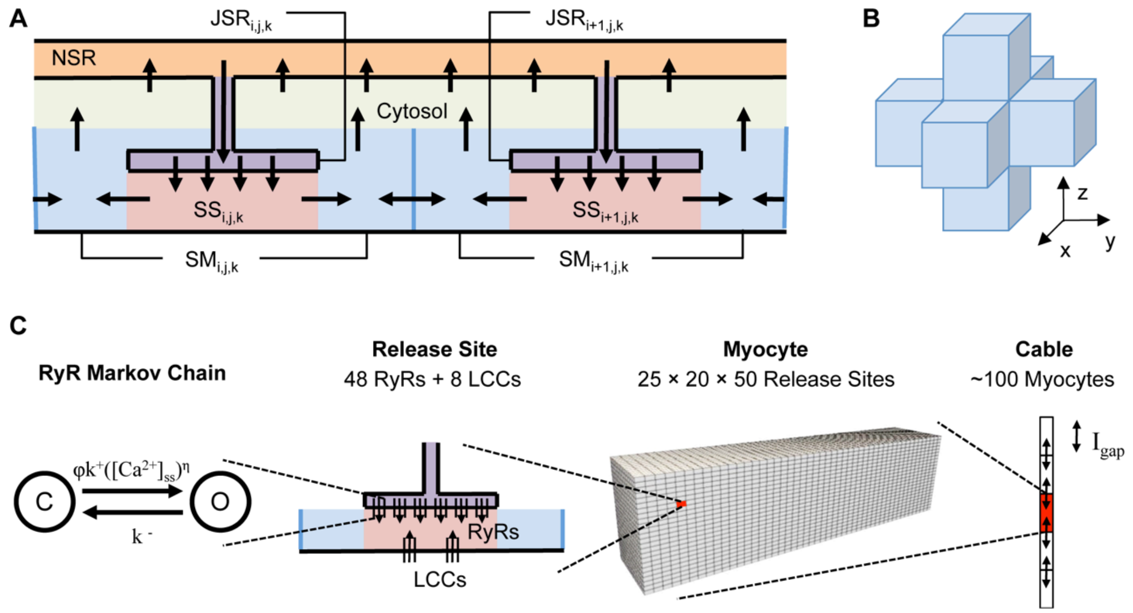
A
$JSR_{i,j,k}$
$JSR_{i+1,j,k}$
NSR
Cytosol
$SS_{i,j,k}$
$SS_{i+1,j,k}$
$SM_{i,j,k}$
$SM_{i+1,j,k}$
B
z
y
x
C
RyR Markov Chain
Release Site
48 RyRs + 8 LCCs
Myocyte
25 × 20 × 50 Release Sites
Cable
~100 Myocytes
$\varphi k^{+}([Ca^{2+}]_{ss})^{\eta}$
C
O
k^{-}
RyRs
LCCs
I_{gap}

Figure 4.2 Multiscale cell and tissue model schematics.

(A) Diagram of intracellular Ca^{2+} compartments and transport. At each release site at coordinates (*i*,*j*,*k*), Ca^{2+} is released via RyRs from the JSR into the dyadic subspace (SS) and diffuses into a submembrane (SM) compartment. Ca^{2+} diffuses between SM compartments of adjacent release sites in the 3D lattice, as depicted in panel (B). Ca^{2+} can also diffuse from the SM into a single cell-averaged cytosolic compartment and can be transported by the SERCA pump from the cytosolic compartment into a single network SR (NSR), which refills the JSR. (C) Illustration of the different spatial scales incorporated in the tissue model including (from left to right) the 48 stochastic RyRs in each of the 25,000 release sites of a single cell. Hundreds of cells are coupled via gap junction currents to form the fiber model.

4.2.2 Fiber model

The 3D cell model was incorporated into a tissue-scale model of a 1D fiber of myocytes. Figure 4.2*C* depicts the multiple scales of model components, from single ion channels to the multicellular fiber. The 3D cell model was augmented with a current carried by the gap junctions at either ends of each cell (I_{gap}). The current from cell *i* into an adjacent cell *i*+1 is given by:

$$I_{gap,i,i+1} = g_{gap}(V_i - V_{i+1}) \tag{4.3}$$

where g_{gap} is the gap junction conductance, which was adjusted to yield a conduction velocity of 55 cm/s. The membrane potential in the fiber was solved using the Crank-Nicolson method (147) with 50 μs time steps.

4.2.3 Beta-adrenergic stimulation

Sympathetic stimulation of the heart occurs through beta-adrenergic receptor activation, which activates the PKA pathway and leads to increased contractility (148). Beta-adrenergic stimulation is also known to be proarrhythmic and evoke spontaneous Ca^{2+} release (149). Cell model parameters were modified to reflect the effects of acute beta-adrenergic stimulation. LCC open probability was increased (150) by changing the fraction of active LCCs from 25% to 60% and setting 3-5% of the channels to gate in a high-activity mode, in which the mean open time was increased from 0.5 to 5.8 ms (151, 152). Enhanced activation of inward currents was implemented for I_{Kr} using modifications described previously (152) and for I_{Ks} by shifting the V_m-dependence of activation by -35 mV and increasing conductance by 40% (153). SR Ca^{2+} loading was facilitated by reducing SERCA pump K_d for $[Ca^{2+}]_i$ by 50% (154). RyR opening rate was increased by 50% to reflect increased SR Ca^{2+} leak observed in experimental studies

(155). Unless otherwise noted, these conditions were applied to all simulations in this study.

4.3 Results

4.3.1 Cell Model Properties

In order to reproduce protocols designed to measure excitation-contraction coupling, membrane potential was stepped to varying test potentials for 200 ms from a holding potential of -80 mV. The dependence of normalized peak RyR and LCC Ca^{2+} fluxes on the test potential and corresponding excitation-contraction coupling gain values were similar to those observed experimentally (73) (Figure 4.3 *A*, *B*).

Under control conditions, model action potentials (APs) and $[Ca^{2+}]_i$ transients were similar to those of normal ventricular myocytes (156), with an AP duration of approximately 320 ms (Figure 4.3*C*). Simulating the effect of beta-adrenergic stimulation increased the amplitude of the AP plateau as well as $[Ca^{2+}]_i$ transient amplitude and decay rate in addition to decreasing the AP duration to ~255 ms (152).

$[Ca^{2+}]_{nsr}$ was clamped at increasing values to test the relationship between SR Ca^{2+} load and leak. The model exhibited an exponential leak-load relationship that is similar to experimental estimates (9, 77) (Figure 4.3*D*). Spontaneous Ca^{2+} waves formed at a threshold Ca^{2+} load, at which wave fronts of propagating Ca^{2+} sparks emanated from random regions of high spark activity. Figure 4.3*E* shows a plot of SR Ca^{2+} leak along a cross-section through the center of the cell during a representative Ca^{2+} wave. The wave shape and velocity of 68 μm/s were similar to those observed in experimental studies (42).

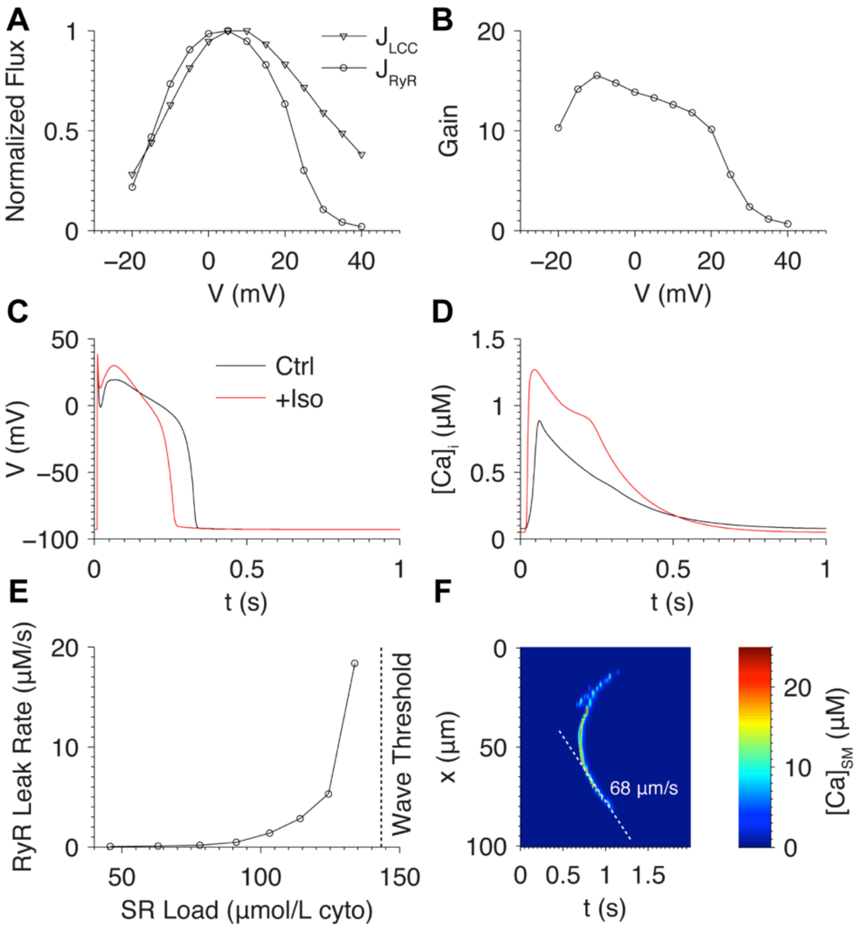

Figure 4.3 Cell model properties.

(A) Diagram of intracellular when the membrane was stepped to test potentials between -20 and 40 mV. (B) Excitation-contraction coupling gain, defined as the ratio of the normalized peak RyR to LCC Ca^{2+} flux at each test potential. (C) Representative action potentials and $[Ca^{2+}]_i$ transients under control (*black*) and beta-adrenergic (*red*) conditions. (E) Cell-wide SR Ca^{2+} leak rate via RyRs at varying SR Ca^{2+} loads. The dotted line indicates the lowest SR Ca^{2+} load tested that exhibited spontaneous Ca^{2+} waves. (F) Example linescan plot showing a Ca^{2+} wave in the baseline model when initialized with SR Ca^{2+} overload. All panels except where indicated in (C) and (D) were in the absence of beta-adrenergic stimulation.

4.3.2 Delayed afterdepolarizations during pacing

Myocytes are known to exhibit DADs and triggered APs under conditions that promote Ca^{2+} overload. Liu et al. demonstrated that ouabain overdose causes accumulation of $[Na^{+}]_i$, leading to Ca^{2+} overload and DADs (157). In addition, the authors showed that the production of reactive oxygen species, which are known to oxidize RyRs (106) and CaMKII (158), both of which enhance RyR activity, contributed to DAD generation.

To induce Ca^{2+} overload, model parameters were modified to simulate beta-adrenergic stimulation and to reflect the conditions in Liu et al. by inhibiting the Na+/K+ ATPase by 90%, elevating $[Na^{+}]_i$ to 22 mM, and increasing RyR opening rate to 5x that of baseline. Figure 4.4*A* shows APs when the cell was paced at 1 Hz under these conditions. Large DADs with ~ 20 mV amplitude occurred after the first and second shown beats. Inhibition of the Na+/K+ ATPase resulted in accumulation of $[Na^{+}]_i$ (Figure 4.4*B*). This caused Ca^{2+} waves to form more readily by reducing extrusion of Ca^{2+} via NCX in the SM compartment, thus elevating $[Ca^{2+}]_{ss}$ at sites adjacent to Ca^{2+} sparks and increasing the probability of Ca^{2+} spark propagation. This resulted in DADs of sufficient amplitude to activate the rapid Na+ current and trigger spontaneous APs.

Intermittent Ca^{2+} waves caused spontaneous $[Ca^{2+}]_i$ transients (Figure 4.4*C*). These waves were triggered by overload of SR Ca^{2+} (Figure 4.4*D*). The threshold SR load for Ca^{2+} waves was reduced to 76 µM/L cytosol compared to the baseline model threshold of 140 µM/L cytosol (see Figure 4.3*E*). This was due to high $[Na^{+}]_i$ and the greater RyR opening rate, which increased Ca^{2+} spark frequency and encouraged Ca^{2+} wave nucleation and propagation.

Elevated diastolic $[Ca^{2+}]_i$ has been implicated in DAD formation in experimental studies (45, 159). Diastolic $[Ca^{2+}]_i$ was ~250 nM when the DADs were sub-threshold. Triggered APs resulted in greater spontaneous $[Ca^{2+}]_i$ transients due to activation of LCCs and the cells exhibited elevated diastolic $[Ca^{2+}]_i$ of ~360-450 nM. This caused a reduction in the SR Ca^{2+} load threshold for spontaneous release to 65 μM/L cytosol due to the resulting increase in RyR opening rate and Ca^{2+} spark frequency.

These results demonstrate how SR Ca^{2+} overload drove the occurrence of DADs under pathophysiological conditions. Elevated RyR sensitivity and $[Na^+]_i$ accumulation led to DADs of sufficient amplitude to trigger action potentials during the diastolic intervals. In addition, these results illustrate the interplay between $[Ca^{2+}]_i$ and SR load dynamics during spontaneous Ca^{2+} release.

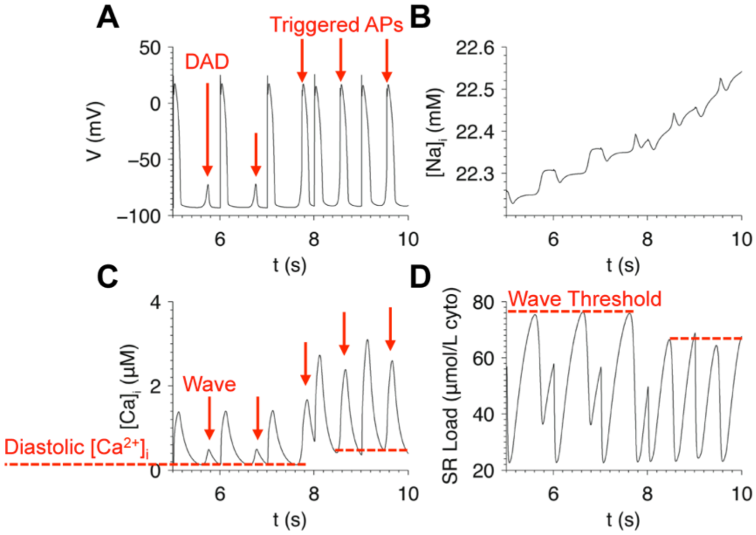

Figure 4.4 DADs induced by Ca^{2+} overload during 1 Hz pacing in the myocyte model.

(A) Sub-threshold DADs and triggered APs (*red arrows*) in between paced APs. (B) Accumulation of $[Na^+]_i$. (C) Spontaneous $[Ca^{2+}]_i$ transients caused by Ca^{2+} waves. Dotted lines indicate diastolic $[Ca^{2+}]_i$. (D) SR Ca^{2+} load. Dotted lines indicate threshold for Ca^{2+} overload that resulted in spontaneous Ca^{2+} waves. This threshold was decreased due to elevated diastolic $[Ca^{2+}]_i$ following triggered APs.

4.3.3 Effect of SR Ca^{2+} load on DADs

The relationship between SR Ca^{2+} load and spontaneous Ca^{2+} release was next investigated. Simulations were run using initial conditions that reflected the cell state just prior to the moment when SR Ca^{2+} load reaches the Ca^{2+} wave threshold following an AP. Initial $[Ca^{2+}]_i$ was set to 150 nM, similar to the level during the late decay phase of a $[Ca^{2+}]_i$ transient. Figure 4.5*A* shows DADs that occurred at the five different values of initial SR Ca^{2+} load shown in Figure 4.5*B*. At the highest SR Ca^{2+} load (v), the DAD amplitude was large enough to trigger an AP. Elevating SR Ca^{2+} load reduced the delay until spontaneous release, consistent with the observations of Wasserstrom et al. (47). The increase in DAD amplitude is consistent with a study by Schlotthauer and Bers, who demonstrated increased amplitude of caffeine-induced DADs at higher SR Ca^{2+} loads (160).

Figure 4.5*C* shows volume renderings of $[Ca^{2+}]_{SM}$ at three time points in each simulation. The number of Ca^{2+} wave nucleation sites (N_{nuc}) generally increased with SR Ca^{2+} load, in agreement with experimental studies in intact heart (46, 47). Therefore, the increase in SR Ca^{2+} load also increased RyR Ca^{2+} release flux (J_{RyR}) by enhancing the synchrony of RyR opening and number of nucleation sites.

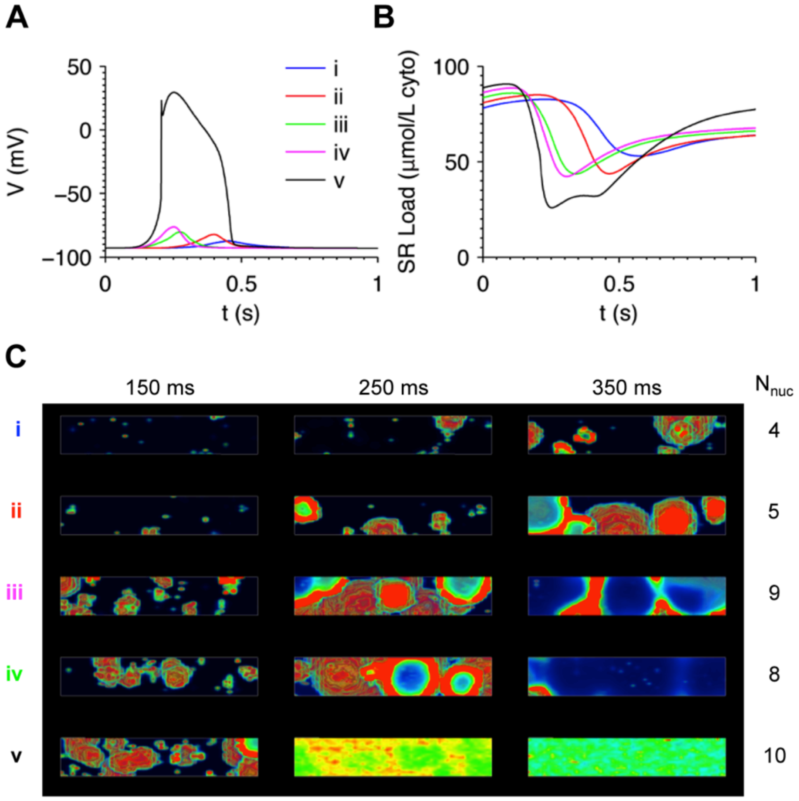

Figure 4.5 Elevating SR Ca^{2+} load accelerated Ca^{2+} wave formation and increased DAD amplitude.

(A) DADs resulting from initializing SR Ca^{2+} load to five different values as shown in (B). (C) Volume renderings of Ca^{2+} in the simulations at three time points illustrating the greater spontaneous Ca^{2+} wave activity at higher SR Ca^{2+} loads. The number of Ca^{2+} wave nucleation sites, N_{nuc}, is tabulated for each simulation.

Ensemble properties of DADs

We hypothesized that stochastic gating of the RyRs drives variability in Ca^{2+} wave dynamics and thus DAD amplitude and timing. To test this, five independent realizations were generated, each of which had identical initial conditions similar to (i) from Figure 4.5. The pseudorandom number generator seed was varied among the realizations in order to produce independent patterns of RyR gating. Figure 4.6*A* shows the resulting DADs, which exhibited marked variability in timing and amplitude. Delays until the DAD peak varied from 520 to 1209 ms and the amplitudes ranged from 2.3 to 6.2 mV. Thus substantial DAD variability could be attributed to the stochasticity of RyR gating.

Spontaneous Ca^{2+} release generates DADs by causing an inward current through NCX (43). Imaging and electrophysiology studies have suggested that NCX senses a $[Ca^{2+}]_{SM}$ that is higher than $[Ca^{2+}]_i$ because it is localized near the release sites (112, 144, 145). Therefore the driving force for inward NCX current is likely to be determined, in part, by the aggregate number of concurrent Ca^{2+} sparks occurring across the cell. This is consistent with a study showing that peak Ca^{2+} release flux is strongly correlated with the likelihood of ectopic activity (161). An ensemble of 98 independent simulations were performed to determine how peak $[Ca^{2+}]_i$ and J_{RyR} were related to DAD amplitude (Figure 4.6 *B*, *C*). There was a strong linear correlation between the peak membrane potential during the DAD, V_{max}, and the maximum $[Ca^{2+}]_i$ of the spontaneous $[Ca^{2+}]_i$ transient ($R^2 = 0.950$). However, there was a stronger relationship between V_{max} and the peak J_{RyR} value ($R^2 = 0.998$). This confirmed that the inward NCX current is primarily driven by J_{RyR} via the resulting rise in $[Ca^{2+}]_{SM}$.

Note that J_{RyR} reflects the combined Ca^{2+} release flux of all Ca^{2+} sparks occurring at any time. It was therefore expected that the variability in DADs was the result of spatio-temporal variations in Ca^{2+} wave dynamics. Figure 4.6*D* shows volume renderings of the Ca^{2+} waves in each simulation. Simulations (i) and (ii) were both associated with the highest-amplitude DADs as well as the greatest number of nucleation sites, while the remaining three had lower amplitudes and fewer nucleation sites. Note that in simulation (iv), two separate Ca^{2+} waves formed over 100 ms apart, resulting in a prolonged low-amplitude DAD with two peaks. These results are consistent with the strong correlation between V_{max} and maximum J_{RyR}, which reflects the timing and pattern of Ca^{2+} wave formation.

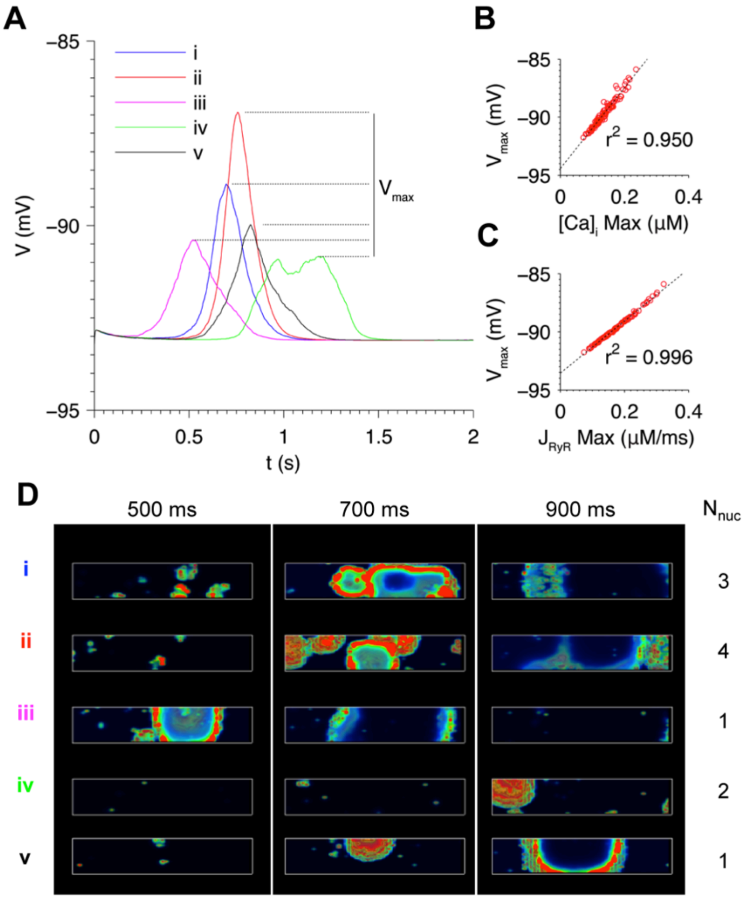

Figure 4.6 Variability of DAD timing and amplitude in five independent model realizations with identical initial conditions.

(A) Variability in DAD timing and amplitude. V_{max} is defined as the peak membrane potential during each DAD. Strong correlations were observed between V_{max} and both the maximum of the spontaneous $[Ca^{2+}]_i$ transient (B) and RyR Ca^{2+} release flux (C). (D) Volume renderings of Ca^{2+} wave dynamics at three time points in each simulation. The number of nucleation sites, N_{nuc}, was higher in simulations (i) and (ii) which had greater DAD amplitude.

4.3.4 Dependence of DAD distribution on total cell Ca^{2+} and I_{K1} density

In this section, the statistical relationships between Ca^{2+} loading and DAD amplitude and timing in ensemble simulations are investigated. Figure 4.7*A* depicts the variability in sub-threshold DADs when initial SR Ca^{2+} load was varied. The shaded regions represent the second and third DAD quartiles. Consistent with the findings from the individual cell simulations in Figure 4.5, DAD delay decreased and amplitude increased with SR Ca^{2+} load.

Recall that diastolic $[Ca^{2+}]_i$ played a critical role in determining the SR Ca^{2+} wave threshold during pacing (see Figure 4.4). The effect of increasing $[Ca^{2+}]_i$ on the DAD distribution when SR Ca^{2+} load is held constant was next tested (Figure 4.7*B*). Elevating $[Ca^{2+}]_i$ had an effect similar to increasing SR Ca^{2+} load, reducing the delay and increasing the amplitude of the DADs.

The inward rectifier K^+ current, I_{K1}, is the primary membrane current that stabilizes V_m at the cell's resting potential and plays a critical role in protecting the cell from triggered APs. I_{K1} density down-regulation is associated with ventricular arrhythmias in diseases such as heart failure (162), Andersen's syndrome (163), and long QT syndrome (164). Figure 4.7*C* shows DAD distributions when I_{K1} density was reduced by 50% and $[Ca^{2+}]_i$ was varied. This caused an apparent increase in DAD amplitude and variability compared to cells with normal I_{K1}. Note that in the 350 nM $[Ca^{2+}]_i$ case, only one of the 98 realizations produced a sub-threshold DAD.

Figure 4.7*D* shows the average and standard deviation of V_{max} as a function of the total cell Ca^{2+}, which was calculated as the combined total of buffered and free Ca^{2+} in the cytosol and SR. These results demonstrate two important conclusions. First, in the baseline model with normal I_{K1}, the distributions of V_{max} were identical as a function of total cell Ca^{2+} when SR $[Ca^{2+}]$ and $[Ca^{2+}]_i$ were varied. This strongly suggests that DADs are driven by overload of total cell Ca^{2+} and not just SR Ca^{2+} load. Second, reducing I_{K1} by 50% caused a marked increase in the average and standard deviation of V_{max}. In this case, Vm was more sensitive to the inward I_{NCX} during the DAD because of the reduced outward I_{K1} current opposing membrane depolarization. Therefore the DAD amplitude was greater for a given I_{NCX}, causing an increase in mean. Similarly, standard deviation was greater because V_m was more sensitive to variability in I_{NCX}.

Total cell Ca^{2+} was also strongly correlated with DAD delay and synchrony, as measured by the distribution of the time until the DAD peak occurred (Figure 4.7*E*). Increasing cell Ca^{2+} reduced DAD delay and increased synchrony. These distributions are comparable to those reported by Wasserstrom et al. (47). DAD delay did not considerably change with 50% I_{K1} reduction because it is determined primarily by the timing of Ca^{2+} wave formation, which was not affected by the I_{K1} density.

As total cell Ca^{2+} increased, the higher DAD amplitudes made it more likely that the threshold membrane potential for triggering an AP (~-55 mV) could be reached. The probability that a triggered AP occurred is shown in Figure 4.7*F*. Reducing I_{K1} by 50% caused triggered beats to occur at lower Ca^{2+} loads, consistent with the observed increase in DAD amplitude.

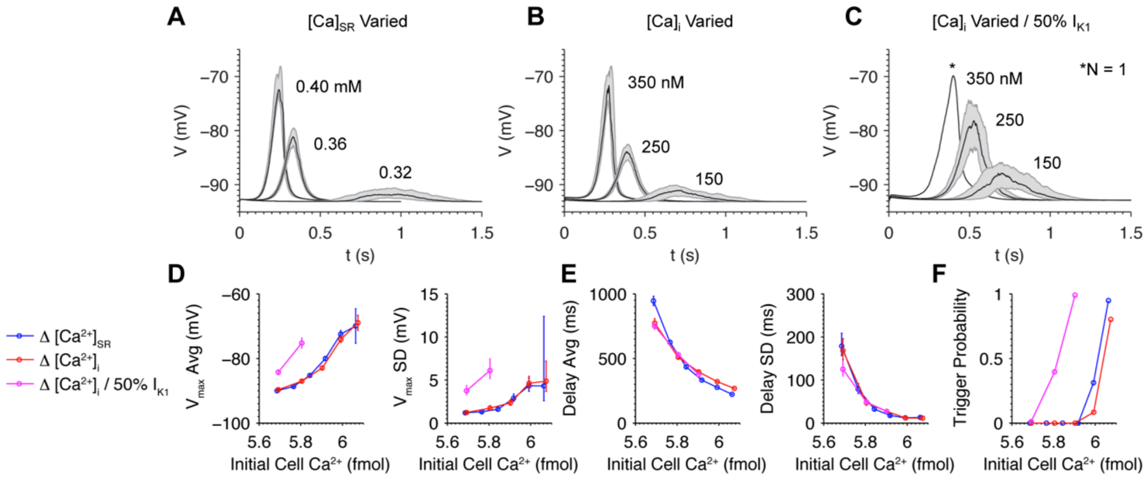

Figure 4.7 Roles of total cell Ca^{2+} and I_{K1} density in DAD distribution.

DAD distributions when initial (A) SR $[Ca^{2+}]$ and (B) $[Ca^{2+}]_i$ were varied in the baseline model. (C) DAD distributions when varying initial $[Ca^{2+}]_i$ after reducing I_{K1} density by 50%. Shaded regions indicate the middle quartiles of the membrane potential for sub-threshold events. Dark lines indicate median values. Statistics of V_{max} (D) of sub-threshold events and delay until DAD peak (E) are shown when $[Ca^{2+}]$ SR was varied (*blue*), $[Ca^{2+}]_i$ was varied (*red*), and $[Ca^{2+}]_i$ was varied with 50% reduction in I_{K1} density (*magenta*) as a function of total cell Ca^{2+}. Error bars indicate standard deviation of the estimates. (F) Dependence of triggered AP probability of total cell Ca^{2+}.

4.3.5 Probabilistic triggered activity in a paced fiber of myocytes

In the previous section, it was shown that triggered APs occurred with a probability that depended on the Ca^{2+} load and I_{K1} density. Simulations were performed to test whether the model could produce probabilistic triggered activity in a 1D fiber of myocytes during pacing. Figure 4.8*A* shows the membrane potential of a fiber paced at 0.5 Hz under conditions similar to those in Figure 4.4 with $[Na^+]_i$ set to 19 mM. To reflect a state of pathological remodeling, I_{K1} density and gap junction conductance were each reduced by 50% as observed in HF (162, 165). $[Na^+]_i$ was decreased to 10 mM in the outer twenty-four cells on either end of the fiber to prevent boundary effects on DAD amplitude. DADs, appearing as faint bands of depolarization between the paced beats, reached V_{max} values between approximately -70 and -60 mV. This is consistent with experimental observations of synchronized spontaneous Ca^{2+} release causing DADs in intact heart following rapid pacing (46).

The model exhibited considerable variability in V_{max} along the length of the fiber. To investigate the source of this variability, the state of the model at time $t_{restart}$ immediately after the third paced beat was recorded. A set of three independent realizations were run starting in that state but with different pseudorandom number generator seeds.

Figure 4.8*B* shows (i) the DAD from the original simulation in Figure 4.8*A* at 4.9 s and (ii)-(iv) the three additional simulations initialized at $t_{restart}$. Each simulation exhibited substantial differences in DAD amplitude along the fiber. In panel (iv), a traveling action potential wave was observed. The wave originated from a region of locally high DAD amplitude near cell no. 50 and emanated in either direction along the fiber.

These results illustrate that arrhythmic events can occur probabilistically in tissue. By restarting the simulations immediately prior to the DADs, it became evident that the variability in DAD amplitude was due to variations in the stochastic events that occurred in this brief time window. Taken together with the results from Figure 4.6 and Figure 4.7, the variability in DAD amplitude in the fiber could therefore be attributed to the underlying randomness of Ca^{2+} wave dynamics and thus stochastic RyR gating.

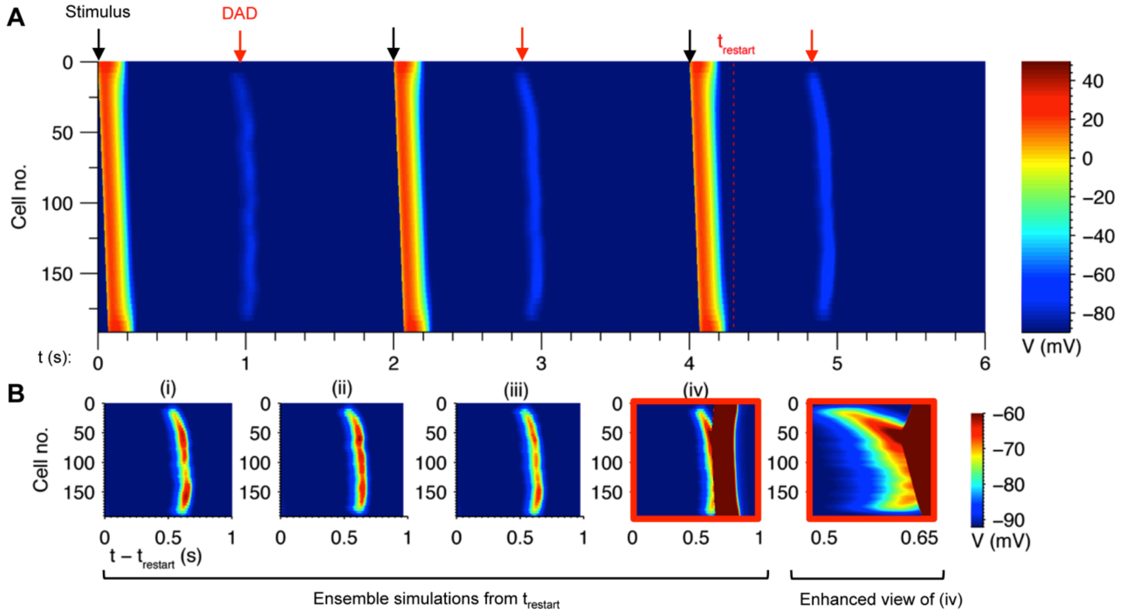

Figure 4.8 Probabilistic triggered activity caused by DADs in the fiber model.

(A) Fiber of 192 cells paced at 0.5 Hz by applying a stimulus current for 2 ms to the first two cells in the fiber (*black arrows*). DADs occurred between paced beats (*red arrows*). (B) Ensemble simulations (i)-(iv) initialized to the state at time $t_{restart}$ in panel (A). (i) corresponds to the simulation in panel (A). Enhanced view of (iv) is shown at right.

4.3.6 Roles of Ca^{2+} loading, I_{K1} density, and g_{gap} in fiber DADs

Conditions reflecting pathological remodeling influenced the distribution of V_{max} in the fiber. Figure 4.9*A* shows fiber simulations when all cells are initialized to identical initial conditions with Ca^{2+} overload in the baseline model. The resulting DADs resembled those from the paced fiber shown in Figure 4.8. As in individual cells, V_{max} increased with initial $[Ca^{2+}]_i$. However, at the highest $[Ca^{2+}]_i$ the range of V_{max} was 2.8 mV, which indicated that there was much less variability than in individual cells at similar Ca^{2+} loads (standard deviation >4 mV, see Figure 4.7*D*). This reduction in variability was due to electrotonic coupling through I_{gap}. This provided a pathway for the charge carried by inward I_{NCX} to diffuse to adjacent cells, thus attenuating spatial gradients in V_m.

Figure 4.9*B* shows similar simulations where I_{K1} density was reduced by 50%. This resulted in greater fluctuations of V_{max} and range of 8.0 mV. This is consistent with the observed increase in V_{max} standard deviation under the same condition in isolated cells (see Figure 4.7*D*). Reducing g_{gap} by 50% in addition to 50% I_{K1} further amplified V_{max} spatial fluctuations, resulting in a range of 10.2 mV (Figure 4.9*C*). The increase in range arose from the reduced electrotonic load experienced by each cell. These results demonstrate how perturbations to I_{K1} and g_{gap} increase the likelihood of observing large DADs.

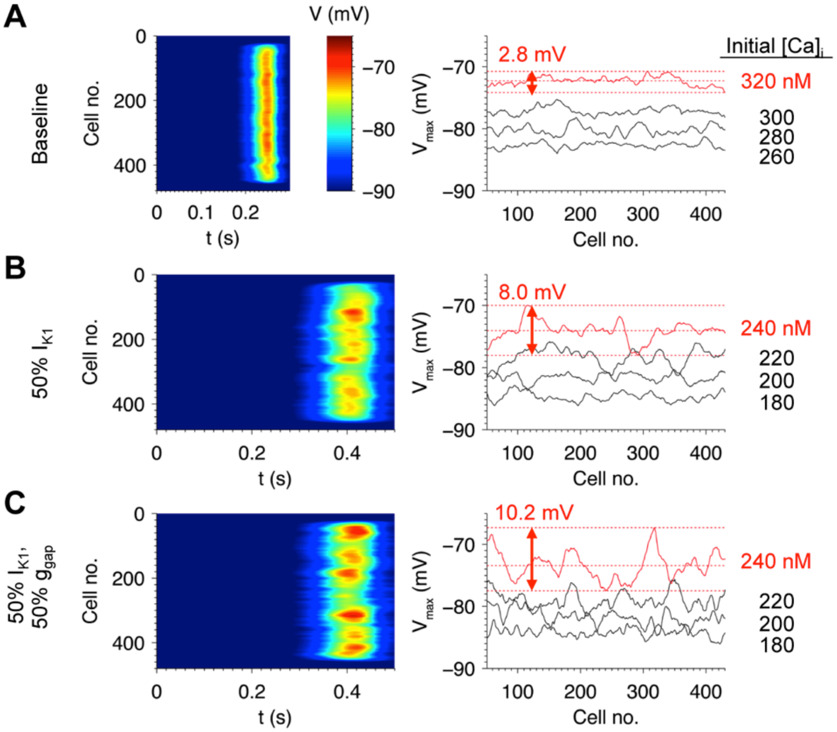

Figure 4.9 Roles of initial $[Ca^{2+}]_i$, I_{K1} density, and g_{gap} in DAD variability in the fiber model.

(A) Spatiotemporal profile of V (*left*) and V_{max} profile (*right*) in a 480-cell fiber under baseline conditions. Similar simulations are shown with 50% I_{K1} reduction (B) and both 50% I_{K1} and 50% gap junction conductance (C). The range of V_{max} values are indicated for the red traces, which correspond to the images at right. To avoid boundary effects, the outer 24 cells on either end were initialized to normal SR loads. The inner cells were initialized to identical initial conditions to those of Figure 4.7.

4.3.7 Overview of method for estimating rare event probabilities

The results from the preceding sections suggest that spatial fluctuations in V_{max} can result in a triggered beat emanating from a cluster of cells exceeding the threshold V_m (~-55 mV). For a fiber of a given length, the probability of this event is dependent on both the mean V_{max} and the likelihood of a deviation from the mean large enough to reach threshold. Under conditions where the mean V_{max} is far below threshold, however, it was unclear whether it would be possible to observe a large fluctuation that causes a triggered beat. Furthermore, we sought to characterize the likelihood of such events by estimating the upper tail of the V_{max} distribution.

We hypothesized that extreme deviations in V_{max} could be caused by rare spatially clustered synchronized release events. Estimating the probability of rare events (e.g. 1 in 10^6) would be computationally prohibitive with the full biophysical model. Therefore a method was developed for estimating the probability of such events using the output from a single fiber simulation. By assuming independence of the spontaneous Ca^{2+} release among the cells in the fiber, cell J_{RyR} profiles were resampled by shuffling the cell positions to generate independent realizations. A spatial smoothing filter and linear transformation was then applied to J_{RyR} to estimate fluctuations in V_{max}. The following sections state the method and its assumptions, validate its accuracy for estimating DAD probabilities, and characterize the how I_{K1} density and g_{gap} affect the likelihood of extreme events.

4.3.8 Filtering method for estimating V_{max} from J_{RyR}

A filtering method was developed for estimating V_{max} from the spatiotemporal profile of J_{RyR} in a fiber. The left column of Figure 4.10*A* shows the simulation from Figure 4.9*A* where $[Ca^{2+}]_i$ was initialized to 300 nM, and the right column illustrates the steps used in the filtering method. The first step in the method was to apply a uniform averaging filter to J_{RyR} at each point in time to obtain a spatially smoothed profile

$$J'_{RyR}(x,t) = \frac{1}{W} \sum_{k=-(W-1)/2}^{(W-1)/2} J_{RyR}(x+k,t) \quad , \tag{4.4}$$

where x refers to cell index, t refers to time, and W is the width of the filter (an odd integer). For each cell, the maximum J'_{RyR} value over all time was computed:

$$J'_{\max}(x) = \max_t \left\{ J'_{RyR}(x,t) \right\} \quad . \tag{4.5}$$

The value of W that maximized the correlation coefficient between V_{max} and J'_{max} was selected. We then normalized J'_{max} to obtain estimates of V_{max} using the formula

$$V'_{\max}(x) = \mu_V + \frac{\sigma_V}{\sigma_J}\left(J'_{\max}(x) - \mu_J \right) \quad , \tag{4.6}$$

where μ_V and σ_V are the mean and standard deviation of V_{max} of the simulation, and μ_J and σ_J are the mean and standard deviation of J'_{max}. Note how in the example of Figure 4.10*A* the estimated profile of V' closely resembled V.

The filtering method was applied to simulations of DADs with baseline conditions, 50% I_{K1}, and both 50% I_{K1} and 50% g_{gap} (Figure 4.10*B*). In non-baseline conditions, the initial $[Ca^{2+}]_i$ was adjusted from 300 to 220 nM so that μ_V would be approximately equal to that of the baseline. The width W of the smoothing filter was dependent on the fiber model parameters and therefore was optimized separately for each case. Table 1 shows the parameter fits for each condition. The resulting fits of V'_{max} to V_{max} were compelling, as measured by high correlation coefficient values ($\rho > 0.94$). All values of μ_V fell in a small range near -78 mV, while the values of μ_J in the two non-baseline conditions were less than half of baseline due to their lower Ca^{2+} loads.

The increase in V_{max} variability in the two pathological conditions is reflected in the parameters of the filtering model. It can be shown that the quantity $S_V = (\sigma_V/\sigma_J)/W$ scales with the standard deviation of V'max (see Appendix C). Recall that 50% I_{K1} reduction increased variability of V in the cell model (see Figure 4.7). However, S_V was 28% larger in this case compared to baseline, primarily reflecting the higher value of σ_V. Imposing 50% g_{gap} resulted in a filter width of only 27 cells compared to 43 and 49 in the other cases due to local decoupling of cells when gap junction conductance is decreased. This caused S_V to be 87% larger than baseline and 46% larger than 50% I_{K1} alone.

These results show that the filtering method accurately estimates fluctuations in V_{max} based on the J_{RyR} profile. In addition, the empirical relationships derived here between J_{RyR} and V_{max} also yield insight into how reductions in outward currents and electrotonic coupling enhance spatial fluctuations in V_{max}.

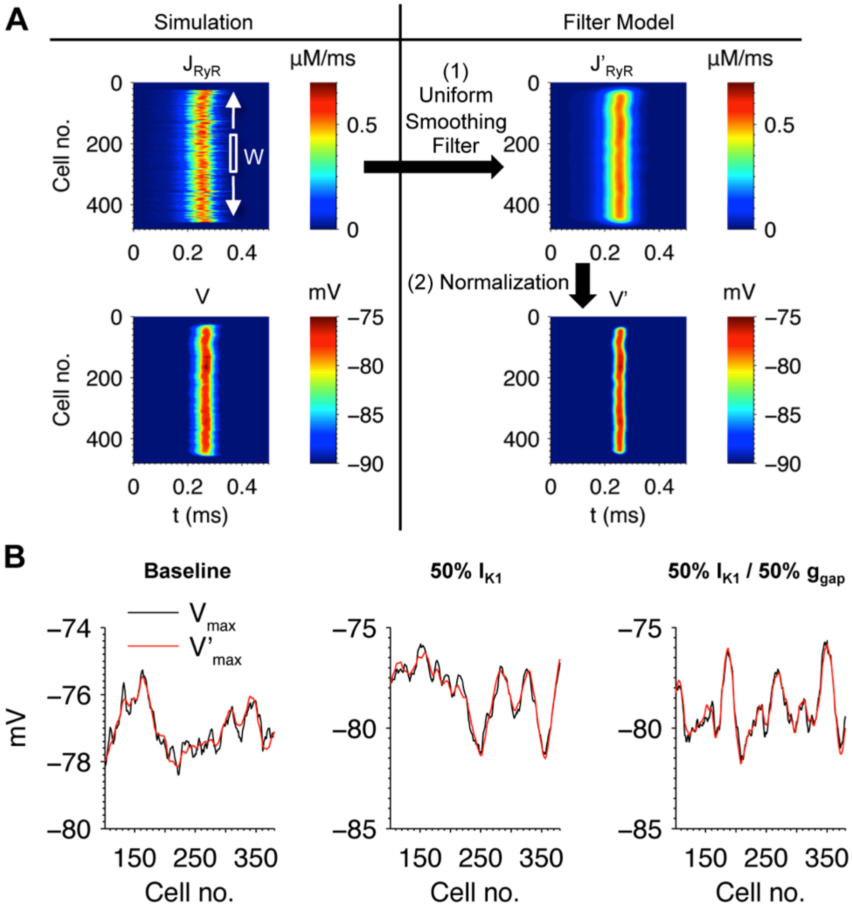

Figure 4.10 Filtering method for estimating V_{max} from the spatiotemporal J_{RyR} profile in a fiber.

(A) Illustration of the filtering method for an example fiber simulation. A uniformly-weighted spatial smoothing filter of width W was applied to the spatiotemporal J_{RyR} profile. The maximum values of the filtered profile were then normalized to obtain an estimate of the voltage profile (see text for details). (B) The filtering method was applied to three fiber simulations using the conditions indicated above each plot. The filtering method result (*red*) accurately estimated V_{max} from the original simulation (*black*). Parameters are listed in Table 1.

	$[Ca^{2+}]_i$ (nM)	ρ	μ_V (mV)	μ_J (μM ms^{-1})	σ_V (mV)	σ_J (μM ms^{-1})	W (cells)	S_V
Baseline	300	0.949	-77.0	0.526	0.665	0.00873	43	1.77
50% I_{K1}	220	0.973	-78.3	0.248	1.38	0.0124	49	2.27
50% I_{K1}, 50% g_{gap}	220	0.976	-79.1	0.242	1.34	0.0150	27	3.31

Table 4.1 Parameters used for filtering method in Figure 4.10.

4.3.9 Resampling method for estimating rare event probabilities

Samples of V_{max} were obtained by shuffling cell positions in the J_{RyR} profile, as illustrated in Figure 4.11*A*. The filter method was then applied to the shuffled J_{RyR} profile to estimate V_{max}. An example V_{max} profile obtained using this method is shown on the right. Note that the fluctuations about the mean μ_V were qualitatively similar to those of the original simulation. In Figure 4.8, it was shown how a triggered propagating wave originated from a region of the fiber exhibiting extreme DADs that reached the threshold for triggering a spontaneous AP. Therefore, events of interest were defined as the greatest value of V_{max} in the fiber, referred to here as V_{peak}.

The shuffling of cell positions makes two assumptions. The first is that the J_{RyR} profiles of the cells are independent and identically distributed stochastic processes. Implicit in this assumption is that for each cell the variability of membrane potential due to local spontaneous Ca^{2+} release does not affect its J_{RyR}. The second assumption is that the fiber contains a sufficient number of cells such that the true distribution of J_{RyR} is well represented by the collection obtained from a single simulation.

To validate our assumptions, the distribution of V_{peak} generated using this method needed to match that of the detailed biophysical model, which was estimated from 1,000 independent realizations. Simulating the ~500-cell fiber with 25,000 release sites in each cell was computationally prohibitive. For the purposes of the validation, the number of release sites was reduced to 2,500 and the fiber length to 96 cells. The values of μ_V and σ_V were computed using the V_{max} values from all cells in all fibers.

Figure 4.11*B* compares the true distribution to the distribution of V_{peak} values obtained from applying only the filtering method to the simulated J_{RyR} profiles (without shuffling). While this distribution exhibited a bias of -0.05 mV, it was not significantly different from the true distribution according to a non-parametric Kruskal-Wallis test after correcting for the bias by subtracting their means ($p = 0.89$). The shuffling method was then validated by resampling from the J_{RyR}'s in all 1,000 fibers to produce 1,000 96-cell fiber realizations and computing V_{peak} with the filtering method. While the resulting distribution also was biased by -0.08 mV, it was not significantly different from the true distribution after adjusting the means ($p = 0.69$) (Figure 4.11*B*). The upper tails of the distributions containing the extreme DADs of interest were also similar (Figure 4.11*C*). To validate the second assumption that sampling population of J_{RyR} is sufficiently large, these tests were repeated using a subset of five of the 1,000 fibers to compute μ_V, σ_V and the population of resampled J_{RyR}'s (bias +0.05 mV, $p = 0.68$). Therefore the method was also accurate using a total of <500 simulated cells. In summary, the method outlined here is a computationally efficient approach that permits the rapid estimation of the V_{peak} distribution using output from a single 500-cell fiber simulation.

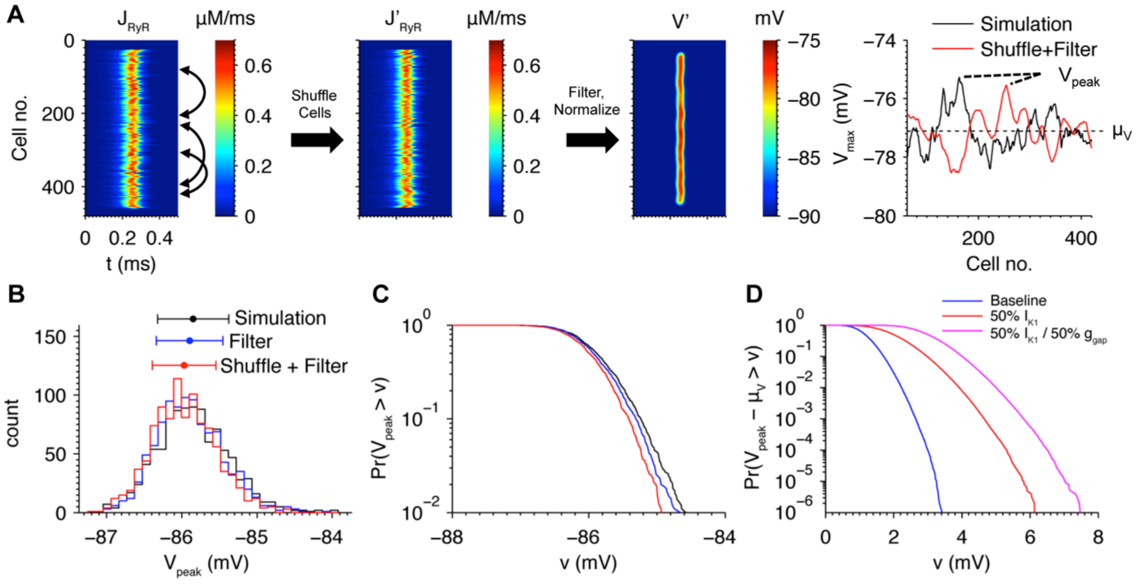

Figure 4.11 Method for estimation of rare extreme DAD probabilities.

(A) Example illustrating how independent fiber realizations are generated by shuffling cell positions and applying the filtering method. The resulting V_{max} profile of the original simulation (*black*) and V'_{max} obtained after shuffling (*red*) are plotted on the right. V_{peak} is defined as the maximum potential achieved in the fiber. (B) Histograms of V_{peak} from model simulations (*black*), the filtering method (*blue*), and shuffling method (*red*). See text for details. (C) Upper tail of the distributions from (B). (D) Predicted tail of V_{peak} distributions for fibers with the baseline model (*blue*), with 50% I_{K1} reduction (*red*), and with both 50% I_{K1} reduction and 50% g_{gap} (*magenta*). Distributions are plotted relative to the average V_{max}, μ_V.

4.3.10 Prediction of rare events

The resampling method was applied to the simulations from Figure 4.10*B* to estimate the probability of rare extreme DADs in the fiber model. Figure 4.11*D* plots the probability that (V_{peak}-μ_V) exceeded a given potential estimated from an ensemble of 10^6 realizations. Reducing I_{K1} by 50% shifted the distribution tail to greater amplitude DADs compared to the baseline model. The most extreme event observed was 6.1 mV above μ_V compared to 3.4 mV in baseline, corresponding to DAD amplitudes 41% and 21% above average, respectively. Reducing g_{gap} by 50% further increased the likelihood of larger DADs, with the most extreme event at 7.5 mV corresponding to a DAD amplitude 53% higher than average. These results demonstrate that reductions in I_{K1} and g_{gap} widen the distribution of DAD amplitude considerably and can increase the probability of occurrence of larger DADs by orders of magnitude.

To illustrate the nature of these rare events, the realizations exhibiting the greatest DAD amplitude were examined in each condition. Figure 4.12*A* plots V_{max} relative to the mean. The extreme DADs occurred in a localized region of ~20-40 cells that achieved a local maximum. Figure 4.12*B* shows the underlying J_{RyR} profiles and the filter window centered on the maximum DAD. In each case, the extreme event occurred at a cluster of cells where J_{RyR} tended to be greater and more synchronized than in the rest of the fiber.

In this section, the resampling method was employed to estimate the probability of extremely rare events in the fiber model. Reducing I_{K1} and g_{gap} greatly increased the likelihood of large DADs that deviate substantially from the average. It was further shown that these events are characterized by unlikely spatial clustering of high-amplitude, synchronized spontaneous Ca^{2+} release, thus confirming our hypothesis that variability in Ca^{2+} wave dynamics and RyR gating can result in rare arrhythmic events at the tissue scale.

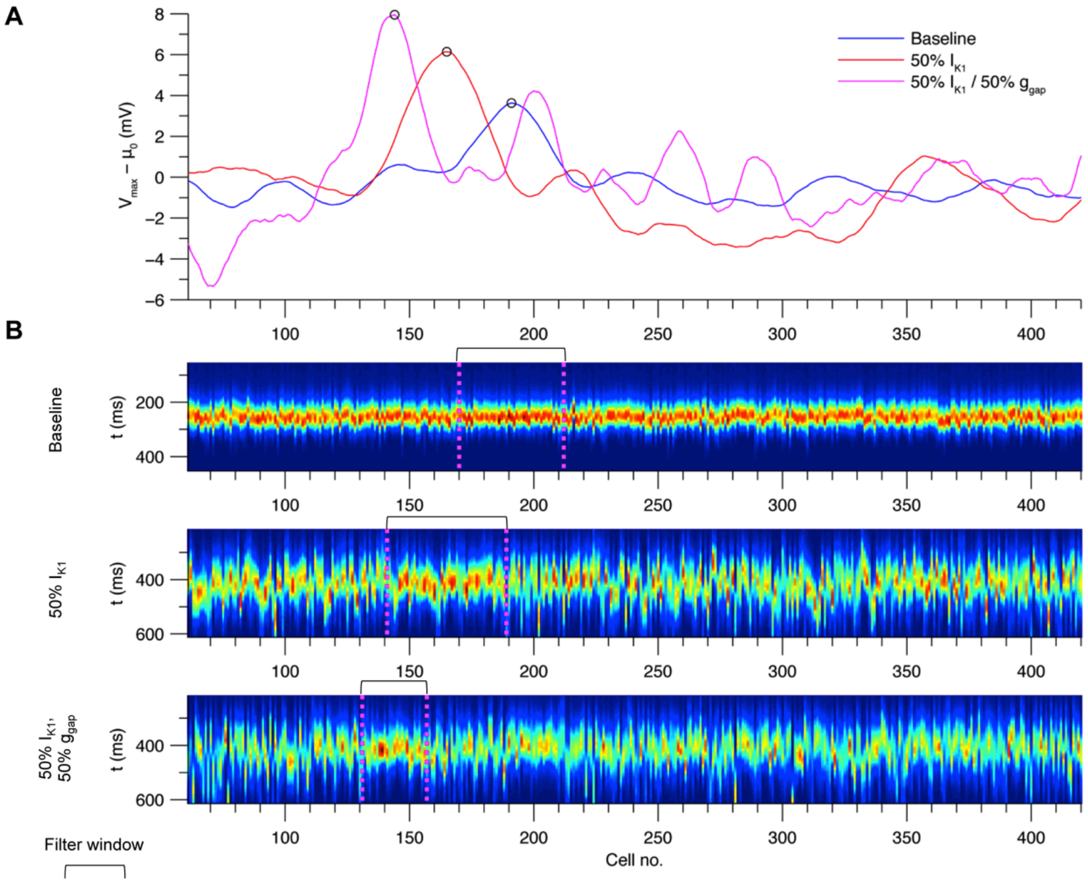

Figure 4.12 Realizations of rare extreme DADs.

(A) Plots of V_{max}-μ_V in the realizations from Figure 4.11*D* containing the most extreme DADs out of 10^6 trials. Curves correspond to the baseline model (*blue*), with 50% reduction of I_{K1} (*red*), and both 50% I_{K1} and 50% g_{gap} (*magenta*). (B) Spatiotemporal J_{RyR} profiles in each realization from panel (A). Brackets and dotted lines mark the location of the filter window centered on the extreme DAD.

4.4 Discussion

In this study we have presented a biophysically detailed stochastic computational model of the ventricular cardiac myocyte describing spatial Ca^{2+} diffusion between release sites and incorporated it into a tissue-scale model to study the mechanisms and statistical properties of DADs and triggered ectopic activity. Loading of SR Ca^{2+} is known to cause spontaneous Ca^{2+} release(43, 84, 160). In this model, Ca^{2+} waves were generated when under high SR Ca^{2+}, load passive diffusion of Ca^{2+} between release sites caused Ca^{2+} sparks to propagate across the cell. In agreement with experimental studies, RyR sensitivity modulated the threshold SR Ca^{2+} load at which this instability arises(166). Rather than explicitly modeling RyR regulation mechanisms such as phosphorylation by activated CaMKII (117) and PKA (23), allosteric channel decoupling due to PKA-dependent dissociation of FKBP12.6 (24), and oxidation by reactive oxygen species (106, 157), RyR opening rate was scaled such that the model reproduced experimentally observed triggered APs at 1 Hz pacing(157). $[Ca^{2+}]_{jsr}$-dependent regulation of the RyRs increases their sensitivity to cytosolic $[Ca^{2+}]$ (102, 167), but its role in spontaneous Ca^{2+} release is controversial. In the model of RyR gating used here, it played a minimal role in dynamically regulating RyR sensitivity because $[Ca^{2+}]_{jsr} < 1$ mM(16, 17).

The distribution of DADs was controlled by the total Ca^{2+} in the cell. This was revealed by the apparent change in the threshold SR Ca^{2+} load for spontaneous Ca^{2+} wave formation during pacing (see Figure 4.4). Elevated diastolic $[Ca^{2+}]_i$ increased RyR opening rate and thus perpetuated Ca^{2+} wave formation at lower SR Ca^{2+} loads. It also caused more rapid loading of the SR to induce overload. Cellular Ca^{2+} loading also increased the amplitude of DADs due to the greater number and concurrence of Ca^{2+}

wave nucleation sites, which is in agreement with experimental studies(46, 47). Consistent with our results, Wasserstrom et al. reported that cellular Ca^{2+} loading reduced DAD delay and increased synchrony associated this with greater likelihood of triggered activity (47).

Triggered events were investigated using the fiber model. Experimental study of the nature of DAD-induced arrhythmias is difficult due the limited temporal and spatial resolutions of live multiplex fluorescence imaging of tissue preparations. The model revealed that triggered beats originated at a region of localized high-amplitude DADs. We showed that these events occurred probabilistically due to random patterns of RyR gating and Ca^{2+} waves that gave rise to high-amplitude, synchronized Ca^{2+} release flux in a cluster of cells. Heterogeneity of cell types and intercellular variability of Ca^{2+} handling, may also play an important role in determining the likelihood and location of triggered foci (47) but were beyond the scope of this study. Furthermore, the potential effects of proarrhythmic beat-to-beat AP variability (168) or stochastic EADs (169), which could affect Ca^{2+} loading and DAD timing, were not examined.

The role of I_{K1}, which acts to stabilize the resting membrane potential, affected the DAD distribution in isolated cells. Loss of I_{K1} function has been associated with arrhythmogenesis in diseases such as heart failure (162), Andersen's syndrome (163), and long QT syndrome (164). The model exhibited a considerable increase in DAD amplitude and variability in both isolated cells and the fiber when I_{K1} density was reduced by 50%. Reduction of gap junction conductance, another pathological feature of diseases such as HF (165), also increased the variability of DAD amplitude in the fiber by reducing the spatial scale of electrotonic coupling. These findings are consistent with a modeling study that showed that fewer contiguous cells are required to exhibit DADs to produce a triggered beat under such conditions(170).

A significant contribution of this work is that sudden arrhythmias can be caused by stochastic molecular events. A rigorous, computationally efficient method was developed to estimate the probability of extreme DADs. There were two important conclusions from using this method. First, that variability of the inward current due to stochastic RyR gating caused random patterns of Ca^{2+} wave dynamics and results in substantial DAD variability at the tissue scale, particularly in the pathological states tested where I_{K1} and g_{gap} were reduced. Second, while one could imagine a possible case where a contiguous cluster of cells exhibit large synchronized spontaneous Ca^{2+} release, the probability distribution of such events has not been well characterized. In a 496-cell fiber with reduced I_{K1} and gap junction coupling, the largest DAD amplitude out of 10^6 realizations had amplitude ~50% greater than mean DAD amplitude. For such a fiber paced at 1 Hz and exhibiting a DAD after every beat, one could therefore expect to observe such an event approximately every 11 days. Thus extreme DADs, while quite rare, are still possible over feasible time frames. Further work is needed to estimate the probability of such events in whole heart, given the increased electrotonic coupling of 3D tissue and greater number of cells. Nevertheless the results presented here suggest that variability due to stochastic molecular events can play a large role in the initiation of cardiac arrhythmias and sudden cardiac death.

4.5 Conclusion

Ectopic heartbeats can trigger reentrant arrhythmias, leading to ventricular fibrillation and sudden cardiac death. Such events have been attributed to unstable Ca^{2+} handling in cardiac myocytes that results in spontaneous Ca^{2+} release and DADs under pathological conditions. However, the molecular mechanisms underlying the generation of ectopic foci are not well understood. Here we presented a multiscale model of cardiac tissue that incorporates a biophysically detailed 3D model of the ventricular myocyte. The cell model reproduces realistic spontaneous Ca^{2+} waves and DADs driven by stochastic Ca^{2+} RyR gating under conditions promoting cellular Ca^{2+} overload. The model was used to study the mechanisms of DAD variability. Key factors influencing the distribution of DAD amplitude and timing included the cell Ca^{2+} load and I_{K1} density. It was further shown how random patterns of RyR gating and Ca^{2+} wave dynamics could thus give rise to probabilistic triggered activity in a fiber of myocytes. Pathological reductions in I_{K1} density and gap junction conductance caused a substantial increase in the variability of DAD amplitude in the fiber model. Lastly, a novel method for estimating the probability of rare stochastic events is presented and used to predict the likelihood of extreme (i.e. rare, high-amplitude) DADs, which were characterized by randomly organized clusters of cells exhibiting synchronized, high amplitude Ca^{2+} release flux. We concluded that variability in DAD amplitude at the tissue scale can be attributed to stochastic molecular events and that the probability of rare arrhythmic events is substantially increased under conditions reflecting pathophysiological remodeling in heart disease.

Chapter 5 Models and Simulations as a Service

5.1 Tool Description

5.1.1 Globus Galaxies

Over the past several years we have developed, deployed, and operated an enhanced version of the Galaxy framework for the Cardiovascular Research Grid (CVRG) (171) community called Globus Galaxies (172). This Globus Galaxies instance provides: integrated high-performance and easy to use data management capabilities using Globus Transfer (173); custom “recipes” to install the Galaxy framework preconfigured with analytical tools and pipelines using virtual machines; integration with the BioPortal Ontology Server (174) through its REST interface; novel on-demand computational infrastructure using Amazon EC2 and HTCondor (175) for elastic scaling; a user-configurable node provisioner for managing elastic scaling by determining when instances should be added and removed from the compute cluster as a result of tasks waiting in the execution queue. We have also created a framework that helps determine the computational characteristics of a particular analysis in terms of the number of CPU cores and the amount of RAM required to run optimally. These profiles help create an optimal execution strategy for the application.

5.1.2 Tool Development

We have developed a set of Galaxy tools for using computational models. All tools can be accessed at https://cvrg.galaxycloud.org. Galaxy tools are typically comprised of two files: a software application such as the model program and an XML configuration document that tells Galaxy how to use the application. Galaxy provides an XML specification for configuring the application’s input and output data files, parameter fields, and documentation. The developer must also specify a command to invoke the main computations performed by the application. Because of this constraint, applications must be implemented such that they receive the paths of input and output files and parameter values as arguments. The application must be accessible as a web-services or an executable on the Galaxy server. Installation of applications and incorporation of third-party software dependencies can be performed manually by a server administrator, or automated using the dependency package manager in the Galaxy Tool Shed (56). Therefore models, modeling tools, and third-party applications can be integrated into a Galaxy tool as long as they can be run programmatically. This includes models that are compiled (e.g. C/C++, FORTRAN, Java), scripted (e.g. MATLAB, R, Python), or available through an application programming interface (API) (e.g. software libraries, web services). This excludes models, however, that can only be run through graphical user interfaces.

5.2 Results

5.2.1 SRS Model Tools

We have developed a Galaxy tool suite for customizing and running the SRS model as an example of how our approach is able to deliver RRS capabilities for complex models. The original SRS model was comprised of a set of executables that were used in different pipelines for running and analyzing the model. These executables performed separate tasks including generating the 3D mesh geometry, running simulations, and performing various post-processing computations. Here we have wrapped these executables into a set of Galaxy tools that streamlines the different workflows used to produce published analyses.

A recent study reported that the calsequestrin *R33Q* mutation associated with CPVT results in an increase of RyR mean open time (MOT) from ~ 2 to 10 ms (17). To illustrate the use of Galaxy workflows for simulating complex models, we ran two Ca^{2+} spark simulations of the SRS model to test the effects of the *R33Q* mutation on Ca^{2+} dynamics.

The first step is to run a meshing tool within Galaxy to generate the three-dimensional tetrahedral mesh used by the model. With this tool users can customize the geometry of the model, including release site dimensions and ion channel locations. The Galaxy simulation tool is invoked to run the model on this new mesh. Users can customize model parameters and run different types of simulations including individual or ensembles of multiple simulations for estimating statistical properties of the model. In the latter case, Galaxy launches ~1,000 parallel simulations on a 32-core AEC2 node. For the control simulation, we used the default set of parameters, which runs a single Ca^{2+}

spark simulation under normal conditions. For the *R33Q* simulation, we decreased the RyR closing rate parameter (k^-) from 0.50 ms^{-1} to 0.10 ms^{-1}. An offline three-dimensional rendering of a Ca^{2+} spark simulation is shown in Figure 5.1*A*.

To visualize simulation output, we developed a tool to mimic confocal linescan plots of simulation results. Figure 5.1*B* shows these linescan plots for the control and *R33Q* simulations. Analysis of these plots using Sparkmaster (68) revealed that the full duration at half-maximum increased by 45% compared to control, in agreement with experimental data (80).

We next designed a Galaxy tool for converting model output so that it can be readily viewed and visualized within Galaxy. Figure 5.1*C* shows graphs of Ca^{2+} dynamics during each spark generated using the Galaxy plotting tool. The increase in Ca^{2+} spark duration can be explained by the longer time until release termination, and the lower nadir of junctional sarcoplasmic reticulum Ca^{2+} concentration is consistent with experimental data (176). These results demonstrate how the complex SRS model and computational resources can be shared with and customized by others to predict the physiological implications of new experimental data.

Galaxy maintains a user "history" containing a list of datasets and executed tools from the current session. The contents and provenance of each history item can be viewed and downloaded. A collection of histories can be stored on the user's account, thus providing a persistent platform for managing multiple simulations and analyses. Importantly, Galaxy lets users share and publish histories and workflows. These are tagged with URLs that can, for example, be embedded in publications. By clicking on these links, readers may repeat simulations and recreate analysis results described in the publication. This was included in Chapter 2 figure captions. Similarly, Galaxy enables researchers to construct workflows using a graphical drag-and-drop editor. In contrast to a history, a workflow serves as a template for performing simulations and data analyses. An entire workflow can be executed, invoking the tools used in the workflow and returning the results to the user as a history when complete. Users can import a copy of a shared history or workflow into their own workspace, enabling them to run identical or customized simulations. To enhance transparency, users can embed workflows, histories, and documentation into a publishable webpage provided by Galaxy's "pages" feature. These features thus address issues of reproducibility in computational modeling by enabling users to readily access the provenance of simulations performed by other researchers. A hyperlink to the history containing the preceding simulation results is given in the caption of Figure 5.1, and a Galaxy page documenting different analyses is available at http://cvrg.galaxycloud.org/u/mwalker/p/calcium-spark-tools.

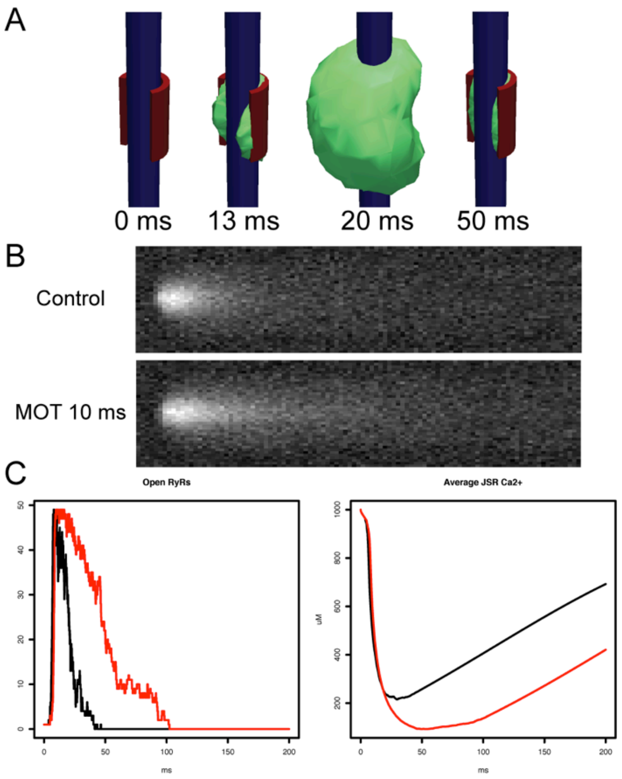

Figure 5.1 Spark simulation from the SRS model.

(A) The three-dimensional model depicting transverse-tubule (*blue*), junctional sarcoplasmic reticulum (*red*), and 1 µM Ca^{2+} concentration isosurface (*green*) during a Ca^{2+} spark. (B) Simulated confocal linescan plots of Ca^{2+} indicator fluorescence for control parameters (*top*) and when the RyR MOT was increased to 10 ms (*bottom*). Image dimensions are 200 ms across and 6 µm vertically. (C) Time-series plots using the control parameters (*black*) and with RyR MOT of 10 ms (*red*). Panels show number of open RyRs (*left*), and average junctional sarcoplasmic reticulum Ca^{2+} concentration (*right*). Simulation histories available at: http://cvrg.galaxycloud.org/u/mwalker/h/calcium-spark-mot-10ms.

5.2.2 XML-encoded Model Tools

The RRS capabilities of Galaxy can be leveraged when working with other applications to provide provenance of *in silico* experiments. To demonstrate a basic use case for SBML simulations, we developed a search interface within Galaxy that uses the BioModels Database web services to support discovery and import of models directly into Galaxy. The tool is able to access the database over SOAP web services using queries specified in the BioModels WSDL document (177). To simulate SBML models, we developed a wrapper tool for the COPASI simulation software (53), which can run simulations via the command line and therefore was suitable for integration into a Galaxy tool. The user selects the desired SBML model, provides solver parameters, and selects whether to run a deterministic or stochastic simulation. Using these tools, we imported a model of PKA signaling by Saucerman et al. from BioModels and replicated Figure 2*B* of the original publication (178) (Figure 5.2*A*).

We have also developed tools for editing and simulating CellML models in Galaxy. Using the upload tool, we first imported the ten-Tusscher epicardial cell model (179) via its URL in the CellML model repository (180). We developed a CellML editing tool that utilizes the CellML Python API (52) to enable users to modify parameter values and initial conditions. Thus from a parent model, one can produce one or more child models representing variations in cell types or conditions. We reduced the I_{Ks} conductance four-fold to derive an M cell model variant and retrieved the endocardial model version from the CellML repository for comparison. OpenCOR is an open-source CellML modeling environment that supports running simulations via the command line (54) and therefore could be wrapped in a Galaxy tool to simulate CellML models. We simulated action potentials for the three models at 1 Hz pacing (Figure 5.2*B*), as shown in Figure 10 of the original publication (179).

Hyperlinks to the histories used to generate Figure 5.2 are included in the figure caption. Thus we have demonstrated how existing SBML and CellML tools can be adapted for use within Galaxy, thereby taking advantage of its RRS capabilities.

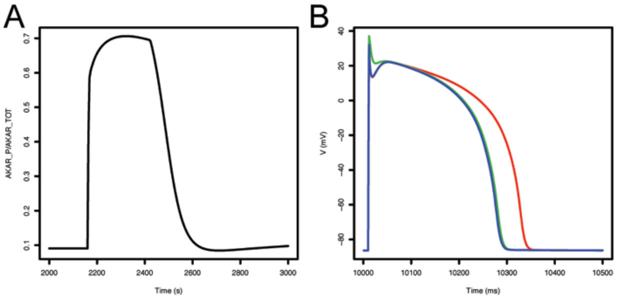

Figure 5.2 Use of XML-encoded models in Galaxy.

(A) The COPASI Galaxy tool was used to simulate a model of PKA signaling (178). Plot of AKAR2 phosphorylation kinetics following application of isoproterenol followed by propranolol. Simulation history available at: http://cvrg.galaxycloud.org/u/mwalker/h/saucerman2006. (B) Action potentials of the epicardial (*blue*), M cell (*red*), and endocardial (*green*) ten Tusscher human ventricular myocyte model (179). Simulation history available at: http://cvrg.galaxycloud.org/u/mwalker/h/tentusscher.

5.2.3 Hodgkin-Huxley Model Composition

Hierarchical model composition is a powerful technique for building models from smaller components. It enables modelers to rapidly prototype new models and facilitates meta-analyses to compare existing ones. Galaxy is a suitable environment for model composition. To demonstrate this, we developed two tools for building Hodgkin-Huxley (HH) type cell models (181) that incorporate ion channels as customizable components. Users can drag and drop new channels into Galaxy's graphical workflow editor. Each channel can be linked to a simulator component that incorporates the channels into a cell model, and simulates the response to a stimulus current. Figure 3*A* shows a screenshot of the workflow editor used to compose the original HH squid giant axon model (181). HH models of sodium, potassium, and leak currents were created. The workflow visual editor was used to interconnect these models to create a HH model of the neuronal action potential (Figure 5.3*A*). Galaxy simulated the model and produced a plot of the membrane potential oscillations over time (Figure 5.3*B*). Links to the workflow and history that produced this figure are given in its caption.

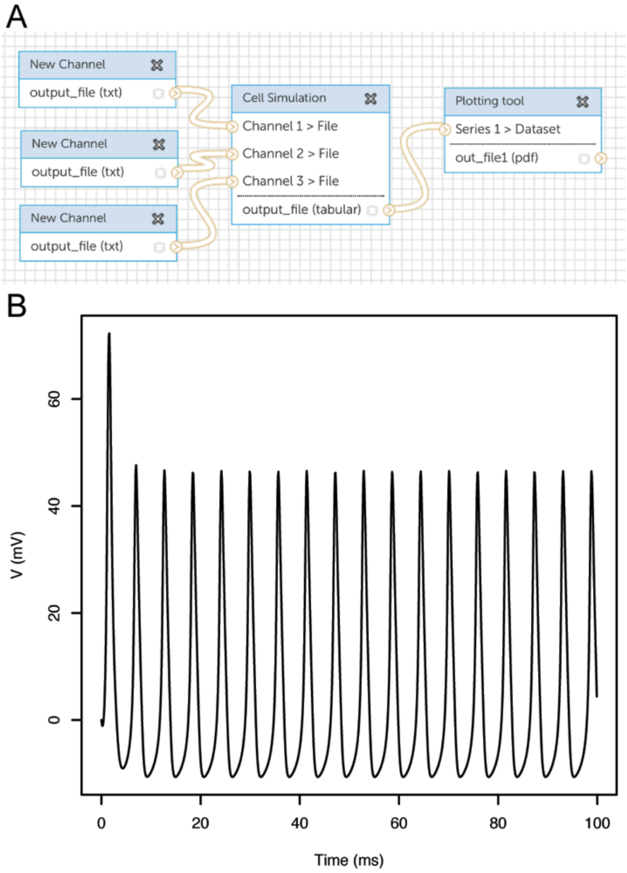

Figure 5.3 Model composition of the Hodgkin-Huxley squid giant axon model using Galaxy workflows.

(A) Workflow interface shows nodes for sodium, potassium, and leak currents (*left*), which are then combined into a cell model for simulation of current injection (*middle*). The final node (*right*) plots the membrane potential, as shown in panel (B). Simulation history and workflow available at: http://cvrg.galaxycloud.org/u/mwalker/w/hh-sga and http://cvrg.galaxycloud.org/u/mwalker/h/hh-sga.

5.3 Discussion

We have introduced the concept of MaSS to address the many challenges associated with computational research and demonstrated that Galaxy is a powerful, easy to use platform for realizing this approach. Galaxy enables users to run and publish simulations and workflows, thus providing complete provenance and transparency of results. We showed how a complex model of Ca^{2+} sparks that requires high performance computing resources for execution can be seamlessly customized and run in the cloud. We have shown how the RRS capabilities of Galaxy can be leveraged when working with SBML- and CellML-encoded models. External repositories such as the BioModels database and the CellML Repository can be integrated into Galaxy using web services, enabling users to query and retrieve models directly. Finally, Galaxy supports model composition in an intuitive graphical workflow editor. This is a powerful feature that will enable modelers to build, for example, cell models from constitutive signaling networks and ion channel modules. To our knowledge, there are no other biomodel databases with the web-based workflow capabilities of Galaxy. While CVRG Galaxy and these tools are currently fully usable, we stress that their development is ongoing. We present them as preliminary examples of how the features of Galaxy can be harnessed for delivering complex models via MaSS.

We are currently hosting an instance of MaSS for community use (https://cvrg.galaxycloud.org) as a biomodeling reproducible research resource. Users wishing to contribute and share models should contact the authors for assistance. This service will host a catalog of user-submitted models that complies with existing annotation standards such as MIRIAM (182). Integration with the BioPortal ontology

(174) has been developed and will be used in the annotation of each model. Galaxy integration will allow users to search models by their ontology, run simulations, and browse their associated histories and workflows. Persistent availability of this data will be ensured using permanent URLs that can be embedded in publications. The repository will fulfill the pressing need for an accessible platform for retrieving, running, and sharing computational simulations.

5.4 Conclusion

We demonstrated the ways in which Galaxy can be used to share complex multi-scale biological models in a manner that supports reproducible modeling research. We proposed the concept of Models and Simulations as a Service (MaSS) in which these capabilities are delivered as easy to use, on-demand web services accessed through the user's browser. To demonstrate MaSS, we showed how Galaxy tools could be used to wrap the SRS model into a convenient web interface that allows users to seamlessly access, customize and execute simulations. We showed how the RRS capabilities of Galaxy enable documentation and reproducibility of published results. We also showed multiple ways in which Galaxy can be used to access and simulate models encoded using the SBML and CellML languages, an approach that automatically inherits the RRS capabilities of the Galaxy platform. Finally, we demonstrated how the WCS capabilities of Galaxy could be used to compose hierarchical models from sub-module components.

Chapter 6 Conclusion and Future Directions

Ca^{2+} plays a central role in the function of the cardiac myocyte. In heart disease, Ca^{2+} dynamics are severely altered, resulting in functional changes to cellular contraction (156, 183), ultrastructure (39, 80), Ca^{2+} handling protein expression (184), Ca^{2+}-dependent signaling pathways (24, 105, 185), and increased propensity for arrhythmias (99, 186). In this work, computational and mathematical models were used to investigate the mechanisms of altered Ca^{2+} handling under normal and pathological conditions.

The SRS model combined a contemporary model of RyR gating with realistic anatomical and biophysical detail based on recent data. The model was used to test the functional roles of $[Ca^{2+}]_{jsr}$-dependent RyR regulation, release site ultrastructure, and RyR channel positioning. These results provide a novel perspective on nanoscale Ca^{2+} spark dynamics and a framework for investigating the roles of additional biophysical components including localized NCX (145), localized Na^+/K^+ ATPase (37), mitochondria (187, 188), and RyR superclusters (140) in health and disease.

An emergent property of the SRS model was the relationship between Ca^{2+} spark probability and the maximum eigenvalue of the adjacency matrix describing the RyR cluster lattice. RyRs were coupled to open neighboring channels via local rises in subspace $[Ca^{2+}]$, and the probability of a spontaneous RyR opening triggering a Ca^{2+} spark was highly dependent on the interconnectedness of the lattice network.

This empirical result was further investigated by describing the Ca^{2+} spark initiation process as a CN model, from which the relationship could be derived analytically. Capturing the behavior of the full biophysical model using this minimal abstraction lends intuition and brings the key mechanisms of probabilistic Ca^{2+} spark initiation into focus. The CN paradigm can be applied to a variety of clustered transmembrane receptors that also exhibit cooperativity in other cell types (131, 132).

Spontaneous ectopic activity in the heart occurs when DADs are induced by pathological conditions that enhance cellular Ca^{2+} overload (46, 47, 159). The stochastic tissue model was developed to study DAD generation and synchronization. Substantial DAD variability in an ensemble of cells was attributed to stochastic molecular events driven by spontaneous RyR openings. In a 1D fiber, this variability was sufficient to cause spatially varying DAD amplitude and probabilistic triggered activity despite the effects of electrotonic coupling between cells. Changes reflecting pathological remodeling in HF, including I_{K1} and g_{gap} reduction, greatly enhanced DAD amplitude variability.

It is not known, though speculated, if arrhythmias can be triggered by rare stochastic events (47). A novel method was developed to efficiently estimate the probability of extreme DADs. By assuming independence and identical distribution across cells of the stochastic processes driving spontaneous Ca^{2+} release, events of probability $\sim 10^{-6}$ could be estimated from the output of a single simulation. Future efforts could incorporate other methods for estimating rare event probabilities, including importance resampling (189) and simulation splitting (190). Under pathological conditions (50% I_{K1} and 50% g_{gap}), rare DADs that had amplitude ~50% higher than average occurred once in every 10^6 beats. Such events were characterized by clusters of cells exhibiting high-amplitude, synchronized Ca^{2+} release flux. This strongly suggests that rare DADs exceeding the threshold for AP activation can occur in a fiber of myocytes. However, future work is needed to investigate this phenomenon in realistic 3D tissue geometry.

Appendix A Superresolution Calcium Spark Model

A.1 Model Parameters

Table A.1 Diffusion Coefficients

Parameter	Definition	Value
D_{Ca}	Ca^{2+} diffusion coefficient	0.250 $\mu m^2\ ms^{-1}$ (67)
D_{ATP}	ATP diffusion coefficient	0.140 $\mu m^2\ ms^{-1}$
D_{Cmdn}	Calmodulin diffusion coefficient	0.025 $\mu m^2\ ms^{-1}$
D_{Fluo4}	Fluo-4 diffusion coefficient	0.042 $\mu m^2\ ms^{-1}$

Table A.2 Initial Conditions

Parameter	Definition	Value
C_0^{Cyto}	Resting cytoplasmic Ca^{2+} concentration	0.10 μM
C_0^{SR}	Resting SR Ca^{2+} concentration	1.0 mM

Table A.3 Buffering Parameters

Parameter	Definition	Value*
B_{ATP}^{Tot}	Total ATP concentration	455 μM
B_{Cmdn}^{Tot}	Total calmodulin concentration	24 μM
B_{Trpn}^{Tot}	Total troponin concentration	70 μM
B_{Fluo4}^{Tot}	Total fluo-4 concentration	50 μM
B_{Csqn}^{Tot}	Total calsequestrin concentration (JSR)	30 mM
ρ_{SL}	Sarcolemmal binding site density	1.6×10^{-13} $\mu mol\ \mu m^{-2}$ (63)
k_{on}^{ATP}	ATP on rate	0.225 $\mu M^{-1}\ ms^{-1}$
k_{off}^{ATP}	ATP off rate	45 ms^{-1}
k_{on}^{Cmdn}	Calmodulin on rate	0.023 $\mu M^{-1}\ ms^{-1}$
k_{off}^{Cmdn}	Calmodulin off rate	0.238 ms^{-1}
k_{on}^{Trpn}	Troponin on rate	0.039 $\mu M^{-1}\ ms^{-1}$
k_{off}^{Trpn}	Troponin off rate	0.020 ms^{-1}
k_{on}^{Fluo4}	Fluo-4 on rate	0.100 $\mu M^{-1}\ ms^{-1}$

k_{off}^{Fluo4}	Fluo-4 off rate	0.110 ms^{-1}
k_{on}^{Csqn}	Calsequestrin on rate	0.100 µM^{-1} ms^{-1}
k_{off}^{Csqn}	Calsequestrin off rate	63.8 ms^{-1}
K_{D}^{SL}	Sarcolemmal binding site affinity	13 µM (63)

---

*Unless otherwise noted, diffusion coefficients and buffering parameters were from (58).

Table A.4 RyR Gating Parameters

Parameter	**Definition**	**Value**[†]
v_{ryr}	RyR Ca^{2+} release rate constant	3.0×10^{-8} ms^{-1}
η	Ca^{2+} Hill coefficient	2.1
k^{+}	RyR open rate constant	1.107×10^{-4} ms^{-1}µM$^{-\eta}$
k^{-}	RyR close rate	0.50 ms^{-1}
ϕ_k	[Ca^{2+}]$_{jsr}$-dependent regulation affinity	1.5 mM
ϕ_b	[Ca^{2+}]$_{jsr}$-dependent regulation intercept	0.8025

[†] RyR gating parameters were fit to achieve physiological spark and leak rates.

Table A.5 SERCA and JSR Transport Parameters

Parameter	**Definition**	**Value**[‡]
v_{refill}	JSR refill rate	0.095 ms^{-1}
A_p	SERCA concentration	150 µM
$K_{d,i}$	SERCA cytosolic [Ca^{2+}] affinity	0.91 mM
$K_{d,sr}$	SERCA SR [Ca^{2+}] affinity	2.24 mM

[‡] JSR refill rate was adjusted to achieve a realistic refill time constant (~130 ms) (61).

SERCA parameters were taken from Williams et al. (12).

A.2 Equations

A.2.1 Transport Equations

The mesh was discretized into tetrahedral elements. For each element *i*, the time rate of change for $[Ca^{2+}]_i$ s given by,

$$\beta_i \frac{d[Ca^{2+}]_i}{dt} = \sum_{k=1}^{4} J_{i,k} + \sum_{j=1}^{N_B} (k_{off}^{k}[CaB_j]_i - k_{on}^{k}[Ca^{2+}]_i[B_j]_i) + J_i^{RyR} + J_i^{refill} + J_i^{SERCA} + J_i^{LCC}, \quad \text{(A.1)}$$

where N_B refers to the number of buffering species B_j, and $J_{i,k}$ is the net flux into the element through each face *k*, which is a function of the element geometry and $[Ca^{2+}]$ gradient. No-flux conditions were imposed at TT and JSR membranes, and at the domain boundary. Similarly, the transport equations for each Ca^{2+}-bound mobile buffer CaB_j is given by,

$$\frac{d[CaB_j]_i}{dt} = \sum_{k=1}^{4} J_{i,k} - k_{off}^{j}[CaB_j]_i + k_{on}^{j}[Ca^{2+}]_i[B_j]_i, \quad \text{(A.2)}$$

Note that because there are no external sources of buffers, total buffer concentration is conserved and therefore the unbound concentration is given by: $[B_j]_i = B_j^{Tot} - [CaB_j]_i$. Immobile buffers also used Eq. A2 with $J_{i,k} = 0$.

A.2.2 Dynamic Buffering Fraction

Recall that β_i refers to the dynamic buffering fraction due to sarcolemmal binding sites, which is given by,

$$\beta_i = \left(1 + \frac{\rho_{SL} A_i K_D^{SL}}{\left(K_D^{SL} + [Ca^{2+}]_i\right)^2}\right)^{-1}, \quad \text{(A.3)}$$

where ρ_{SL} is the sarcolemmal binding site density per area of TT membrane, K_D^{SL} is the sarcolemmal binding site affinity, and A_i is the surface area of TT membrane incident with the faces of element *i*.

A.2.3 RyR Flux

Each RyR *i* is mapped to the closest cytosolic and JSR elements with indices *j* and *k*, respectively. The flux of Ca^{2+} in each element with volumes V_j and V_k are then given by,

$$J_j^{RyR} = v_{RyR} \frac{25.84 \times 10^3 um^3}{V_j} \left([Ca^{2+}]_k - [Ca^{2+}]_j \right), \tag{A.4}$$

$$\text{and}\, J_k^{RyR} = -J_j^{RyR}. \tag{A.5}$$

A.2.4 SERCA Formulation

We implemented a thermodynamically constrained kinetic model of the SERCA pump presented in Tran et al. (60) and used parameters from Williams et al. (12). SERCA was homogeneously distributed in space > 200 nm from the TT axis. The flux in element *j* is given by,

$$J_j^{SERCA} = -(2 \times 10^{-3}) v_{cycle,j} A_p, \tag{A.6}$$

where A_p is the concentration of SERCA, and $v_{cycle,j}$ is the cycling rate given by,

$$v_{cycle,j} = \frac{3.24873 \times 10^{12} K_{i,j}^2 + K_{i,j}(9.17846 \times 10^6 - 11478.2 K_{sr}) - 0.329904 K_{sr}}{D_{cycle,j}}, \tag{A.7}$$

where

$$\begin{aligned} D_{cycle,j} = 0.104217 + 17.293 K_{sr} + K_{i,j}(1.75583 \times 10^6 + 7.61673 \times 10^6 K_{sr}) + \\ K_{i,j}^2 (6.08462 \times 10^{11} + 4.50544 \times 10^{11} K_{sr}) \end{aligned}, \tag{A.8}$$

$$K_{i,j} = \left(\frac{[Ca^{2+}]_j}{1 \times 10^3 K_{D,i}} \right)^2 \text{(A.9)}, \text{ and}\, K_{sr} = \left(\frac{[Ca^{2+}]_{NSR}}{1 \times 10^3 K_{d,sr}} \right)^2 . \tag{A.10}$$

A.3 Numerical Methods and Implementation

Briefly, it can be shown that for a Markov process with non-stationary transition rates, $v_i(t)$, if the last transition occurred at time t_0, then the time until the next reaction τ can be determined using the residual $R_i(\tau)$ given by,

$$R_i(\tau) = \int_{t_0}^{t_0+\tau} v_i(t)dt, \tag{A.11}$$

which is an exponential random variable with mean 1. Therefore, for each transition, one can draw a random number, x_i, from this distribution and effect the transition when $R_i(\tau) = x_i$.

The model was implemented in C++ and deployed to a cluster for ensemble simulations. A CUDA implementation was also developed for model prototyping and spark simulations on GPU devices. For a 100 ms simulation, the run times were 184 min on a 2.27GHz Intel Xeon E5520 and 18 min on an Nvidia Tesla C2075.

A.4 Ca^{2+} Spark Properties and ECC Gain

Ensemble simulations of individual CRUs were used to estimate whole-cell Ca^{2+} spark rate, leak rate, and ECC gain. Assuming that release sites are independent and the spark refractory period is much shorter than the mean waiting time for an channel opening in a 49 RyR cluster (23.2 sec at 100 nM $[Ca^{2+}]_{ss}$), whole-cell spark occurrence can be modeled as a thinned Poisson process compounded over all CRUs. This yields the spark rate $R_s \approx N_{RyR} r_{open} P_{spark}$ where N_{RyR} is the total number of RyRs per cell (1.25×10^6), r_{open} is the resting RyR opening rate, and P_{spark} is the spark fidelity, which is defined as the probability a Ca^{2+} spark is generated given that one RyR has opened. Spark fidelity was estimated by opening a randomly chosen RyR at the beginning of each simulation and counting the fraction of simulations where at least 4 RyRs were open.

The spark leak rate L_S was then estimated using the spark rate, R_S, and the average total Ca^{2+} release per spark J_S: $L_s \approx R_s J_s / V_{cyto}$, where V_{cyto} is the total cytosplasmic volume (18 pL). Non-spark leak L_N was calculated using the average amount of release per non-spark J_N: $L_N \approx N_{RyR} r_{open} (1-P_{spark}) J_N / V_{cyto}$. At least 1,000 independent simulations were performed to estimate P_{spark}, J_S, and J_N.

For RyR clusters inferred from STED images, sparks were simulated for each cluster by initially opening a randomly-chosen RyR. The spark fidelity of each RyR was then estimated as the ratio of the total number of sparks initiated by the RyR to the total number of times it was opened at the start of the simulation.

The distribution of the spark rate $R'_S(n)$ and leak rate $L'_S(n)$ in a population of RyR clusters was estimated as a function of cluster size n using the formulas: $R'_S(n) = f(n)R_S(n)$ and $L'_S(n) = f(n)L_S(n)$, where $R_S(n)$ and $L_S(n)$ are the spark and leak rate fit to both STED-informed and square array clusters, and $f(n)$ is the biexponential fit to the cluster size distribution.

ECC gain was defined as the ratio of peak release (RyR) to peak trigger (LCC) flux and was estimated by summing the release fluxes over > 1,000 simulations in response to a 200 ms voltage clamp from a holding potential of-80 mV.

Appendix B RyR Contact Network Model

B.1 CN Model Formulation

Contact process models have been widely studied for their use in modeling disease and computer virus spread (see Keeling and Eams (119) for a review). In the present work, the CN model represents the RyR channel gating of a cluster of *n* channels. We will restrict ourselves to clusters that are connected, i.e. there are no separate islands of channels. The model is composed of a set of *n* random variables $X_i(t) = 1$ if channel *i* is open at time *t* and 0 otherwise. If the channel is open, the probability that it closes within an infinitesimal time step *dt* is given by δdt, where $\delta = 0.5\ \mathrm{ms}^{-1}$ is constant. If channel *i* is closed, it transitions into the open state in time *dt* with probability $\beta Y_i(t)dt$, where $Y_i(t)$ is the number of open adjacent channels. β is a constant given by $\beta = k^+C^\eta$, where $k^+ = 1.107\times10^{-4}\ \mu\mathrm{M\ s}^{-\eta}$ is the opening rate constant, *C* is the local elevation of Ca^{2+} concentration caused by an open neighbor, and $\eta = 2.1$ is the Hill coefficient for Ca^{2+} binding. These parameters were taken from the SRS model.

The adjacency matrix **A** is defined as an n×n matrix, where element $(\mathbf{A})_{ij} = 1$ if channels *i* and *j* are adjacent, and 0 otherwise. The number of open adjacent channels is then given by $Y_i(t) = \sum_j (A)_{ij} X_j(t)$. Let $p_i(t) = P(X_i(t) = 1)$, the probability that channel *i* is open at time *t*, which obeys the equation (124)

$$\frac{dp_i(t)}{dt} = \beta\left(1 - X_i(t)\right)\sum_{j=1}^{n}(\mathbf{A})_{ij} X_j(t) - \delta X_i(t)\,. \tag{B.1}$$

The entire system can be more compactly represented as the matrix equation

$$\frac{d\underline{p}(t)}{dt} = \left(\beta \operatorname{diag}\left\{\underline{u} - \underline{X}(t)\right\}\mathbf{A} - \delta\mathbf{I}\right)\underline{X}(t)\,, \tag{B.2}$$

where $\underline{p}(t) = [p_1(t),..., p_n(t)]$, $\underline{u}$ is the all-one-vector, $\underline{X}(t) = [X_1(t),..., X_n(t)]$, and $\mathbf{I}$ is the identity matrix. The system is therefore described by a set of n coupled stochastic differential equations, whose solution is analytically intractable. We simulated the CN model using the Gillespie algorithm (115). Spark probability in the CN model was estimated by running an ensemble of 10,000 simulations per data point.

B.2 Ca^{2+} Diffusion Model

Here we incorporate a simple model of Ca^{2+} diffusion that relate the CN model to the Ca^{2+}-based communication between RyRs. We use the steady-state diffusion equation for a continuous point source in a semi-infinite volume to obtain the Ca^{2+} concentration sensed by a RyR neighboring a single open channel (191)

$$C = \frac{i_{RyR}}{2\pi z F d_C r}, \tag{B.3}$$

where $i_{RyR} = 0.15$ pA is the unitary current of a single channel, $z = 2$ is the valence of Ca^{2+}, F is Faraday's constant, d_C is the effective diffusion coefficient of Ca^{2+} in the release site subspace, and $r = 31$ nm is the distance between the open channel pore and neighboring Ca^{2+} binding site.

The diffusion coefficient for Ca^{2+} in the subspace is unknown, though estimates for d_C in the cytosol range from 100 to 600 $\mu m^2\ s^{-1}$ (67). Ca^{2+} buffering molecules, electrostatic interactions with the membrane, and tortuosity imposed by the large RyR channels can affect the motion Ca^{2+} ions (192). In light of these factors, the value of d_C was adjusted from 250 to 146 $\mu m^2\ s^{-1}$ to obtain the nominal value of $\beta = 0.115$ that yields accurate spark probabilities (see Figure 3.1).

B.3 Linear Mean-Field CN Model

A common approach is to derive a mean-field approximation of the first moment of $X_i(t)$ by assuming that the higher moments are equal to 0 (124). This yields a set of non-linear ordinary differential equations

$$\frac{d\underline{p}(t)}{dt} = \left(\beta \operatorname{diag}\left\{\underline{u} - \underline{p}(t)\right\}\mathbf{A} - \delta\mathbf{I}\right)\underline{p}(t), \tag{B.4}$$

where $\underline{p}(t)$ is now the vector of mean-field open probabilities. This non-linear system is difficult to analyze analytically (124). We further simplify the model by linearizing the equations about $\underline{p} = 0$ (91)

$$\frac{d\underline{p}(t)}{dt} = \left(\beta\mathbf{A} - \delta\mathbf{I}\right)\underline{p}(t). \tag{B.5}$$

We refer to this as the linearized mean-field CN (LCN) model, which is amenable to the tools of linear systems theory. Note that the system is stable if and only if the maximum (dominant) eigenvalue of $\beta\mathbf{A} - \delta\mathbf{I}$, given by $\beta\lambda_1 - \delta$, is less than 0, or

$$\lambda_1 < \frac{\delta}{\beta}, \tag{B.6}$$

where λ_1 is the maximum (dominant) eigenvalue of **A**. Therefore, if $\lambda_1 < \delta/\beta$, the open probabilities in the LCN decay to 0. Otherwise, $\underline{p}(t)$ is unbounded as t approaches infinity. While physically meaningless, this result implies that the open probabilities increase when most channels are closed, or $\underline{p}(t) \approx 0$ (near the origin of linearization).

The eigendecomposition of **A** is given by

$$\mathbf{A} = \mathbf{V}\mathbf{D}\mathbf{V}^{\mathrm{T}}, \tag{B.7}$$

where **V** is the modal matrix with columns formed by the orthonormal eigenvectors $\{\underline{v}_1, \ldots, \underline{v}_n\}$ of **A**, and **D** is a diagonal matrix of the eigenvalues $\{\lambda_1, \ldots, \lambda_n\}$ in descending order. Note that **A** is symmetric and therefore $\mathbf{V}^{-1} = \mathbf{V}^{\mathrm{T}}$. Combining Eqs. B16 and B18 gives

$$\frac{d\underline{p}(t)}{dt} = \mathbf{V}\left(\beta\mathbf{D} - \delta\mathbf{I}\right)\mathbf{V}^{\mathrm{T}}\underline{p}(t)\,, \tag{B.8}$$

which can be rewritten as the summation

$$\frac{d\underline{p}(t)}{dt} = \sum_{i=1}^{n}\left(\beta\lambda_i - \delta\right)\underline{v}_i\underline{v}_i^{\mathrm{T}}\,\underline{p}(t)\,. \tag{B.9}$$

The solution of this system is given by

$$\underline{p}(t) = \sum_{i=1}^{n} e^{(\beta\lambda_i - \delta)t}\,\underline{v}_i\underline{v}_i^{\mathrm{T}}\,\underline{p}(0)\,. \tag{B.10}$$

We refer to the eigenmodes as the eigenvalue-eigenvector pairs λ_i-$\underline{v}_i$. Note that $\underline{p}(t)$ is essentially a sum of the eigenmodes. If the initial probability distribution $\underline{p}(0) = \alpha\underline{v}_i$ for some constant α, then $\underline{p}$(t) is proportional to $\underline{v}_i$ for all t. In other words, the trajectory of the system will be entirely characterized by the i^{th} eigenmode. In general, the contribution of the i^{th} eigenmode is determined by the weight $\underline{v}_i^{\mathrm{T}}\underline{p}(0)$ and a time-dependent exponential factor with time constant $1/(\beta\lambda_i-\delta)$.

We define $\mathrm{E}[\underline{n}_O(t)]$ as the vector whose elements $(\mathrm{E}[\underline{n}_O(t)])_i$ give the expected number of open channels at time t given that channel i is open initially. This is computed by taking the sum of the elements of $\underline{p}$(t) in the previous equation

$$E\left[\underline{n}_O(t)\right] = \sum_{i=1}^{n} e^{(\beta\lambda_i - \delta)t}\left(\underline{u}^{\mathrm{T}}\,\underline{v}_i\right)\underline{v}_i\,. \tag{B.11}$$

We assume that in a resting RyR cluster, every channel experiences the same Ca^{2+} concentration and therefore is equally likely to initiate a spark. The expected total number of open channels when the first open channel is chosen randomly can be computed by setting $\underline{p}(0)$ to the uniform distribution and again summing over all elements of $\underline{p}(t)$

$$E\left[N_O(t)\right] = \frac{1}{n}\sum_{i=1}^{n} e^{(\beta\lambda_i-\delta)t}\left(\underline{u}^{\mathrm{T}}\,\underline{v}_i\right)^2 . \tag{B.12}$$

Appendix C Stochastic Tissue Model

C.1 Release Site Ca^{2+} Transport

$$\frac{d[Ca^{2+}]_{JSR,i,j,k}}{dt} = \beta_{JSR,i,j,k}\left(J_{NSR-JSR,i,j,k} - J_{RyR,i,j,k}\right) \tag{C.1}$$

$$\frac{d[Ca^{2+}]_{SS,i,j,k}}{dt} = \beta_{SS,i,j,k}\left(\frac{V_{JSR}}{V_{SS}} J_{RyR,i,j,k} + J_{LCC,i,j,k} - J_{SS-SM,i,j,k}\right) \tag{C.2}$$

$$\frac{d[Ca^{2+}]_{SM,i,j,k}}{dt} = \beta_{SM,i,j,k}\left(\frac{V_{SS}}{V_{SM}} J_{SS-SM,i,j,k} - J_{SL-Cyto,i,j,k} - \sum_{n_T} J_{Trans,i,j,k,n_T} - \sum_{n_L} J_{Long,i,j,k,n_L}\right) \tag{C.3}$$

$$\beta_{JSR,i,j,k} = \left(1 + \frac{B_{csqn}K_{csqn}}{\left(K_{csqn} + [Ca^{2+}]_{JSR,i,j,k}\right)^2}\right)^{-1} \tag{C.4}$$

$$\beta_{SS,i,j,k} = \left(1 + \frac{B_{SR}K_{SR}}{\left(K_{SR} + [Ca^{2+}]_{SS,i,j,k}\right)^2} + \frac{B_{SL,SS}K_{SL}}{\left(K_{SL} + [Ca^{2+}]_{SS,i,j,k}\right)^2}\right)^{-1} \tag{C.5}$$

$$\beta_{SM,i,j,k} = \left(1 + \frac{B_{cmdn}K_{cmdn}}{\left(K_{cmdn} + [Ca^{2+}]_{SM,i,j,k}\right)^2} + \frac{B_{SL,SM}K_{SL}}{\left(K_{SL} + [Ca^{2+}]_{SM,i,j,k}\right)^2}\right)^{-1} \tag{C.6}$$

$$J_{RyR,i,j,k} = N_{RyROpen,i,j,k}\, v_{RyR}\left([Ca^{2+}]_{JSR,i,j,k} - [Ca^{2+}]_{SS,i,j,k}\right) \tag{C.7}$$

$$J_{LCC,i,j,k} = N_{LCCOpen,i,j,k}\frac{C_m}{V_{SS}} P_{CaL}\frac{V_m F}{RT}\left(\frac{[Ca^{2+}]_{SS,i,j,k}\, e^{2V_mF/RT} - 0.31[Ca^{2+}]_o}{e^{2V_mF/RT} - 1}\right) \tag{C.8}$$

$$J_{NSR-JSR,i,j,k} = \left([Ca^{2+}]_{NSR} - [Ca^{2+}]_{JSR,i,j,k}\right)/\tau_{NSR-JSR} \tag{C.9}$$

$$J_{SS-SM,i,j,k} = \left([Ca^{2+}]_{SS,i,j,k} - [Ca^{2+}]_{SM,i,j,k}\right)/\tau_{SS-SM} \tag{C.10}$$

$$J_{SM-Cyto,i,j,k} = \left([Ca^{2+}]_{SM,i,j,k} - [Ca^{2+}]_{i}\right)/\tau_{SM-Cyto} \tag{C.11}$$

$$J_{Trans,i,j,k,n} = \left([Ca^{2+}]_{SM,i,j,k} - [Ca^{2+}]_{SM,i_n,j_n,k_n}\right) / \tau_{Trans} \tag{C.12}$$

$$J_{Long,i,j,k,n} = \left([Ca^{2+}]_{SM,i,j,k} - [Ca^{2+}]_{SM,i_n,j_n,k_n}\right) / \tau_{Long} \tag{C.13}$$

Table C.1 Release Site Ca^{2+} Transport Parameters

V_{JSR}	JSR volume	1.113×10^{-11} μL
V_{SS}	Subspace volume	0.812×10^{-12} μL
V_{SM}	Submembrane volume	5.85×10^{-11} μL
B_{csqn}	Calsequestrin buffer concentration	13.5 mM
K_{csqn}	Calsequestrin buffer affinity	0.63 mM
B_{SR}	SR membrane buffer site concentration	0.047 mM
K_{SR}	SR membrane buffer site affinity	0.00087 mM
$B_{SL,SS}$	Sarcolemmal membrane buffer site concentration (subspace)	1.124 mM
$B_{SL,SM}$	Sarcolemmal membrane buffer site concentration (submembrane)	0.122 mM
K_{SL}	Sarcolemmal membrane buffer site affinity	0.0087 mM
B_{cmdn}	Calmodulin buffer concentration	0.05 mM
K_{cmdn}	Calmodulin buffer affinity	2.38×10^{-3} mM
v_{RyR}	Open RyR Ca^{2+} transport rate	0.92 ms^{-1}
P_{CaL}	LCC permeability	9.13×10^{-13} cm μF s^{-1}
$\tau_{NSR\text{-}JSR}$	NSR-JSR Ca^{2+} diffusion time constant	9 ms
$\tau_{SS\text{-}SM}$	SS-SM Ca^{2+} diffusion time constant	0.02 ms
$\tau_{SM\text{-}Cyto}$	SM-Cyto Ca^{2+} diffusion time constant	1 ms
τ_{Long}	Longitudinal Ca^{2+} diffusion time constant	4 ms
τ_{Trans}	Transverse Ca^{2+} diffusion time constant	2 ms

C.2 LCC Markov Model

We used the LCC Markov model described by Greenstein and Winslow (59). In the baseline model, we assumed that 25% of LCCs were functionally active, which were randomly selected at the beginning of each simulation. The function γ that controls the rate into the Ca^{2+}-inactivated states was changed from a linear to a saturating function of $[Ca^{2+}]_{ss,i,j,k}$:

$$\gamma = 0.0022 \frac{[Ca^{2+}]_{SS,i,j,k}}{0.003 + [Ca^{2+}]_{SS,i,j,k}} . \tag{C.14}$$

C.3 Sensitivity Analysis of the Filtering Method

According to Eq. 4.6, the ratio σ_V/σ_J represents the sensitivity of V_{max} with respect to deviations from the average in the filtered release flux values, $J'_{max}-\mu_J$. Compared to the baseline, the sensitivity was 46% larger with 50% IK1 density and 17% larger with both 50% IK1 and 50% g_{gap} due to the reduced outward current. In the latter case, the sensitivity was 20% lower than with 50% IK1 alone. This result is counter-intuitive, as one would expect the sensitivity of V_{max} with respect to J_{RyR} to increase due to the reduced electrotonic load.

This discrepancy can be explained by the fact that the filter width was reduced by ~50% after introducing 50% g_{gap}. Note that combining Eqs. 4.4 and 4.6 yields the expression

$$V'(x,t)=\mu_V+\frac{\sigma_V}{\sigma_J}\frac{1}{W}\left(\sum_{k=-(W-1)/2}^{(W-1)/2}J_{RyR}(x+k,t)-\frac{1}{N}\sum_{x'=1}^{N}\sum_{k=-(W-1)/2}^{(W-1)/2}J_{RyR}(x'+k,t)\right), \tag{C.15}$$

where N is the number of cells in the fiber. Note the summations in second term in parentheses can be exchanged and simplified to yield

$$V'(x,t)=\mu_V+\frac{\sigma_V}{\sigma_J}\frac{1}{W}\left(\sum_{k=-(W-1)/2}^{(W-1)/2}J_{RyR}(x+k,t)-\frac{W}{N}\sum_{x'=1}^{N}J_{RyR}(x',t)\right). \tag{C.16}$$

The partial derivative of V' at cell x with respect to J'_{RyR} of any cell $x-(W-1)/2 \le x' \le x+(W-1)/2$, lying within the filter window centered on x, is therefore approximated by

$$\frac{\partial V'(x,t)}{\partial J_{RyR}(x',t)}=\frac{\sigma_V}{\sigma_J}\frac{1}{W}\left(1-\frac{W}{N}\right)\approx\frac{\sigma_V}{\sigma_J}\frac{1}{W}, \tag{C.17}$$

assuming that the filter width is much smaller than the fiber length (W/N << 1). Therefore V' is approximated by the linear function

$$V'(x,t) \approx V'_0(t) + \frac{\sigma_V}{\sigma_J}\frac{1}{W}\sum_{k=-(W-1)/2}^{(W-1)/2} J_{RyR}(x+k,t) \quad \text{(C.18)}$$
,

The variance of V' therefore given by

$$Var(V'(x,t)) = E\left[V'(x,t)^2\right] - E\left[V'(x,t)\right]^2 \quad \text{(C.19)}$$
.

Combining Eqs. C.18 and C.19 and applying the linearity property of expectation gives the result

$$Var(V'(x,t)) \approx \left(\frac{\sigma_V}{\sigma_J}\frac{1}{W}\right)^2 Var\left(\sum_{k=-(W-1)/2}^{(W-1)/2} J_{RyR}(x+k,t)\right) \quad \text{(C.20)}$$
.

Therefore the standard deviation of V' is given by the product of $(\sigma_V/\sigma_J)/W$ and the standard deviation of J_{RyR} over the filter window.

List of References

1. Chugh, S. S., K. Reinier, C. Teodorescu, A. Evanado, M. A. Samara, R. Mariani, K. Gunson, and J. Jui. 2008. Epidemiology of Sudden Cardiac Death: Clinical and Research Implications. Progress in Cardiovascular Diseases 51:213-228.
2. Heidenreich, P. a., J. G. Trogdon, O. a. Khavjou, J. Butler, K. Dracup, M. D. Ezekowitz, E. A. Finkelstein, Y. Hong, S. C. Johnston, A. Khera, D. M. Lloyd-Jones, S. a. Nelson, G. Nichol, D. Orenstein, P. W. F. Wilson, and Y. J. Woo. 2011. Forecasting the future of cardiovascular disease in the United States: a policy statement from the American Heart Association. Circulation 123:933-944.
3. Tomaselli, G. F., and D. P. Zipes. 2004. What causes sudden death in heart failure? Circ Res 95:754-763.
4. Zipes, D. P., and H. J. Wellens. 1998. Sudden cardiac death. Circulation 98:2334-2351.
5. Mohler, P. J., J.-J. Schott, A. O. Gramolini, K. W. Dilly, S. Guatimosim, W. H. duBell, L.-S. Song, K. Haurogné, F. Kyndt, M. E. Ali, T. B. Rogers, W. J. Lederer, D. Escande, H. Le Marec, and V. Bennett. 2003. Ankyrin-B mutation causes type 4 long-QT cardiac arrhythmia and sudden cardiac death. Nature 421:634-639.
6. Leenhardt, A., I. Denjoy, and P. Guicheney. 2012. Catecholaminergic polymorphic ventricular tachycardia. Circulation Arrhythmia and Electrophysiology 5:1044-1052.

7. Cannell, M. B., H. Cheng, and W. J. Lederer. 1994. Spatial non-uniformities in [Ca2+]i during excitation-contraction coupling in cardiac myocytes. Biophys J 67:1942-1956.

8. Cheng, H., W. J. Lederer, and M. B. Cannell. 1993. Calcium sparks: elementary events underlying excitation-contraction coupling in heart muscle. Science 262:740-744.

9. Zima, A. V., E. Bovo, D. M. Bers, and L. A. Blatter. 2010. Ca(2)+ spark-dependent and -independent sarcoplasmic reticulum Ca(2)+ leak in normal and failing rabbit ventricular myocytes. J Physiol 588:4743-4757.

10. Santiago, D. J., J. W. Curran, D. M. Bers, W. J. Lederer, M. D. Stern, E. Ríos, and T. R. Shannon. 2010. Ca sparks do not explain all ryanodine receptor-mediated SR Ca leak in mouse ventricular myocytes. Biophys J 98:2111-2120.

11. Sato, D., and D. M. Bers. 2011. How does stochastic ryanodine receptor-mediated Ca leak fail to initiate a Ca spark? Biophys J 101:2370-2379.

12. Williams, G. S. B., A. C. Chikando, H.-T. M. Tuan, E. A. Sobie, W. J. Lederer, and M. S. Jafri. 2011. Dynamics of calcium sparks and calcium leak in the heart. Biophys J 101:1287-1296.

13. Brochet, D. X. P., W. Xie, D. Yang, H. Cheng, and W. J. Lederer. 2011. Quarky calcium release in the heart. Circul Res 108:210-218.

14. Sobie, E. A., S. Guatimosim, L. Gómez-Viquez, L.-S. Song, H. Hartmann, M. Saleet Jafri, and W. J. Lederer. 2006. The Ca2+ leak paradox and "rogue ryanodine receptors": SR Ca2+ efflux theory and practice. Progress in Biophysics and Molecular Biology 90:172-185.

15. Qin, J., G. Valle, A. Nani, H. Chen, J. Ramos-Franco, A. Nori, P. Volpe, and M. Fill. 2009. Ryanodine receptor luminal Ca2+ regulation: swapping calsequestrin and channel isoforms. Biophys J 97:1961-1970.

16. Cannell, M. B., C. H. T. Kong, M. S. S. Imtiaz, and D. R. Laver. 2013. Control of sarcoplasmic reticulum Ca2+ release by stochastic RyR gating within a 3D model of the cardiac dyad and importance of induction decay for CICR termination. Biophys J 104:2149-2159.

17. Chen, H., G. Valle, S. Furlan, A. Nani, S. Gyorke, M. Fill, and P. Volpe. 2013. Mechanism of calsequestrin regulation of single cardiac ryanodine receptor in normal and pathological conditions. J Gen Physiol 142:127-136.

18. Li, J., M. S. Imtiaz, N. a. Beard, A. F. Dulhunty, R. Thorne, D. F. Vanhelden, and D. R. Laver. 2013. ß-Adrenergic Stimulation Increases RyR2 Activity via Intracellular Ca(2+) and Mg(2+) Regulation. PLoS One 8:e58334-e58334.

19. Györke, I., and S. Györke. 1998. Regulation of the cardiac ryanodine receptor channel by luminal Ca2+ involves luminal Ca2+ sensing sites. Biophys J 75:2801-2810.

20. Laver, D. R., and B. N. Honen. 2008. Luminal Mg2+, a key factor controlling RYR2-mediated Ca2+ release: cytoplasmic and luminal regulation modeled in a tetrameric channel. The Journal of General Physiology 132:429-446.

21. Qin, J., G. Valle, A. Nani, A. Nori, N. Rizzi, S. G. Priori, P. Volpe, and M. Fill. 2008. Luminal Ca2+ regulation of single cardiac ryanodine receptors: insights provided by calsequestrin and its mutants. The Journal of General Physiology 131:325-334.

22. Guo, T., D. Gillespie, and M. Fill. 2012. Ryanodine receptor current amplitude controls Ca2+ sparks in cardiac muscle. Circul Res 111:28-36.

23. Reiken, S., M. Gaburjakova, S. Guatimosim, A. M. Gomez, J. D'Armiento, D. Burkhoff, J. Wang, G. Vassort, W. J. Lederer, and A. R. Marks. 2003. Protein kinase A phosphorylation of the cardiac calcium release channel (ryanodine receptor) in normal and failing hearts. Role of phosphatases and response to isoproterenol. J Biol Chem 278:444-453.

24. Marx, S. O., S. Reiken, Y. Hisamatsu, T. Jayaraman, D. Burkhoff, N. Rosemblit, and a. R. Marks. 2000. PKA phosphorylation dissociates FKBP12.6 from the calcium release channel (ryanodine receptor): defective regulation in failing hearts. Cell 101:365-376.

25. Hashambhoy, Y. L., J. L. Greenstein, and R. L. Winslow. 2010. Role of CaMKII in RyR leak, EC coupling and action potential duration: a computational model. J Mol Cell Cardiol 49:617-624.

26. Guo, T., T. Zhang, R. Mestril, and D. M. Bers. 2006. Ca2+/Calmodulin-dependent protein kinase II phosphorylation of ryanodine receptor does affect calcium sparks in mouse ventricular myocytes. Circul Res 99:398-406.

27. Marx, S. O., J. Gaburjakova, M. Gaburjakova, C. Henrikson, K. Ondrias, and A. R. Marks. 2001. Coupled Gating Between Cardiac Calcium Release Channels (Ryanodine Receptors). Circul Res 88:1151-1158.

28. Groff, J. R., and G. D. Smith. 2008. Ryanodine receptor allosteric coupling and the dynamics of calcium sparks. Biophys J 95:135-154.

29. Belevych, A. E., D. Terentyev, S. Viatchenko-Karpinski, R. Terentyeva, A. Sridhar, Y. Nishijima, L. D. Wilson, A. J. Cardounel, K. R. Laurita, C. a. Carnes, G. E. Billman, and S. Gyorke. 2009. Redox modification of ryanodine receptors underlies calcium alternans in a canine model of sudden cardiac death. Cardiovascular Research 84:387-395.

30. Györke, S. 2009. Molecular basis of catecholaminergic polymorphic ventricular tachycardia. Heart Rhythm 6:123-129.

31. Jiang, D., R. Wang, B. Xiao, H. Kong, D. J. Hunt, P. Choi, L. Zhang, and S. R. W. Chen. 2005. Enhanced store overload-induced Ca2+ release and channel sensitivity to luminal Ca2+ activation are common defects of RyR2 mutations linked to ventricular tachycardia and sudden death. Circul Res 97:1173-1181.

32. Gaur, N., and Y. Rudy. 2011. Multiscale modeling of calcium cycling in cardiac ventricular myocyte: macroscopic consequences of microscopic dyadic function. Biophys J 100:2904-2912.

33. Lee, Y.-S., O. Z. Liu, H. S. Hwang, B. C. Knollmann, and E. A. Sobie. 2013. Parameter sensitivity analysis of stochastic models provides insights into cardiac calcium sparks. Biophys J 104:1142-1150.

34. Franzini-Armstrong, C., F. Protasi, and V. Ramesh. 1999. Shape, size, and distribution of Ca(2+) release units and couplons in skeletal and cardiac muscles. Biophys J 77:1528-1539.

35. Baddeley, D., I. D. Jayasinghe, L. Lam, S. Rossberger, M. B. Cannell, and C. Soeller. 2009. Optical single-channel resolution imaging of the ryanodine receptor

distribution in rat cardiac myocytes. Proceedings of the National Academy of Sciences 106:22275-22280.

36. Hayashi, T., M. E. Martone, Z. Yu, A. Thor, M. Doi, M. J. Holst, M. H. Ellisman, and M. Hoshijima. 2009. Three-dimensional electron microscopy reveals new details of membrane systems for Ca2+ signaling in the heart. J Cell Sci 122:1005-1013.

37. Wong, J., D. Baddeley, E. A. Bushong, Z. Yu, M. H. Ellisman, M. Hoshijima, and C. Soeller. 2013. Nanoscale Distribution of Ryanodine Receptors and Caveolin-3 in Mouse Ventricular Myocytes: Dilation of T-Tubules near Junctions. Biophys J 104:L22-L24.

38. Zhang, H.-B., R.-C. Li, M. Xu, S.-M. Xu, Y.-S. Lai, H.-D. Wu, X.-J. Xie, W. Gao, H. Ye, Y.-Y. Zhang, X. Meng, and S.-Q. Wang. 2013. Ultrastructural uncoupling between T-tubules and sarcoplasmic reticulum in human heart failure. Cardiovascular Research 98:269-276.

39. Wu, H. D., M. Xu, R. C. Li, L. Guo, Y. S. Lai, S. M. Xu, S. F. Li, Q. L. Lu, L. L. Li, H. B. Zhang, Y. Y. Zhang, C. M. Zhang, and S. Q. Wang. 2012. Ultrastructural remodelling of Ca(2+) signalling apparatus in failing heart cells. Cardiovasc Res 95:430-438.

40. Wei, S., A. Guo, B. Chen, W. Kutschke, Y.-P. Xie, K. Zimmerman, R. M. Weiss, M. E. Anderson, H. Cheng, and L.-S. Song. 2010. T-tubule remodeling during transition from hypertrophy to heart failure. Circul Res 107:520-531.

41. Wagner, E., M. A. Lauterbach, T. Kohl, V. Westphal, G. S. B. Williams, J. H. Steinbrecher, J.-H. Streich, B. Korff, H.-T. M. Tuan, B. Hagen, S. Luther, G.

Hasenfuss, U. Parlitz, M. S. Jafri, S. W. Hell, W. J. Lederer, and S. E. Lehnart. 2012. Stimulated emission depletion live-cell super-resolution imaging shows proliferative remodeling of T-tubule membrane structures after myocardial infarction. Circul Res 111:402-414.

42. Cheng, H., M. R. Lederer, W. J. Lederer, and M. B. Cannell. 1996. Calcium sparks and [Ca2+]i waves in cardiac myocytes. Am J Physiol 270:C148-159.

43. Berlin, J. R., M. B. Cannell, and W. J. Lederer. 1989. Cellular origins of the transient inward current in cardiac myocytes. Role of fluctuations and waves of elevated intracellular calcium. Circul Res 65:115-126.

44. Moss, A. J., H. T. Davis, J. DeCamilla, and L. W. Bayer. 1979. Ventricular ectopic beats and their relation to sudden and nonsudden cardiac death after myocardial infarction. Circulation 60:998-1003.

45. Laurita, K. R., and R. P. Katra. 2005. Delayed afterdepolarization-mediated triggered activity associated with slow calcium sequestration near the endocardium. Journal of Cardiovascular Electrophysiology 16:418-424.

46. Fujiwara, K., H. Tanaka, H. Mani, T. Nakagami, and T. Takamatsu. 2008. Burst emergence of intracellular ca2+ waves evokes arrhythmogenic oscillatory depolarization via the Na+-Ca2+ exchanger: Simultaneous confocal recording of membrane potential and intracellular Ca2+ in the heart. Circul Res 103:509-518.

47. Wasserstrom, J. A., Y. Shiferaw, W. Chen, S. Ramakrishna, H. Patel, J. E. Kelly, M. J. O'Toole, A. Pappas, N. Chirayil, N. Bassi, L. Akintilo, M. Wu, R. Arora, and G. L. Aistrup. 2010. Variability in timing of spontaneous calcium release in

the intact rat heart is determined by the time course of sarcoplasmic reticulum calcium load. Circul Res 107:1117-1126.

48. Satoh, H., L. A. Blatter, and D. M. Bers. 1997. Effects of [Ca2+]i , SR Ca2+ load, and rest on Ca2+ spark frequency in ventricular myocytes. American Journal of Physiology Heart and Circulation Physiology 272:H657-H668.

49. Hucka, M., M. Hucka, F. Bergmann, S. Hoops, S. Keating, S. Sahle, and D. Wilkinson. 2010. The Systems Biology Markup Language (SBML): Language Specification for Level 3 Version 1 Core (Release 1 Candidate). Nature Precedings.

50. Hedley, W. J., M. R. Nelson, D. P. Bullivant, and P. F. Nielsen. 2001. A short introduction to CellML. Philosophical Transactions of the Royal Society of London Series a-Mathematical Physical and Engineering Sciences 359:1073-1089.

51. Li, C., M. Donizelli, N. Rodriguez, H. Dharuri, L. Endler, V. Chelliah, L. Li, E. He, A. Henry, M. I. Stefan, J. L. Snoep, M. Hucka, N. Le Novere, and C. Laibe. 2010. BioModels Database: An enhanced, curated and annotated resource for published quantitative kinetic models. BMC Syst Biol 4:92.

52. Miller, A. K., J. Marsh, A. Reeve, A. Garny, R. Britten, M. Halstead, J. Cooper, D. P. Nickerson, and P. F. Nielsen. 2010. An overview of the CellML API and its implementation. BMC Bioinformatics 11:178.

53. Hoops, S., S. Sahle, R. Gauges, C. Lee, J. Pahle, N. Simus, M. Singhal, L. Xu, P. Mendes, and U. Kummer. 2006. COPASI--a COmplex PAthway SImulator. Bioinformatics 22:3067-3074.

54. Garny, A., and P. J. Hunter. 2015. OpenCOR: a modular and interoperable approach to computational biology. Front Physiol 6:26.

55. Goecks, J., A. Nekrutenko, J. Taylor, and T. Galaxy. 2010. Galaxy: a comprehensive approach for supporting accessible, reproducible, and transparent computational research in the life sciences. Genome Biol 11:R86.

56. Blankenberg, D., G. Von Kuster, E. Bouvier, D. Baker, E. Afgan, N. Stoler, T. Galaxy, J. Taylor, and A. Nekrutenko. 2014. Dissemination of scientific software with Galaxy ToolShed. Genome Biol 15:403.

57. Brochet, D. X. P., D. Yang, A. Di Maio, W. J. Lederer, C. Franzini-Armstrong, and H. Cheng. 2005. Ca2+ blinks: rapid nanoscopic store calcium signaling. Proceedings of the National Academy of Sciences 102:3099-3104.

58. Hake, J., A. G. Edwards, Z. Yu, P. M. Kekenes-huskey, A. P. Michailova, J. A. McCammon, M. J. Holst, M. Hoshijima, and A. D. McCulloch. 2012. Modeling Calcium Sparks in a Three-Dimensional Reconstruction of a Calcium Release Unit. Journal of Physiology 590:4403-4422.

59. Greenstein, J. L., and R. L. Winslow. 2002. An integrative model of the cardiac ventricular myocyte incorporating local control of Ca2+ release. Biophys J 83:2918-2945.

60. Tran, K., N. P. Smith, D. S. Loiselle, and E. J. Crampin. 2009. A thermodynamic model of the cardiac sarcoplasmic/endoplasmic Ca(2+) (SERCA) pump. Biophys J 96:2029-2042.

61. Picht, E., A. V. Zima, T. R. Shannon, A. M. Duncan, L. A. Blatter, and D. M. Bers. 2011. Dynamic calcium movement inside cardiac sarcoplasmic reticulum during release. Circ Res 108:847-856.

62. Soeller, C., and M. B. Cannell. 1997. Numerical simulation of local calcium movements during L-type calcium channel gating in the cardiac diad. Biophys J 73:97-111.

63. Peskoff, A., J. A. Post, and G. A. Langer. 1992. Sarcolemmal calcium binding sites in heart: II. Mathematical model for diffusion of calcium released from the sarcoplasmic reticulum into the diadic region. J Membr Biol 129:59-69.

64. Tencerová, B., A. Zahradníková, J. Gaburjáková, and M. Gaburjáková. 2012. Luminal Ca2+ controls activation of the cardiac ryanodine receptor by ATP. The Journal of General Physiology 140:93-108.

65. Si, H., and K. Gärtner. Meshing piecewise linear complexes by constrained delaunay tetrahedralizations. 147-163.

66. Alfonsi, A., E. Canès, G. Turinici, B. D. Ventura, and W. Huisinga. 2004. Exact simulation of hybrid stochastic and deterministic models for biochemical systems. INRIA Rapport de Recherche, Thèmes NUM et BIO 5435:5435-5435.

67. Smith, G. D., J. E. Keizer, M. D. Stern, W. J. Lederer, and H. Cheng. 1998. A simple numerical model of calcium spark formation and detection in cardiac myocytes. Biophys J 75:15-32.

68. Picht, E., A. V. Zima, L. A. Blatter, and D. M. Bers. 2007. SparkMaster: automated calcium spark analysis with ImageJ. Am J Physiol Cell Physiol 293:C1073-1081.

69. Brouwer, A. E., and W. H. Haemers. 2009. Spectra of Graphs. Springer.

70. Sobie, E. A., K. W. Dilly, J. dos Santos Cruz, W. J. Lederer, and M. Saleet Jafri. 2002. Termination of Cardiac Ca2+ Sparks: An Investigative Mathematical Model of Calcium-Induced Calcium Release. Biophys J 83:59-78.

71. Tan, W., C. Fu, C. Fu, W. Xie, and H. Cheng. 2007. An anomalous subdiffusion model for calcium spark in cardiac myocytes. Appl Phys Lett 91:183901-183901.

72. Cheng, H., and W. J. Lederer. 2008. Calcium Sparks. Physiol Rev 88:1491-1545.

73. Wier, W. G., T. M. Egan, J. R. Lopez-Lopez, and C. W. Balke. 1994. Local control of excitation-contraction coupling in rat heart cells. J Physiol 474:463-471.

74. Jafri, M. S., J. J. Rice, and R. L. Winslow. 1998. Cardiac Ca2+ dynamics: the roles of ryanodine receptor adaptation and sarcoplasmic reticulum load. Biophys J 74:1149-1168.

75. Winslow, R. L., J. Rice, S. Jafri, E. Marbán, B. O. Rourke, C. T.-i. H. Failure, and E. Marba. 1999. Mechanisms of Altered Excitation-Contraction Coupling in Canine Tachycardia-Induced Heart Failure, II : Model Studies. Circul Res 84:571-586.

76. Gillespie, D., and M. Fill. 2013. Pernicious attrition and inter-RyR2 CICR current control in cardiac muscle. J Mol Cell Cardiol 58:53-58.

77. Shannon, T. R., K. S. Ginsburg, and D. M. Bers. 2002. Quantitative assessment of the SR Ca2+ leak-load relationship. Circul Res 91:594-600.

78. Trafford, A. W., M. E. Díaz, G. C. Sibbring, and D. A. Eisner. 2000. Modulation of CICR has no maintained effect on systolic Ca2+: simultaneous measurements

of sarcoplasmic reticulum and sarcolemmal Ca2+ fluxes in rat ventricular myocytes. The Journal of Physiology 522.2:259-270.

79. van Oort, R. J., A. Garbino, W. Wang, S. S. Dixit, A. P. Landstrom, N. Gaur, A. C. De Almeida, D. G. Skapura, Y. Rudy, A. R. Burns, M. J. Ackerman, and X. H. T. Wehrens. 2011. Disrupted junctional membrane complexes and hyperactive ryanodine receptors after acute junctophilin knockdown in mice. Circulation 123:979-988.

80. Liu, N., M. Denegri, W. Dun, S. Boncompagni, F. Lodola, F. Protasi, C. Napolitano, P. A. Boyden, and S. G. Priori. 2013. Abnormal propagation of calcium waves and ultrastructural remodeling in recessive catecholaminergic polymorphic ventricular tachycardia. Circ Res 113:142-152.

81. Denegri, M., R. Bongianino, F. Lodola, S. Boncompagni, V. C. De Giusti, J. E. Avelino-Cruz, N. Liu, S. Persampieri, A. Curcio, F. Esposito, L. Pietrangelo, I. Marty, L. Villani, A. Moyaho, P. Baiardi, A. Auricchio, F. Protasi, C. Napolitano, and S. G. Priori. 2014. Single Delivery of an Adeno-Associated Viral Construct to Transfer the CASQ2 Gene to Knock-In Mice Affected by Catecholaminergic Polymorphic Ventricular Tachycardia Is Able to Cure the Disease From Birth to Advanced Age. Circulation 129:2673-2681.

82. Kohl, T., U. Parlitz, S. W. Hell, S. Luther, and S. E. Lehnart. 2013. Analysis of Fluorescence Microscopy Super-Resolution Data of Protein Assemblies. Biophys J 104:444a-444a.

83. Yin, C. C., and F. A. Lai. 2000. Intrinsic lattice formation by the ryanodine receptor calcium-release channel. Nat Cell Biol 2:669-671.

84. Jiang, D., B. Xiao, D. Yang, R. Wang, P. Choi, L. Zhang, H. Cheng, and S. R. W. Chen. 2004. RyR2 mutations linked to ventricular tachycardia and sudden death reduce the threshold for store-overload-induced Ca2+ release (SOICR). Proceedings of the National Academy of Sciences 101:13062-13067.

85. Faloutsos, M., P. Faloutsos, and C. Faloutsos. 1999. On power-law relationships of the Internet topology. 251-262.

86. Cozzo, E., R. A. Baños, S. Meloni, and Y. Moreno. 2013. Contact-based social contagion in multiplex networks. Physical Review E - Statistical, Nonlinear, and Soft Matter Physics 88:1-5.

87. Kannan, N., and S. Vishveshwara. 1999. Identification of side-chain clusters in protein structures by a graph spectral method. J Mol Biol 292:441-464.

88. Banerjee, A., and J. Jost. 2007. Spectral plots and the representation and interpretation of biological data. Theory in Biosciences 126:15-21.

89. Zhang, S.-B., S.-Y. Zhou, J.-G. He, and J.-H. Lai. 2011. Phylogeny inference based on spectral graph clustering. J Comput Biol 18:627-637.

90. Ahmadlou, M., H. Adeli, and A. Adeli. 2010. New diagnostic EEG markers of the Alzheimer's disease using visibility graph. J Neural Transm 117:1099-1109.

91. Youssef, M., and C. Scoglio. 2011. An individual-based approach to SIR epidemics in contact networks. J Theor Biol 283:136-144.

92. Stern, M. D., L. S. Song, H. Cheng, J. S. Sham, H. T. Yang, K. R. Boheler, and E. Ríos. 1999. Local control models of cardiac excitation-contraction coupling. A possible role for allosteric interactions between ryanodine receptors. The Journal of General Physiology 113:469-489.

93. Zima, A. V., E. Picht, D. M. Bers, and L. A. Blatter. 2008. Partial inhibition of sarcoplasmic reticulum ca release evokes long-lasting ca release events in ventricular myocytes: role of luminal ca in termination of ca release. Biophys J 94:1867-1879.

94. Stern, M. D., E. Rios, and V. A. Maltsev. 2013. Life and death of a cardiac calcium spark. The Journal of General Physiology 142:257-274.

95. Terentyev, D., A. Nori, M. Santoro, S. Viatchenko-Karpinski, Z. Kubalova, I. Gyorke, R. Terentyeva, S. Vedamoorthyrao, N. a. Blom, G. Valle, C. Napolitano, S. C. Williams, P. Volpe, S. G. Priori, and S. Gyorke. 2006. Abnormal interactions of calsequestrin with the ryanodine receptor calcium release channel complex linked to exercise-induced sudden cardiac death. Circul Res 98:1151-1158.

96. Tao, T., S. C. O'Neill, M. E. Diaz, Y. T. Li, D. A. Eisner, and H. Zhang. 2008. Alternans of cardiac calcium cycling in a cluster of ryanodine receptors: a simulation study. American Journal of Physiology Heart and Circulation Physiology 295:H598-609.

97. Bovo, E., P. P. de Tombe, and A. V. Zima. 2014. The Role of Dyadic Organization in Regulation of Sarcoplasmic Reticulum Ca2+ Handling during Rest in Rabbit Ventricular Myocytes. Biophys J 106:1902-1909.

98. George, C. H., H. Jundi, N. L. Thomas, D. L. Fry, and F. A. Lai. 2007. Ryanodine receptors and ventricular arrhythmias: emerging trends in mutations, mechanisms and therapies. Journal of Molecular and Cellular Cardiology 42:34-50.

99. Knollmann, B. C., N. Chopra, T. Hlaing, B. Akin, T. Yang, K. Ettensohn, B. E. C. Knollmann, K. D. Horton, N. J. Weissman, I. Holinstat, W. Zhang, D. M. Roden, L. R. Jones, C. Franzini-armstrong, and K. Pfeifer. 2006. Casq2 deletion causes sarcoplasmic reticulum volume increase, premature Ca2+ release, and catecholaminergic polymorphic ventricular tachycardia. The Journal of Clinical Investigation 116:2510-2520.

100. Brunello, L., J. L. Slabaugh, B. R. Przemyslaw, H.-T. Ho, A. E. Belevych, Q. Lou, H. Chen, C. Napolitano, F. Lodola, S. G. Priori, V. V. Fedorov, P. Volpe, M. Fill, P. M. L. Janssen, and S. Gyorke. 2013. Decreased RyR2 refractoriness determines myocardial synchronization of aberrant Ca2+ release in a genetic model of arrhythmia. Proceedings of the National Academy of Sciences 110:10312-10317.

101. Lehnart, S. E., M. Mongillo, A. Bellinger, N. Lindegger, B.-X. Chen, W. Hsueh, S. Reiken, A. Wronska, L. J. Drew, C. W. Ward, W. J. Lederer, R. S. Kass, G. Morley, and A. R. Marks. 2008. Leaky Ca2+ release channel / ryanodine receptor 2 causes seizures and sudden cardiac death in mice. J Clin Invest 118:2230-2245.

102. Chen, W., R. Wang, B. Chen, X. Zhong, H. Kong, Y. Bai, Q. Zhou, C. Xie, J. Zhang, A. Guo, X. Tian, P. P. Jones, M. L. O'Mara, Y. Liu, T. Mi, L. Zhang, J. Bolstad, L. Semeniuk, H. Cheng, J. Zhang, J. Chen, D. P. Tieleman, A. M. Gillis, H. J. Duff, M. Fill, L.-S. Song, and S. R. W. Chen. 2014. The ryanodine receptor store-sensing gate controls Ca2+ waves and Ca2+-triggered arrhythmias. Nat Med 20:184-192.

103. Domeier, T. L., L. A. Blatter, and A. V. Zima. 2009. Alteration of sarcoplasmic reticulum Ca2+ release termination by ryanodine receptor sensitization and in heart failure. The Journal of Physiology 587:5197-5209.

104. Gomez, A. M., S. Guatimosim, K. W. Dilly, G. Vassort, and W. J. Lederer. 2001. Heart failure after myocardial infarction: altered excitation-contraction coupling. Circulation 104:688-693.

105. Ai, X., J. W. Curran, T. R. Shannon, D. M. Bers, and S. M. Pogwizd. 2005. Ca2+/calmodulin-dependent protein kinase modulates cardiac ryanodine receptor phosphorylation and sarcoplasmic reticulum Ca2+ leak in heart failure. Circ Res 97:1314-1322.

106. Terentyev, D., I. Györke, A. E. Belevych, R. Terentyeva, A. Sridhar, Y. Nishijima, E. C. de Blanco, S. Khanna, C. K. Sen, A. J. Cardounel, C. a. Carnes, and S. Györke. 2008. Redox modification of ryanodine receptors contributes to sarcoplasmic reticulum Ca2+ leak in chronic heart failure. Circul Res 103:1466-1472.

107. Song, L. S., E. A. Sobie, S. McCulle, W. J. Lederer, C. W. Balke, and H. Cheng. 2006. Orphaned ryanodine receptors in the failing heart. Proc Natl Acad Sci U S A 103:4305-4310.

108. Izu, L. T., W. G. Wier, and C. W. Balke. 2001. Evolution of cardiac calcium waves from stochastic calcium sparks. Biophys J 80:103-120.

109. Weiss, J. N., M. Nivala, A. Garfinkel, and Z. Qu. 2011. Alternans and arrhythmias: from cell to heart. Circul Res 108:98-112.

110. Lukyanenko, V., A. Chikando, and W. J. Lederer. 2009. Mitochondria in cardiomyocyte Ca2+ signaling. The International Journal of Biochemistry & Cell Biology 41:1957-1971.

111. Fischer, T. H., S. Neef, and L. S. Maier. 2013. The Ca-calmodulin dependent kinase II: a promising target for future antiarrhythmic therapies? Journal of Molecular and Cellular Cardiology 58:182-187.

112. Jayasinghe, I. D., M. B. Cannell, and C. Soeller. 2009. Organization of ryanodine receptors, transverse tubules, and sodium-calcium exchanger in rat myocytes. Biophys J 97:2664-2673.

113. Kekenes-Huskey, P. M., Y. Cheng, J. E. Hake, F. B. Sachse, J. H. Bridge, M. J. Holst, J. A. McCammon, A. D. McCulloch, and A. P. Michailova. 2012. Modeling effects of L-type Ca(2+) current and Na(+)-Ca(2+) exchanger on Ca(2+) trigger flux in rabbit myocytes with realistic t-tubule geometries. Frontiers in Physiology 3:351-351.

114. Walker, M. A., G. S. Williams, T. Kohl, S. E. Lehnart, M. S. Jafri, J. L. Greenstein, W. J. Lederer, and R. L. Winslow. 2014. Superresolution modeling of calcium release in the heart. Biophys J 107:3018-3029.

115. Gillespie, D. T. 1977. Exact Stochastic Simulation of couple chemical reactions. The Journal of Physical Chemistry 81:2340-2361.

116. Cvetković, D. M., M. Doob, and H. Sachs. 1980. Spectra of graphs : theory and application. Deutscher Verlag der Wissenschaften, Berlin.

117. Wehrens, X. H. T., S. E. Lehnart, S. R. Reiken, and A. R. Marks. 2004. Ca2+/calmodulin-dependent protein kinase II phosphorylation regulates the cardiac ryanodine receptor. Circul Res 94:e61-70.

118. Bovo, E., S. L. Lipsius, and A. V. Zima. 2012. Reactive oxygen species contribute to the development of arrhythmogenic Ca^{2+} waves during β-adrenergic receptor stimulation in rabbit cardiomyocytes. The Journal of Physiology 590:3291-3304.

119. Keeling, M. J., and K. T. D. Eames. 2005. Networks and epidemic models. Journal of the Royal Society, Interface 2:295-307.

120. Cator, E., and P. Van Mieghem. 2012. Second-order mean-field susceptible-infected-susceptible epidemic threshold. Physical Review E - Statistical, Nonlinear, and Soft Matter Physics 85:1-7.

121. Ruhnau, B. 2000. Eigenvector-centrality — a node-centrality? Social Networks 22:357-365.

122. Asghari, P., D. R. L. Scriven, S. Sanatani, S. K. Gandhi, A. I. M. Campbell, and E. D. W. Moore. 2014. Nonuniform and variable arrangements of ryanodine receptors within mammalian ventricular couplons. Circul Res 115:252-262.

123. Bers, D. M., and V. M. Stiffel. 1993. Ratio of ryanodine to dihydropyridine receptors in cardiac and skeletal muscle and implications for E-C coupling. Am J Physiol 264:C1587-1593.

124. Van Mieghem, P. 2011. The N-intertwined SIS epidemic network model. Computing (Vienna/New York) 93:147-169.

125. Van Mieghem, P., J. Omic, and R. Kooij. 2009. Virus spread in networks. IEEE/ACM Transactions on Networking 17:1-14.

126. Dickinson, G. D., D. Swaminathan, and I. Parker. 2012. The probability of triggering calcium puffs is linearly related to the number of inositol trisphosphate receptors in a cluster. Biophys J 102:1826-1836.

127. Diambra, L., and J. S. Marchant. 2011. Inositol (1,4,5)-trisphosphate receptor microarchitecture shapes Ca2+ puff kinetics. Biophys J 100:822-831.

128. Smith, I. F., D. Swaminathan, G. D. Dickinson, and I. Parker. 2014. Single-molecule tracking of inositol trisphosphate receptors reveals different motilities and distributions. Biophys J 107:834-845.

129. Endo, M. 2009. Calcium-induced calcium release in skeletal muscle. Physiol Rev 89:1153-1176.

130. Jayasinghe, I. D., M. Munro, D. Baddeley, B. S. Launikonis, and C. Soeller. 2014. Observation of the molecular organization of calcium release sites in fast- and slow-twitch skeletal muscle with nanoscale imaging. J R Soc Interface 11.

131. Huang, B., H. Babcock, and X. Zhuang. 2010. Breaking the diffraction barrier: super-resolution imaging of cells. Cell 143:1047-1058.

132. Truong-Quang, B. A., and P. F. Lenne. 2014. Membrane microdomains: from seeing to understanding. Frontiers in Plant Science 5:18.

133. Caré, B. R., and H. a. Soula. 2011. Impact of receptor clustering on ligand binding. BMC Systems Biology 5:48-48.

134. Sieber, J. J., K. I. Willig, C. Kutzner, C. Gerding-Reimers, B. Harke, G. Donnert, B. Rammner, C. Eggeling, S. W. Hell, H. Brubuller, and T. Lang. 2007. Anatomy

and Dynamics of a Supramolecular Membrane Protein Cluster. Science 317:1072-1076.

135. Kellner, R. R., C. J. Baier, K. I. Willig, S. W. Hell, and F. J. Barrantes. 2007. Nanoscale organization of nicotinic acetylcholine receptors revealed by stimulated emission depletion microscopy. Neuroscience 144:135-143.

136. Meyer, A. C., T. Frank, D. Khimich, G. Hoch, D. Riedel, N. M. Chapochnikov, Y. M. Yarin, B. Harke, S. W. Hell, A. Egner, and T. Moser. 2009. Tuning of synapse number, structure and function in the cochlea. Nat Neurosci 12:444-453.

137. Rossy, J., S. V. Pageon, D. M. Davis, and K. Gaus. 2013. Super-resolution microscopy of the immunological synapse. Curr Opin Immunol 25:307-312.

138. Jaqaman, K., and S. Grinstein. 2012. Regulation from within: the cytoskeleton in transmembrane signaling. Trends Cell Biol 22:515-526.

139. Greenfield, D., A. L. McEvoy, H. Shroff, G. E. Crooks, N. S. Wingreen, E. Betzig, and J. Liphardt. 2009. Self-organization of the Escherichia coli chemotaxis network imaged with super-resolution light microscopy. PLoS Biol 7:e1000137-e1000137.

140. Hou, Y., I. Jayasinghe, D. J. Crossman, D. Baddeley, and C. Soeller. 2015. Nanoscale analysis of ryanodine receptor clusters in dyadic couplings of rat cardiac myocytes. J Mol Cell Cardiol 80:45-55.

141. Soeller, C., and D. Baddeley. 2013. Super-resolution imaging of EC coupling protein distribution in the heart. Journal of Molecular and Cellular Cardiology 58:32-40.

142. Chen-Izu, Y., S. L. McCulle, C. W. Ward, C. Soeller, B. M. Allen, C. Rabang, M. B. Cannell, C. W. Balke, and L. T. Izu. 2006. Three-dimensional distribution of ryanodine receptor clusters in cardiac myocytes. Biophys J 91:1-13.

143. Subramanian, S., S. Viatchenko-Karpinski, V. Lukyanenko, S. Györke, and T. F. Wiesner. 2001. Underlying mechanisms of symmetric calcium wave propagation in rat ventricular myocytes. Biophys J 80:1-11.

144. Weber, C. R. 2001. Na+-Ca2+ Exchange Current and Submembrane [Ca2+] During the Cardiac Action Potential. Circul Res 90:182-189.

145. Scriven, D. R., P. Dan, and E. D. Moore. 2000. Distribution of proteins implicated in excitation-contraction coupling in rat ventricular myocytes. Biophys J 79:2682-2691.

146. Diaz, M. E., A. W. Trafford, S. C. O'Neill, and D. A. Eisner. 1997. Measurement of sarcoplasmic reticulum Ca2+ content and sarcolemmal Ca2+ fluxes in isolated rat ventricular myocytes during spontaneous Ca2+ release. J Physiol 501 (Pt 1):3-16.

147. Crank, J., P. Nicolson, and D. R. Hartree. 1947. A practical method for numerical evaluation of solutions of partial differential equations of the heat-conduction type. 50-50.

148. Belardinelli, L., and G. Isenberg. 1983. Actions of adenosine and isoproterenol on isolated mammalian ventricular myocytes. Circul Res 53:287-297.

149. Priori, S. G., and P. B. Corr. 1990. Mechanisms underlying early and delayed afterdepolarizations induced by catecholamines. Am J Physiol 258:H1796-1805.

150. Yue, D. T., S. Herzig, and E. Marban. 1990. Beta-Adrenergic Stimulation of Calcium Channels Occurs by Potentiation of High-Activity Gating Modes. Proc Natl Acad Sci USA 87:753-757.

151. Foteinou, P. T., J. L. Greenstein, and R. L. Winslow. 2015. Mechanistic Investigation of the Arrhythmogenic Role of Oxidized CaMKII in the Heart. Biophys J 109:838-849.

152. Greenstein, J. L., A. J. Tanskanen, and R. L. Winslow. 2004. Modeling the actions of beta-adrenergic signaling on excitation--contraction coupling processes. Ann N Y Acad Sci 1015:16-27.

153. Volders, P. G., M. Stengl, J. M. van Opstal, U. Gerlach, R. L. Spatjens, J. D. Beekman, K. R. Sipido, and M. A. Vos. 2003. Probing the contribution of IKs to canine ventricular repolarization: key role for beta-adrenergic receptor stimulation. Circulation 107:2753-2760.

154. Soltis, A. R., and J. J. Saucerman. 2010. Synergy between CaMKII substrates and β-adrenergic signaling in regulation of cardiac myocyte Ca(2+) handling. Biophys J 99:2038-2047.

155. Curran, J., M. J. Hinton, E. Ríos, D. M. Bers, and T. R. Shannon. 2007. Beta-adrenergic enhancement of sarcoplasmic reticulum calcium leak in cardiac myocytes is mediated by calcium/calmodulin-dependent protein kinase. Circul Res 100:391-398.

156. O'Rourke, B., D. A. Kass, G. F. Tomaselli, S. Kääb, R. Tunin, and E. Marbán. 1999. Mechanisms of Altered Excitation-Contraction Coupling Canine

Tachycardia-Induced Heart Failure, I: Experimental Studies. Circul Res 84:562-570.

157. Liu, T., D. A. Brown, and B. O'Rourke. 2010. Role of mitochondrial dysfunction in cardiac glycoside toxicity. J Mol Cell Cardiol 49:728-736.

158. Erickson, J. R., M. L. Joiner, X. Guan, W. Kutschke, J. Yang, C. V. Oddis, R. K. Bartlett, J. S. Lowe, S. E. O'Donnell, N. Aykin-Burns, M. C. Zimmerman, K. Zimmerman, A. J. Ham, R. M. Weiss, D. R. Spitz, M. A. Shea, R. J. Colbran, P. J. Mohler, and M. E. Anderson. 2008. A dynamic pathway for calcium-independent activation of CaMKII by methionine oxidation. Cell 133:462-474.

159. Katra, R. P., and K. R. Laurita. 2005. Cellular mechanism of calcium-mediated triggered activity in the heart. Circul Res 96:535-542.

160. Schlotthauer, K., and D. M. Bers. 2000. Sarcoplasmic Reticulum Ca2+ Release Causes Myocyte Depolarization: Underlying Mechanism and Threshold for Triggered Action Potentials. Circul Res:774-780.

161. Hoeker, G. S., R. P. Katra, L. D. Wilson, B. N. Plummer, and K. R. Laurita. 2009. Spontaneous calcium release in tissue from the failing canine heart. American Journal of Physiology Heart and Circulation Physiology 297:H1235-H1242.

162. Pogwizd, S. M., K. Schlotthauer, L. Li, W. Yuan, and D. M. Bers. 2001. Arrhythmogenesis and Contractile Dysfunction in Heart Failure. Circul Res 88:1159-1167.

163. Dhamoon, A. S., and J. Jalife. 2005. The inward rectifier current (IK1) controls cardiac excitability and is involved in arrhythmogenesis. Heart Rhythm 2:316-324.

164. Domenighetti, A. A., C. Boixel, D. Cefai, H. Abriel, and T. Pedrazzini. 2007. Chronic angiotensin II stimulation in the heart produces an acquired long QT syndrome associated with IK1 potassium current downregulation. J Mol Cell Cardiol 42:63-70.

165. Jongsma, H. J., and R. Wilders. 2000. Gap junctions in cardiovascular disease. Circ Res 86:1193-1197.

166. Venetucci, L. a., A. W. Trafford, and D. a. Eisner. 2007. Increasing ryanodine receptor open probability alone does not produce arrhythmogenic calcium waves: threshold sarcoplasmic reticulum calcium content is required. Circul Res 100:105-111.

167. Lukyanenko, V., S. Subramanian, I. Gyorke, T. F. Wiesner, and S. Gyorke. 1999. The role of luminal Ca2+ in the generation of Ca2+ waves in rat ventricular myocytes. The Journal of Physiology 518 (Pt 1:173-186.

168. Zaniboni, M., a. E. Pollard, L. Yang, and K. W. Spitzer. 2000. Beat-to-beat repolarization variability in ventricular myocytes and its suppression by electrical coupling. American Journal of Physiology Heart and Circulation Physiology 278:H677-H687.

169. Tanskanen, A. J., J. L. Greenstein, B. O'Rourke, and R. L. Winslow. 2005. The role of stochastic and modal gating of cardiac L-type Ca2+ channels on early after-depolarizations. Biophys J 88:85-95.

170. Xie, Y., D. Sato, A. Garfinkel, Z. Qu, and J. N. Weiss. 2010. So little source, so much sink: requirements for afterdepolarizations to propagate in tissue. Biophys J 99:1408-1415.

171. Winslow, R. L., J. Saltz, I. Foster, J. J. Carr, Y. Ge, M. I. Miller, L. Younes, D. Geman, S. Granite, T. Kurc, A. Post, R. Madduri, T. Ratnanather, J. Larkin, S. Ardekani, T. Brown, A. Kolasny, K. Reynolds, and M. Shipway. 2011. The CardioVascular Research Grid (CVRG) Project. In Proceedings of the AMIA Summit on Translational Bioinformatics. 77-81.

172. Madduri, R., K. Chard, R. Chard, L. Lacinski, A. Rodriguez, D. Sulakhe, D. Kelly, U. Dave, and I. Foster. 2015. The Globus Galaxies platform: delivering science gateways as a service. Concurrency and Computation-Practice & Experience 27:4344-4360.

173. Foster, I. 2011. Globus Online Accelerating and Democratizing Science through Cloud-Based Services. Ieee Internet Comput 15:70-73.

174. Noy, N. F., N. H. Shah, P. L. Whetzel, B. Dai, M. Dorf, N. Griffith, C. Jonquet, D. L. Rubin, M. A. Storey, C. G. Chute, and M. A. Musen. 2009. BioPortal: ontologies and integrated data resources at the click of a mouse. Nucleic Acids Res 37:W170-173.

175. Litzkow, M. J., M. Livny, and M. W. Mutka. Condor - A hunter of idle workstations. IEEE Comput. Soc. Press. 104-111.

176. Terentyev, D., Z. Kubalova, G. Valle, A. Nori, S. Vedamoorthyrao, R. Terentyeva, S. Viatchenko-Karpinski, D. M. Bers, S. C. Williams, P. Volpe, and S. Gyorke. 2008. Modulation of SR Ca release by luminal Ca and calsequestrin in cardiac myocytes: effects of CASQ2 mutations linked to sudden cardiac death. Biophys J 95:2037-2048.

177. Li, C., M. Courtot, N. Le Novere, and C. Laibe. 2010. BioModels.net Web Services, a free and integrated toolkit for computational modelling software. Brief Bioinform 11:270-277.

178. Saucerman, J. J., J. Zhang, J. C. Martin, L. X. Peng, A. E. Stenbit, R. Y. Tsien, and A. D. McCulloch. 2006. Systems analysis of PKA-mediated phosphorylation gradients in live cardiac myocytes. Proc Natl Acad Sci U S A 103:12923-12928.

179. ten Tusscher, K. H., D. Noble, P. J. Noble, and A. V. Panfilov. 2004. A model for human ventricular tissue. Am J Physiol Heart Circ Physiol 286:H1573-1589.

180. Lloyd, C. M., M. D. Halstead, and P. F. Nielsen. 2004. CellML: its future, present and past. Prog Biophys Mol Biol 85:433-450.

181. Hodgkin, A. L., and A. F. Huxley. 1952. A quantitative description of membrane current and its application to conduction and excitation in nerve. J Physiol 117:500-544.

182. Le Novere, N., A. Finney, M. Hucka, U. S. Bhalla, F. Campagne, J. Collado-Vides, E. J. Crampin, M. Halstead, E. Klipp, P. Mendes, P. Nielsen, H. Sauro, B. Shapiro, J. L. Snoep, H. D. Spence, and B. L. Wanner. 2005. Minimum information requested in the annotation of biochemical models (MIRIAM). Nat Biotechnol 23:1509-1515.

183. Hobai, I. a., and B. O'Rourke. 2001. Decreased Sarcoplasmic Reticulum Calcium Content Is Responsible for Defective Excitation-Contraction Coupling in Canine Heart Failure. Circulation 103:1577-1584.

184. Ahmmed, G. U., P. H. Dong, G. Song, N. A. Ball, Y. Xu, R. A. Walsh, and N. Chiamvimonvat. 2000. Changes in Ca2+ Cycling Proteins Underlie Cardiac

Action Potential Prolongation in a Pressure-Overloaded Guinea Pig Model With Cardiac Hypertrophy and Failure. Circul Res 86:558-570.

185. Kubalova, Z., D. Terentyev, S. Viatchenko-Karpinski, Y. Nishijima, I. Györke, R. Terentyeva, D. N. Q. da Cuñha, A. Sridhar, D. S. Feldman, R. L. Hamlin, C. a. Carnes, and S. Györke. 2005. Abnormal intrastore calcium signaling in chronic heart failure. Proceedings of the National Academy of Sciences 102:14104-14109.

186. Nuss, H. B., S. Kääb, D. a. Kass, G. F. Tomaselli, and E. Marbán. 1999. Cellular basis of ventricular arrhythmias and abnormal automaticity in heart failure. The American Journal of Physiology 277:H80-H91.

187. Winslow, R. L., M. A. Walker, and J. L. Greenstein. 2016. Modeling calcium regulation of contraction, energetics, signaling, and transcription in the cardiac myocyte. Wiley Interdiscip Rev Syst Biol Med 8:37-67.

188. Chikando, A. C., S. Kettlewell, G. S. Williams, G. Smith, and W. J. Lederer. 2011. Ca2+ dynamics in the mitochondria - state of the art. Journal of Molecular and Cellular Cardiology 51:627-631.

189. Zhang, B. W., D. Jasnow, and D. M. Zuckerman. 2010. The "weighted ensemble" path sampling method is statistically exact for a broad class of stochastic processes and binning procedures. The Journal of Chemical Physics 132:054107-054107.

190. Donovan, R. M., J. J. Tapia, D. P. Sullivan, J. R. Faeder, R. F. Murphy, M. Dittrich, and D. M. Zuckerman. 2016. Unbiased Rare Event Sampling in Spatial

Stochastic Systems Biology Models Using a Weighted Ensemble of Trajectories. PLoS Comput Biol 12:e1004611.

191. Bers, D. M., and A. Peskoff. 1991. Diffusion around a cardiac calcium channel and the role of surface bound calcium. Biophys J 59:703-721.

192. Tanskanen, A. J., J. L. Greenstein, A. Chen, S. X. Sun, and R. L. Winslow. 2007. Protein geometry and placement in the cardiac dyad influence macroscopic properties of calcium-induced calcium release. Biophys J 92:3379-3396.

Curriculum Vitae

Mark A. Walker

Educational History

Ph.D.	2016	Program in Biomedical Engineering Mentor: Raimond Winslow, PhD	Johns Hopkins University
BS	2010	Chemical Engineering	Tufts University

Other Professional Experience

Intern	2015	IBM TJ Watson Research Center
Instructor of Foundations of HPC in Computational Medicine (EN580.121.13)	2014	Johns Hopkins University
Teaching Assistant for Biological Models and Simulations (EN580.223)	2013	Johns Hopkins University
Res. Assistant	2008-2010	Tissue & Metabolic Eng. Lab, Tufts University

Academic Awards and Honors

2010	Summa cum laude	Tufts University
2010	Highest Thesis Honors	Tufts University
2010	Class of 1898 Prize	Tufts University
2009	Tau Beta Pi Engineering Honors Society	Tufts University
2008	Summer Scholar	Tufts University

Peer-Reviewed Publications

Walker, M. A., J. L. Greenstein, and R. L. Winslow. Functional coupling of RyR2 superclusters in the cardiac myocyte. In preparation.

Walker, M. A., V. Gurev, J. J. Rice, J. L. Greenstein, and R. L. Winslow. Investigation of rare arrhythmic events caused by delayed afterdepolarizations in a multiscale computational model of cardiac tissue. In preparation.

Winslow, R. L., **M. A. Walker**, and J. L. Greenstein. 2016. Modeling calcium regulation of contraction, energetics, signaling, and transcription in the cardiac myocyte. Wiley Interdiscip Rev Syst Biol Med 8:37-67.

Walker, M. A., R. Madduri, A. Rodriguez, J. L. Greenstein, and R. L. Winslow. 2016. Models and Simulations as a Service: Exploring the Use of Galaxy for Delivering Computational Models. Biophys J 110:1038-1043.

Walker, M. A., T. Kohl, S. E. Lehnart, J. L. Greenstein, W. J. Lederer, and R. L. Winslow. 2015. On the Adjacency Matrix of RyR2 Cluster Structures. PLoS Comput Biol 11:e1004521.

Ullah, E., **M. Walker**, K. Lee, and S. Hassoun. 2015. PreProPath: An Uncertainty-Aware Algorithm for Identifying Predictable Profitable Pathways in Biochemical Networks. IEEE/ACM Trans Comput Biol Bioinform 12:1405-1415.

Walker, M. A., G. S. Williams, T. Kohl, S. E. Lehnart, M. S. Jafri, J. L. Greenstein, W. J. Lederer, and R. L. Winslow. 2014. Superresolution modeling of calcium release in the heart. Biophys J 107:3018-3029.

Suhail, Y., Kshitiz, J. Lee, **M. Walker**, D. H. Kim, M. D. Brennan, J. S. Bader, and A. Levchenko. 2013. Modeling intercellular transfer of biomolecules through tunneling nanotubes. Bull Math Biol 75:1400-1416.

Presentations and Posters

Walker, M.A. and Winslow, R.L. Models and Simulations as a Service using Galaxy. Presentation and poster at the Interagency Modeling and Analysis Group (IMAG) Multiscale Modeling (MSM) Consortium meeting. September 8-9, 2015, Bethesda, MD.

Walker, M. A., T. Kohl, S. E. Lehnart, J. L. Greenstein, W. J. Lederer, and R. L. Winslow. Predicting Functional Cardiac Calcium Dynamics from RyR2 Cluster Structure. Presentation at the Society for Mathematical Biology Annual Meeting. July 1, 2015, Atlanta, GA.

Walker, M. A., T. Kohl, S. E. Lehnart, J. L. Greenstein, W. J. Lederer, and R. L. On the Adjacency Matrix of RyR2 Cluster Structures. Poster at the Annual Meeting of the Biophysical Society. February 7, 2015, Baltimore, MD.

Walker, M.A. and Winslow, R.L. Models as a Service. Presentation in the IMAG MSM Group Webinar Series. July 21, 2014.

Walker, M. A., G. S. Williams, T. Kohl, S. E. Lehnart, M. S. Jafri, J. L. Greenstein, W. J. Lederer, and R. L. Winslow. Super-Resolution Modeling of Calcium Release in Heart. Poster at the Annual Meeting of the Biophysical Society. February 17, 2014, San Francisco, CA.

Ullah, E., **M. Walker**, S. Hassoun, and K. Lee. "A Weighted Graph Algorithm for Identifying Dominant Metabolic Pathways." Presentation at the American Institute of Chemical Engineers Annual Meeting. November 10, 2009, Nashville, TN.

About the Author

Mark A. Walker was born July 21st, 1988 in Boston, Massachusetts. Mark grew up in Concord, Massachusetts, where he attended Concord Academy. In his senior year there, he developed a physics engine in Java and grew interested in modeling and simulation of physical systems. Mark then attended nearby Tufts University in Medford, Massachusetts, where he studied chemical and biological engineering as well as computer science. Under the supervision of Dr. Kyongbum Lee in the Department of Chemical and Biological Engineering and Dr. Soha Hassoun in the Department of Computer Science, Mark pursued interdisciplinary research projects in metabolic engineering. He graduated summa cum laude in 2010 and received Highest Thesis Honors for his research. Mark then enrolled in the Ph.D. program in the Department of Biomedical Engineering at the Johns Hopkins School of Medicine, where he honed his skills in systems biology modeling and high performance computing. Under the supervision of Dr. Raimond Winslow, he plunged into the field of cardiomyocyte electrophysiology and calcium signaling. During his graduate studies, Mark created and instructed an intensive programming course, Foundations of High Performance Computing in Computational Medicine. In 2015, he interned for three months at the IBM T.J. Watson Research Center in Yorktown Heights, New York under the supervision of Dr. J. Jeremy Rice in the Computational Biology and Functional Genomics Group. With the support of his mentor, labmates, friends, and family, Mark completed his dissertation on modeling of calcium-induced arrhythmias in 2016 and has accepted a research position as a computational biologist at the Broad Institute of Harvard University and MIT.